THE QUANTUM MECHANICS OF HYPERION

by

Nathan O. Wiebe
B.Sc., Simon Fraser University, 2002

THESIS SUBMITTED IN PARTIAL FULFILLMENT
OF THE REQUIREMENTS FOR THE DEGREE OF
MASTER OF SCIENCE
in the Department
of
Physics

SIMON FRASER UNIVERSITY
Spring, 2005

APPROVAL

Name:	Nathan O. Wiebe
Degree:	Master of Science
Title of thesis:	The Quantum Mechanics of Hyperion
Examining Committee:	Dr. Nancy Forde (Chair)

Dr. Leslie E. Ballentine, Supervisor
Professor, Department of Physics

Dr. Howard Trottier
Professor, Department of Physics

Dr. Igor Herbut
Associate Professor, Department of Physics

Dr. Steve Dodge, Internal Examiner
Assistant Professor, Department of Physics

Date Approved: April 20, 2005

SIMON FRASER UNIVERSITY

Partial Copyright Licence

The author, whose copyright is declared on the title page of this work, has granted to Simon Fraser University the right to lend this thesis, project or extended essay to users of the Simon Fraser University Library, and to make partial or single copies only for such users or in response to a request from the library of any other university, or other educational institution, on its own behalf or for one of its users.

The author has further granted permission to Simon Fraser University to keep or make a digital copy for circulation via the Library's website.

The author has further agreed that permission for multiple copying of this work for scholarly purposes may be granted by either the author or the Dean of Graduate Studies.

It is understood that copying or publication of this work for financial gain shall not be allowed without the author's written permission.

Permission for public performance, or limited permission for private scholarly use, of any multimedia materials forming part of this work, may have been granted by the author. This information may be found on the separately catalogued multimedia material.

The original Partial Copyright Licence attesting to these terms, and signed by this author, may be found in the original bound copy of this work, retained in the Simon Fraser University Archive.

Bennett Library
Simon Fraser University
Burnaby, BC, Canada

Abstract

In this thesis I examine the quantum mechanics of a satellite rotating about a fixed axis with gravitational gradient torques, and compare it to the classical expectation values and probability distributions.

The differences between quantum and classical expectation values scale as a power law in $\hbar$, so Hyperion's expectation values should be classical . The quantum probability distributions require either environmental interactions or coarse graining to appear classical. Both methods lead to quantum classical differences that are laws in $\hbar$, so the two effects are similar but not equivalent. Hence environmental interactions are not *required* to explain Hyperion's classical limit.

I also examine the Floquet states of the system and show that their average distribution is the classical distribution for late times, and extend this model into 3D in both quantum and classical mechanics. However, I find that the classical limit of 3D quantum rotations cannot be numerically investigated presently.

To my parents

Acknowledgments

I would like to thank Dr. Ballentine for all his help and guidance on this project. In addition I would like to thank Dr. J. Emerson for reviewing a portion of this thesis, and for his many helpful comments. I would also like to thank Dr. B.C. Sanders for his encouragement and comments on this work. Finally I'd like to thank the faculty and staff at S.F.U. for all their help over the years.

Contents

Appendices

List of Figures

Chapter 1

Introduction

Quantum mechanics is a more fundamental theory than classical mechanics, and so it should emerge in an asymptotic limit of the deeper theory. However argument persists about how the transition between the two theories occurs, and what criteria need to be met for it to do so.

This question is more important than ever because of the progress in the field of quantum computing, where the distinction between quantum and classical information can lead to an exponential speed up of certain algorithms. To understand the distinction between the two, we must come to grips with questions of what makes quantum mechanics different from classical mechanics, and how classical mechanics emerges out of it.

This question is particularly troublesome in chaotic systems because their greater sensitivity could conceivably amplify small quantum effects and cause them to grow to a macroscopic scale. This sensitivity can also cause different versions of the correspondence principle predict different experimental results [19, 18].

The correspondence principle states that every aspect of physical reality can be expressed in quantum mechanics if it is to be considered more fundamental than classical mechanics. The two versions of the correspondence principle that will be addressed here are the Liouville and the Ehrenfest correspondences. The Ehrenfest correspondence states that in the classical limit quantum mechanics will correspond to single particle Newtonian mechanics. The Liouville correspondence on the other hand, assumes that in the classical limit the quantum probability distribution corresponds to the classical probability distribution given by the Liouville equation.

For chaotic systems the Ehrenfest correspondence will innevitably breakdown, but the Liouville correspondence can still be valid after the Ehrenfest criteria breaks down [9]. The Liouville criteria is more robust than the Ehrenfest criteria, and is a better measure for determining when quantum mechanics corresponds to classical mechanics.

The distinction between the two is important in light of the claims by W.H. Zurek, that the classical limit of chaotic systems occurs because of environmental interactions [47, 46, 26]. As a particular example, he cites the chaotic rotation of Hyperion (one of the moons of Saturn) and claims that after 20 years Hyperion will be in a grossly non-classical superposition of states. He then states that environmental interactions are the only way to limit the growth of these quantum differences, and as a result the classical limit of Hyperion is a direct consequence of these interactions.

Although his argument fails to distinguish the Liouville and Ehrenfest breaktimes, there is reason to suspect that environmental effects could have an impact on the classical limit of chaotic systems. However we do not know the scale on which these presumably large quantum-classical differences would occur. So more work is needed in order to understand the classical limit of Hyperion, and to understand if environmental effects are needed to understand classicality.

There are other reasons to examine Hyperion's quantum rotation: the quantum mechanics of a satellite's chaotic rotation in a gravitational field has never been studied. Interesting quantum effects can emerge in classically chaotic systems, such as localization [21, 39] or fractal-like properties [5] which are unique to the model. Hyperion may exhibit these or other undiscovered quantum effects, so studying Hyperion's quantum mechanical rotation is interesting in and of itself.

In this thesis I will present a model of Hyperion's rotation, and compare the probability distributions and average angular momenta predicted by both quantum and classical mechanics. This analysis is repeated with environmental effects included, in order to determine what role, if any, they have in the classical limit. From previous work we know that the Ehrenfest correspondence has a very limited range of validity, so this work will not discuss the origin of single particle trajectories.

Before I present the model and my results, it is useful to review some material that will be used repeatedly in this thesis. I will review chaos in both classical and quantum mechanics, and discuss the Wigner representation of Quantum mechanics and the associated Husimi distribution. I will also discuss the correspondence principle, and give a brief discussion of decoherence and a short summary of Zurek's argument that Hyperion's classical appearance is due to decoherence.

1.1 Chaos in Classical and Quantum Mechanics

1.1.1 Chaos in Classical Mechanics

Chaos is a very interesting phenomenon that causes systems with chaos to be qualitatively different from those without it. Understanding these features is essential to understanding Zurek's claims about Hyperion, as well as to understand the quantum classical differences in Hyperion's chaotic tumbling. In this section I will discuss how chaos arises in classical dynamics, and how its signatures can be deduced from the distributions in quantum mechanics.

A classical system is chaotic if nearby trajectories separate exponentially with time, whereas nearby non-chaotic trajectories separate at most like a power law. To examine the origin of this separation, it is most convenient to look at chaos in systems with stroboscopic maps of the form

$$\mathbf{x}(n+1) = F(\mathbf{x}(n)) \tag{1.1}$$

To see how exponential separation can arise, I will examine what the map does to two nearby trajectories. Let the distance between these two trajectories $\mathbf{d}(n) = \mathbf{x}_1(n) - \mathbf{x}_2(n)$ be small then,

$$\begin{aligned} \mathbf{d}_{\mathbf{i}}(n) &\approx \mathbf{M}_{i,j}(\mathbf{x}, n)\mathbf{d}_j(n-1) & (1.2) \\ \mathbf{M}_{i,j} &= \left.\frac{\partial \mathbf{F}_{\mathbf{i}}(x,t)}{\partial x_j}\right|_{\mathbf{x}_1(t)} & (1.3) \end{aligned}$$

The Lyapunov exponents for a mapping, measure how nearby trajectories seperate in time along a reference direction. Negative Lyapunov exponents correspond to contraction of the trajectories in the direction in question, whereas positive exponents represent expansion. In Hamiltonian systems, the sum of these exponents must be 0 to ensure that area is preserved. The largest of these Lyapunov exponent is given by

$$\lambda = \lim_{t \to \infty} \lim_{\mathbf{d}(0) \to 0} \frac{1}{t} \ln \left(\frac{|\mathbf{d}(t)|}{|\mathbf{d}(0)|} \right) \tag{1.4}$$

This expression produces the largest Lyapunov exponent because

$$\lim_{t \to \infty} |\mathbf{d}(t)| = \lim_{t \to \infty} \sqrt{\sum_i \mathbf{d}_i^2(0) e^{2\lambda_i t}} \propto \lim_{t \to \infty} e^{\lambda_{max} t} \tag{1.5}$$

The maximum Lyapunov exponent is the typical rate that two nearby trajectories seperate at, meaning that $\mathbf{d}(t) \approx \mathbf{d}(0) \exp \lambda t$. Hence λ is the typical rate at which experimental (or numerical) errors will propegate in a chaotic system. Because experimental or numerical errors will eventually become significant and prevent accurate predictions, this behavior is called chaos, and $\lambda > 0$ is a necessary and sufficient condition for classical chaos.

This theoretical expression for the Lyapunov exponent is never used in practice since $\mathbf{d}(t)$ grows exponentially and so the perturbed trajectory will only be near the reference trajectory for a short period of time. The growth of these differences causes the linearization approximation to breakdown very quickly. This problem can be corrected by periodically rescaling the differences [33]. The numerical method I use to calculate Lyapunov exponents is described in appendix C.

Classical mechanics is not solely comprised of single particle trajectories. We can also talk about the evolution of ensembles of trajectories or equivalently classical probability densities. This is known as Liouville dynamics and the time evolution is given by the Liouville equation,

$$\frac{\partial \rho(p,q)}{\partial t} = \{H, \rho(p,q)\} = \frac{\partial H}{\partial p}\frac{\partial \rho(p,q)}{\partial q} - \frac{\partial H}{\partial q}\frac{\partial \rho(p,q)}{\partial p} \tag{1.6}$$

Here $\rho(p,q)$ is the probability density of finding a particle with momentum p and position q.

The Liouville equation has two interesting properties that are worth mentioning. The first of these is that area of $\rho(p,q)$ is preserved under time evolution, and the second is that even for a chaotic Hamiltonian, adjacent probability distributions do not separate exponentially. These two properties are important, and will be used in the following section to show that quantum mechanics is conceptually closer to Liouville dynamics than Newtonian mechanics.

1.1.2 Signs of Chaos in Quantum Mechanics

In quantum mechanics a different criteria is needed for chaos since state vectors do not exponentially separate, in fact they do not separate at all. To see this, consider the projection of the state $|\psi\rangle$ onto the state $|\psi'\rangle$

$$\langle\psi(t)|\psi'(t)\rangle = \langle\psi(0)|U^{\dagger}(0,t)U(0,t)|\psi'(0)\rangle = \langle\psi(0)|\psi'(0)\rangle \tag{1.7}$$

As a result of unitarity of time evolution, the overlap of two quantum states remains the same over time and states do not separate like classical trajectories do. However the overlap of classical probability densities also is time independent, suggesting that quantum mechanics has more in common with Liouville dynamics than with single particle trajectories. To show this consider the overlap between two density functions,

$$A = \int\int \rho_1 \rho_2 dpdq \tag{1.8}$$

Assuming A is non-zero then $\rho_1\rho_2$ may be renormalized to a probability distribution ρ_3. Because of the linearity of the Liouville equation this renormalization will not change the solution. Since the Liouville equation preserves the area of the density function, the overlap of the two classical states is preserved if non-zero. If on the other hand the overlap is 0 then let $\rho_3 = \frac{\rho_1 \bigcup \rho_2}{2}$, then since the area of ρ_3 is preserved, ρ_1 can never overlap ρ_2. Since the overlap of 2 classical distributions is also constant as time evolves, the evolution of a state vector has more in common with Liouville than Newtonian dynamics.

Although state vectors do not separate in quantum mechanics, other features can betray the presence of chaos. One well known feature of quantum chaos is level repulsion and the fidelity of the system to random matrix theory. Level repulsion is an effect that causes two adjacent energy levels to avoid each other as the Hamiltonian is perturbed in an attempt to make the levels degenerate. The system's ability to resist this crossing is dependent on the number of free parameters permitted by the Hamiltonian's symmetry class [31].

Random matrix theory assumes that the Hamiltonian for chaotic systems is complicated, and that the eigenvalues and vectors found for chaotic systems should be similar to those found for Hermitian matrices with Gaussian random elements [31]. Random matrix theory cannot predict the individual eigenvalues or vectors for a given Hamiltonian, but it can predict the statistics of ensembles of eigenvectors and eigenvalues for purely chaotic systems. These statistics depend on the degree of level repulsion, which as mentioned above, depends on the symmetry class of the Hamiltonian.

The symmetry class of a Hamiltonian is determined by the group of canonical transformations that will retain the eigenvalues, hermiticity and symmetries of the matrix. These transformations will belong to certain subgroups of the group of $N \times N$ unitary matrices $U(N)$, where N is the dimension of the Hilbert space. It can be shown easily that Hamiltonians which are invariant under time reversal will have canonical transformations that belong to $O(N)$ or the group of orthogonal matrices [31]. For spin 1/2 particles under certain conditions another class called symplectic transformations are canonical. If a Hamiltonian's canonical transformations are not members of either of these subgroups, then the canonical transformations are referred to as unitary.

The degree of level repulsion for matrices of each of these three symmetry classes varies with the number of parameters available to resist a level crossing. Based on the different degrees of level repulsion for these 3 classes of Hamiltonians, random matrix theory predicts that the spacing between adjacent energy levels is distributed according to [31]

$$P(S) = \begin{cases} (S\pi/2)e^{-S^2\pi/4} & \text{orthogonal} \\ (32S^2/\pi^2)e^{-4S^2/\pi} & \text{unitary} \\ (2^{18}S^4/3^6\pi^3)e^{-64S^2/9\pi} & \text{symplectic} \end{cases} \tag{1.9}$$

Here S is the spacing between energy levels in units where the mean energy level spacing is 1.

These predictions of random matrix theory apply to chaotic Hamiltonians, but not to regular systems because of the extra constraints that integrability imposes. It can be shown using torus quantization that integrable systems do not typically exhibit level repulsion, which causes the level spacings to have a Poissonian distribution. There are exceptions to this rule, most notably the harmonic oscillator. However most integrable systems exhibit Poissonian level spacing [24].

Eigenstates for purely chaotic Hamiltonians, tend to be wider in position and momentum than their non-chaotic brethren. This is reasonable because the classically accessible phase space is far wider for chaotic, than for regular systems. Hence if we were to represent a minimum uncertainty state with non-chaotic and chaotic eigenstates, it would require more chaotic eigenstates to represent it than if we were to use non-chaotic eigenstates.

Since each eigenstate has its own eigenfrequency, a minimum uncertainty state will be represented by a large number of eigenfrequencies. Quantum mechanics is inherently periodic because of these eigenfrequencies, although the period may approach infinity in the classical limit. The recursion time is given by the smallest non-zero t that satisfies $\omega_1 t = \omega_2 t = \cdots = \omega_N t$ modulo 2π, where ω_i refers to the eigenfrequency of the i'th eigenstate. As the number of eigenfrequencies increases, the recursion time will also tend to increase. Hence the more eigenfrequencies needed to represent a state the longer the quantum recursion time will be, and so the recursion times should be longer for chaotic systems than for non-chaotic ones.

Although it may take a long time for a complete recursion to occur, if the accumulated phase of some but not all eigenstates are equivalent modulo 2π, then there will be a partial recursion of the QC differences. Since minimum uncertainty states in non-chaotic systems are composed of fewer eigenstates, these partial recurrences will be far more common and lead to differences in expectation values that are visibly periodic. For chaotic systems on the other hand no such periodicity is typically observed. For some chaotic systems, such as the kicked rotor, the QC differences are periodic. However these exceptions again are not typical, and the lack of recursion in chaotic systems is one of the more striking and unambiguous signatures of chaos.

The Schrödinger equation also tends to be less stable in regions that are classically chaotic than in regions that are non-chaotic. A small perturbation to the Hamiltonian for a non-chaotic initial state results in a small perturbation to the solution, however in chaotic regions of phase space these small perturbations can result in rapid separation of the solutions [20, 24].

Although all these characteristics are common to many chaotic systems, there is no single criteria that applies universally to all quantum systems to indicate the presence of chaos. Quantum chaos should not be seen only as a field of study that tries to find signitures of classical chaos in quantum mechanics, but rather it is a field that investigates the interesting and sometimes unique properties of quantum mechanics that arise for complicated Hamiltonians.

1.2 Quantum Classical Differences and The Classical Limit

In this section I will discuss the differences between quantum and classical mechanics, and the different measures that are used to determine when classical mechanics is asymptotically valid. To compare them, I must invoke some form of the correspondence principle, since different versions have different ways of measuring classicality.

One version of the correspondence principle is the Ehrenfest correspondence, which assumes that the classical limit is reached if the centroid of the wave function obeys Newton's equations. This will only be true so long as the wave function is narrow.

This correspondence is thought to be too restrictive, because quantum mechanics typically corresponds to an ensemble of trajectories rather than a single one [9, 19].

Although restrictive, I will examine the Ehrenfest correspondence because it is used as support for Zurek's claim that Hyperion requires environmental interaction to reach the classical limit. To derive Ehrenfest's theorem, consider the expectation values of the Heisenberg equations of motion

$$\begin{aligned} \frac{\partial\langle q(t)\rangle}{\partial t} &= \frac{\langle p(t)\rangle}{m} \\ \frac{\partial\langle p(t)\rangle}{\partial t} &= \langle F(q)\rangle \end{aligned} \tag{1.10}$$

$F(q)$ is the force operator defined through $F(q) = \frac{i}{\hbar}[H,p]$. By Taylor expanding $F(q)$ about the centroid and taking expectation values one obtains

$$\langle F(q)\rangle = F(\langle q\rangle) + \frac{\langle (q-\langle q\rangle)^2\rangle}{2}\frac{\partial^2 F}{\partial q^2}\bigg|_{q=\langle q\rangle} + \cdots \tag{1.11}$$

Hence the centroid of a sufficiently narrow state will obey Newton's equations. Harmonic oscillators serve as a unique example of a system that always obeys Ehrenfest's theorem, since the correction terms will be 0 regardless of the width of the state. Other states will only correspond to a single trajectory until the Ehrenfest breaktime.

For chaotic systems this breaktime is remarkably short. Let us assume that the Ehrenfest correspondence breaks down when $\Delta q = L$ where L is some fixed length. A narrow state's width as a function of time will be on the order of $\Delta q(t) \approx \Delta q(0)e^{\lambda t}$ where λ is the Lyapunov exponent, and $\Delta q(0)$ is the width of the initial state in position. Using the uncertainty principle $\Delta q(0) \approx \Delta p(0)/\hbar$. Using these results we find that the Ehrenfest breaktime occurs at

$$t_{\text{ehr}} \approx \frac{1}{\lambda}\ln\left(\frac{A_0}{\hbar}\right) \tag{1.12}$$

Here $A_0 = \Delta p(0)L$, which is typically assumed to on the order of a system action such as total angular momentum. The above equation varies extremely slowly with $\hbar/A_0$, which must be extraordinarily small for the Ehrenfest breaktime to occur on an unobservably long timescale. In the absence of chaos, this time is typically on the order of the age of the universe [16].

The Ehrenfest correspondence is insufficient to describe the transition between quantum and classical mechanics. Firstly the Ehrenfest breaktime has little to do with quantum mechanics, since $\hbar$ only appears in the width of the initial state and not in the dynamics. Consequently, if I consider a classical probability distribution with $\langle (q - \langle q \rangle)^2 \rangle \propto \hbar$ then I will find the same breaktime even though quantum mechanics is not used in the time evolution [9]. Also the Ehrenfest breaktime typically occurs before the quantum probability distributions deviate from those of a similar classical ensemble [18, 8], hence the Ehrenfest correspondence is too restrictive to measure the transition between quantum and classical mechanics.

If instead I suppose that quantum mechanics corresponds to an ensemble of classical trajectories, then the correspondence principle will hold as long as the quantum and classical probability distributions are approximately the same. This is known as the Liouville correspondence and the time it breaks down at is called the Liouville breaktime. Although the Ehrenfest breaktime is inevitable in chaotic systems, it has been observed in some chaotic systems [7, 19] that the Liouville breaktime does not occur.

For some systems the classical distributions do not emerge in a pointwise sense out of quantum mechanics, but require some averaging process to do so. The two most common justifications for smoothing out these quantum classical differences are coarse graining and decoherence. The proponents of coarse graining claim that quantum effects typically occur on a scale that is too fine to experimentally resolve. This view has been adopted by Ballentine [5, 3], Takahashi [41], and Casati and Cherikov [12].

Others believe that the classical probability distribution is reached by interaction with the environment, which diffuses the probability distributions and tends to eliminate quantum effects. This view is supported by work by Zurek and Paz [47], Habib [26], Pattanayak Sundaram and Greenbaum [36] and Kolovsky [29]. The debate about which of these two mechanisms provides the correct explanation for the emergence of classicality continues, and this work will try to clarify the differences between the two views.

1.3 Wigner and Husimi Distributions

1.3.1 Wigner Function

In classical mechanics I can construct a phase space distribution $\rho(p,q)$ that gives the probability of finding the system in the square $(p, p+dp), (q, q+dq)$, and satisfies $\int \rho(p,q)dp = P_c(q), \int \rho(p,q)dq = P_c(p)$ where $P_c(q), P_c(p)$ are the marginal classical position and momentum probability distributions. In quantum mechanics we do not have a quantum phase space probability density equivalent to the Liouville density. However we can construct a quasi-probability density called the Wigner function that is deceptively similar to the Liouville density.

The Wigner function $\rho^w(p,q)$ is an intermediate between position and momentum representation containing information about both, and is defined through either of the following equations

$$\begin{aligned} \rho^w(p,q) &= \frac{1}{2\pi\hbar}\int e^{ipq'/\hbar}\langle q-q'/2|\hat{\rho}|q+q'/2\rangle dq' \\ \rho^w(p,q) &= \frac{1}{2\pi\hbar}\int e^{-ip'q/\hbar}\langle p+p'/2|\hat{\rho}|p-p'/2\rangle dp' \end{aligned} \tag{1.13}$$

Like the classical probability density, $\int \rho^w(p,q)dp = P(q), \int \rho^w(p,q)dq = P(p)$.

Although analogous to the classical probability distribution, it is not equivalent because the Wigner function can take on negative values and does not generally have a probability interpretation. In fact from a theorem due to Hudson [27], Gaussian states are the only pure states that have a non-negative Wigner function. So we must either restrict the classically permitted states to a small set of mixed states, or concede that the Wigner function is only a quasi-probability distribution that does not have an equivalent classical quantity.

Despite its lack of a probability interpretation, the divergence of $\rho^w(p,q)$ from $\rho(p,q)$ is used to estimate the breakdown of classical behavior in quantum systems [47, 36] because of the similarity of $\rho^w(p,q)$'s time evolution to the Liouville equation [4],

$$\dot{\rho}^w = \{H, \rho^w\} + \sum_{n=1}^{\infty} \frac{\hbar^{2n}}{2^{2n}(2n+1)!}\frac{\partial^{2n+1}V(x)}{\partial x^{2n+1}}\frac{\partial^{2n+1}\rho^w}{\partial p^{2n+1}} \tag{1.14}$$

Eq. (1.14) is the Liouville equation with quantum correction terms added. These corrections are collectively known as Moyal terms. If the initial Wigner function is the initial classical probability density, then $\rho^w(p,q)$ will no longer follow the Liouville equation when these Moyal terms become comparable to the Poisson bracket, allowing us to estimate when the Liouville breaktime occurs.

1.3.2 Husimi Distribution

This lack of a probability interpretation is a major defect of the Wigner function, but if the negativity of the distribution can be removed by integrating over position or momentum then we must ask ourselves if it is possible to find another way to remove this negativity? It turns out that a modest amount of Gaussian smoothing also makes the Wigner function non-negative. This smoothed Wigner function is known as the Husimi distribution which is defined as

$$\rho_H(q,p) = \int\int \rho_w(q',p') \exp(-(p'-p)^2/2a^2 - (q-q')^2a^2) dq'dp' \qquad (1.15)$$

It is not clear in this form that the Husimi distribution will yield a non-negative probability density. However it will because $\rho_H(p,q)$ gives the probability of finding a state $|\psi\rangle$ in a minimum uncertainty coherent state centered at $\{p,q\}$. I will denote this state $|p,q\rangle$. Since the Wigner function of a Gaussian is also a Gaussian, the Gaussian used to smooth the distribution can be expressed as the Wigner transform of $|p,q\rangle$ and as such Eq. (1.15) can be re-written as

$$\rho_H(q,p) = \int\int\int\int \exp(ip'q''/\hbar)\langle q' - q''/2|\psi\rangle\langle\psi|q' + q''/2\rangle \exp(ip'q'''/\hbar) \\ \langle q' - q'''/2|p', q'\rangle\langle p', q'|q' + q'''/2\rangle dq'''dq''dq'dp' \tag{1.16}$$

Using orthogonality [4], the above expression may be simplified considerably to

$$\rho_H(q,p) = \frac{1}{2\pi\hbar}|\langle q,p|\psi\rangle|^2 \tag{1.17}$$

This shows that the Husimi distribution is proportional to the probability of finding the system in the minimum uncertainty state $|q,p\rangle$. Because the Hussimi distribution does not allow a measurement that defies the uncertainty principle and because it is non-negative, it is more natural to compare to the Liouville density to $\rho_H(p,q)$ than to $\rho^w(p,q)$. This comparison is only valid in the classical limit, since this Gaussian smoothing may significantly alter the probability distributions if $\hbar$ is not significantly smaller than a typical system action.

1.4 Decoherence

In open systems quantum effects are particularly susceptible to dissipation due to environmental interactions. Decoherence is a quantum effect that occurs in these systems where the environment causes off-diagonal elements of the density matrix to rapidly decay, and causes the Wigner function to be predominantly non-negative [43, 26]. This decay tends to be very rapid, causing interference patterns to quickly vanish. Because environmental interactions cause these interference patterns to lose phase coherence and decay, this decay process is known as decoherence.

I will not be able to do justice to the field of open quantum systems and decoherence here, but we will endeavor to review the basic principles so that the reader can get an idea of how we expect quantum mechanics in open systems to behave. This is important to put our work into context, so that we can contrast decoherence effects with what we find by coarse graining the probability distributions.

In an open system the Hamiltonian can be broken into three parts,

$$H = H_{\text{sys}} + H_{\text{env}} + H_{\text{int}} \tag{1.18}$$

Where H_{sys} is the system Hamiltonian, H_{env} is the Hamiltonian for the environment, and H_{int} is the interaction potential between the system and its surroundings.

The environment is typically modeled by a thermal field composed of an infinite number of Harmonic oscillator modes [43, 2, 44]. It is assumed that the observer has the ability to prepare the system in any manner desired but the environment is not under their control. Because the environment is randomly prepared for each measurement, the observed distributions will be an average over all possible environmental interactions. After reducing the Hilbert space by tracing over all environmental variables, the reduced Wigner function of the system obeys [43]

$$\dot{\rho^w} = \{H_{\text{sys}}, \rho^w\} + \sum_{n=1}^{\infty} \frac{\hbar^{2n}}{2^{2n}(2n+1)!} \frac{\partial^{2n+1} V(x)}{\partial x^{2n+1}} \frac{\partial^{2n+1} \rho^w}{\partial p^{2n+1}} + 2\gamma \frac{\partial p \rho^w}{\partial p} + D \frac{\partial^2 \rho^w}{\partial p^2} \tag{1.19}$$

Here γ is the damping coefficient and D is the momentum diffusion parameter. D is the parameter relevant to decoherence, and γ is often neglected because the damping timescale is far longer than the timescale decoherence occurs on. This master equation is very similar to the classical Fokker Planck equation for Brownian motion [14], and so the thermal effects should diffuse ρ^w in a fashion analogous to the Gaussian smoothing used to construct the Hussimi distribution. This has been observed in other systems to result in a predominantly non-negative Wigner function [26], and eliminate fine scale behavior that causes $\rho^w(p, q)$ to deviate from the classical density $\rho(p, q)$. Subsequent work by Habib et. al. [25] suggests that decoherence will not remove all the negative regions in the Wigner function, so environmental interactions will not cause it to have a probability interpretation.

Most studies of decoherence involve Schrödinger's cat states, which correspond to two separated coherent states with an interference pattern between them. The Wigner function for these states is [4]

$$\begin{aligned} \rho^w = \frac{1}{2\pi\hbar} e^{-p^2/[2(\Delta p)^2]} \Big[& e^{-(q-d)^2/[2(\Delta q)^2]} + e^{-(q+d)^2/[2(\Delta q)^2]} + \\ & 2\cos(2pd/\hbar) e^{-q^2/[2(\Delta q)^2]} \Big] \end{aligned} \tag{1.20}$$

Here $2d$ is the separation between the Gaussian wave packets, Δq and Δp are their widths in position and momentum respectively. This Wigner function can be divided into two pieces $\rho^w = \rho + \rho_{int}$ where ρ is the phase space density of the two Gaussian states, and ρ_{int} is the interference pattern between the two. As $d/\hbar$ increases the interference pattern will increase in frequency, leading to very rapid interference terms for macroscopic separations. For macroscopic values of d these rapid oscillations in ρ_{int} are more susceptible to smoothing than the broad Gaussians in ρ, suggesting that the environment will selectively eliminate quantum effects and leave the classical structure largely intact.

If classicality is reached through decoherence, the quantum effects must dissipate on a timescale that is far shorter than the classical timescale. The decoherence time scale is referred to in the literature as the decoherence time or T_2. The decoherence times typically depend on the system Hamiltonian, so the timescales mentioned in [43] will not apply to our work. Strunz et. al. [40] suggest that when decoherence is faster than the system timescale or even the environmental timescale, the decoherence times are independent of the system potential. This occurs because if the system timescale is slow compared to the decoherence timescale, then the system Hamiltonian will be approximately constant during the short decoherence time. This approximation leads to three different decoherence times for Schrodinger's cat states with two Gaussians separated in both position and momentum.

These three time scales are denoted $\tau_d^Q, \tau_d^P, \tau_d^{QP}$. The timescale τ_d^Q refers to the decoherence time for two coherent states separated only in position, τ_d^P is the decoherence time for two states separated only in momentum, and τ_d^{QP} is the decoherence time for states that are equally separated in both position and momentum. These vary with $\hbar$ and the separations as follows

$$\begin{aligned}
\tau_d^Q &= \frac{\hbar}{|q_1 - q_2|\sqrt{\langle B^2 \rangle}}, \\
\tau_d^{QP} &= \left(\frac{M\hbar^2}{2|q_1 - q_2||p_1 - p_2|\langle B^2 \rangle} \right)^{1/3}, \\
\tau_d^P &= \left(\frac{4M^2\hbar^2}{(p_1 - p_2)^2 \langle B^2 \rangle} \right)^{1/4}
\end{aligned} \tag{1.21}$$

Here M is the mass of the system that interacts with the environment. B represents the set of environmental variables $\{B_i\}$. The environment is often a thermal field, so $\{B_i\}$ usually represents a set of photon number operators. $\{q_1, p_1\}, \{q_2, p_2\}$ are the coordinates of the centroids of the two coherent states. For a general Schrodingers cat state, the separation between the two Gaussians can be arbitrary. This means that any of these 3 timescales can be the dominant one, since a particular value of $|q_1 - q_2|, |p_1 - p_2|$ can always be chosen to make any of these timescales the fastest.

The utility of Schrödingers cat states in studies of decoherence is twofold. First, they are composed of Gaussians which can be dealt with using path integrals. Second, the interference patterns generated by these two states are mono-chromatic. This allows us to look at how the environment eliminates single frequency quantum classical differences. This is not typical for most systems, since there are typically a large number of frequencies present. So we cannot expect there to be a unique decoherence timescale even in the limit of very rapid decoherence.

For Hyperion these decoherence timescales for macroscopic separations are incredibly short because of the mass of the satellite is so large, but since these times are derived only for Schrödinger's cat states they may not be generic. But it stands to reason that since there is nothing unique about the interference patterns in these states, the decoherence times for generic interference patterns also should also obey a power law in $\hbar$.

1.5 Liouville Breaktimes For Chaotic Systems

1.5.1 Liouville Breaktime Without Thermal Effects

In 1998 Zurek et al suggested that the Liouville breaktime for chaotic systems is dramatically shorter than the Liouville breaktime for integrable ones [46]. It is important to review this argument, since if it was ironclad then there would be no question that thermal effects are needed to understand why Hyperion appears classical. So here I will summarize Zurek's argument, and show that we may not need decoherence to understand why classicality emerges.

His estimate was made by determining how long it would take a classical phase space distribution to fold its self sufficiently for the Moyal terms in Eq. (1.14) to become non-negligible. From Eq. (1.14), the n^{th} Moyal term is proportional to $\hbar^{2n}\frac{\partial^{2n+1}V}{\partial x^{2n+1}}\frac{\partial^{2n+1}\rho^{w}}{\partial p^{2n+1}}$. Hence the quantum corrections depend on two factors: the scale of the structure of the probability distribution in momentum and the scale in position that the potential is non-linear. Using these ideas of scale, $\frac{\partial^{2n}V}{\partial x^{2n}} \approx \chi^{-2n}V$ and $\frac{\partial^{2n}\rho^{w}}{\partial p^{2n}} \approx [\sigma_p]^{-2n}$. Here σ_p is the scale in momentum over which ρ^w exhibits structure, and the length scale associated with potential non-linearities is χ. This means that the Moyal corrections are on the order of

$$\hbar^{2n}\frac{\partial^{2n+1}V}{\partial x^{2n+1}}\frac{\partial^{2n+1}\rho^{w}}{\partial p^{2n+1}} \approx \frac{1}{\chi\sigma_p}\left(\frac{\hbar}{\chi\sigma_p}\right)^{2n} \tag{1.22}$$

The classical terms in the Moyal expansion are given by the Poisson bracket $\{H, \rho(p,q)\} =$

$\partial_p H \partial_q \rho - \partial_q H \partial_p \rho \approx [\chi\sigma_p]^{-1}$. This characteristic scale can be factored out of the classical and quantum terms, and so the Moyal corrections are proportional to $(\hbar/\sigma_p\chi)^{2n}$.

Because the Liouville equation is area preserving, as the distribution spreads it must also become narrower. This narrowing will cause the momentum to vary over a fine scale as time proceeds, and so σ_p will diminish as time advances. Hence $\sigma_p(t) \approx \sigma_p(0)e^{-\lambda t}$ where λ is the largest Lyapunov exponent, and so $\frac{\partial \rho^w}{\partial p} \approx [\sigma_p(0)]^{-1}e^{\lambda t}$. Thus the time it takes for the first quantum correction to be non-negligible is

$$\tau_b \approx \frac{1}{\lambda}\ln\left(\frac{\chi\sigma_p(0)}{\hbar}\right) \tag{1.23}$$

Here $\sigma_p(0)$ measures the variance of the initial quantum state in momentum, and χ measures the non-linearity of the potential.

This breaktime is similar to the Ehrenfest prediction in Eq. (1.12), and as a result the Ehrenfest estimate was used to calculate the Liouville breaktime for Hyperion [46]. To find the Ehrenfest time the characteristic action was purposefully over estimated as the orbital energy multiplied by the period: $A_0 \approx 2.8 \times 10^9 Js$. From this the Ehrenfest breaktime was calculated to be approximately 20 years and it was assumed that the Liouville breaktime is comparable.

This characteristic action is an overestimate since the chaotic behavior is in the rotation of the body, not its orbit. However because the breaktime is proportional to $\ln(A_0/\hbar)$, even if A_0 is incorrect by a factor of 100 the breaktime will vary by less than a year. Hence the value of the action is less important to this estimate than the fact that τ_b varies as $\ln(1/\hbar)$.

1.5.2 Thermal Effects

This breaktime occurs because the probability distribution will continue to fold its self until the Moyal terms become comparable to the Poisson bracket. However thermal effects will create a minimum scale on which the Wigner function can vary in momentum. Pattanayak et al [35, 34] argue that this scale is formed by two competing processes in chaotic open systems, namely the narrowing of the density function that chaos causes and diffusion due to the environment. This spreading does not significantly effect the expansion along the eigenvectors corresponding to positive Lyapunov exponents, but it opposes the narrowing along the directions of the negative Lyapunov exponents. From considerations of entropy production rates of these two processes, they will counteract each other when $\frac{\partial \rho^w}{\partial p} \approx \sqrt{\frac{\lambda}{2D}}$ where D is the momentum diffusion parameter. Hence the Moyal terms in Eq. (1.12) can never become large, and so they should not exhibit the runaway growth predicted in the absence of decoherence. This claim is reinforced by numerical studies by Zurek and Pattanayak [26, 36].

According to this argument, decoherence should suppress quantum-classical differences, but it is not clear what these differences are, or whether they need suppression. Even if these differences are large, if most of them occur on a fine scale, then decoherence may only be destroying interference patterns that are too difficult to observe.

Hence Zurek's argument does not conclusively show that Hyperion needs environmental interactions to appear classical. This means that the validity of his claims can only be tested by invoking a model for Hyperion, and seeing whether or not the quantum-classical differences should be observable for the satellite in the absence of environmental interactions.

1.6 Outline

This thesis will proceed as follows, Chapter 2 describes the model for Hyperion's rotation in 1 dimension. It also contains the classical equations of motion, the corresponding Schrödinger equation, and the equations for the initial classical and quantum states.

Chapter 3 and Chapter 4 examine how the differences between quantum and classical mechanics vary as the classical limit is approached, for both regular and chaotic states. The differences in expectation values and for probability distributions are considered in the limit as $\hbar \rightarrow 0$. The fractal behavior of the quantum probability distribution is also addressed.

Chapter 5 shows how environmental effects are handled in this work, as well as how they affect QC differences in the classical limit. The differences in probability distributions, with and without environmental interactions are also examined through Fourier analysis to determine whether decoherence is a form of coarse graining.

Chapter 6 examines the structure of quasi-energy or Floquet states for Hyperion. The scaling of participation numbers for minimum uncertainty states is considered as $\hbar \rightarrow 0$, and the structure of Floquet states is used to explain the differences noted in Chapter 3. Finally the spacing of quasi-energy levels for regular and chaotic systems is also examined.

Chapter 7 investigates the 3D rotation of Hyperion. A set of quaternionic coordinates are introduced to examine the tumbling of the satellite. The classical equations of motion are presented, and estimates are made of Hyperion's Lyapunov exponent. A foray is made into the 3D quantum mechanics, and it is shown that the 3D quantum calculation is too difficult to get sufficiently far into the classical limit to be meaningfully contrasted with the classical result. Finally an estimate of how long Hyperion's rotation can remain 1D due to quantum uncertainty is made.

Chapter 2

Model

Our model of Hyperion's rotation was first suggested in 1988 by Wisdom [45]. It assumes that Hyperion travels in an elliptical orbit about Saturn, and that its orbit is independent of its rotation. However since Hyperion is an extended object, Saturn's gravitational field is not constant over its volume. For a body without a symmetric mass distribution, the variation in the gravitational field can lead to a net torque. To lowest order in a multipole expansion of the mass distribution, this torque depends on the quadrupole moments of the mass distribution, and for simplicity we neglect all higher order moments.

It should be noted that this configuration is attitude unstable, and so small inclinations of I_3 towards the plane of the orbit will tend to grow. However this simplifying assumption makes the quantum mechanical computations feasible.

The coordinate system is shown in Fig. 2.1. The space-fixed x-axis is along the semi-major axis of the orbital ellipse, and the z-axis is perpendicular to the orbital plane. The angle θ denotes the position of the satellite in the orbit. The axis of the smallest moment of inertia (I_1), makes an angle ϕ with respect to the x-axis, hence the angle between the body axis of I_1 and the radius vector $\vec{r}$ is $\phi - \theta$. The largest moment of inertia I_3 is parallel to the z-axis. The canonical coordinates for this system are the angular momentum and the orientation of the satellite $\{L_z, \phi\}$.

The coupling of the gravitational field to the satellite is obtained by a Taylor expansion of the potential about the satellite's center of mass,

$$H = \frac{L_z^2}{2I_{zz}} + \sum_i \sum_j \int \rho(\vec{r}) x_i x_j d^3x \left. \frac{\partial^2 V}{\partial x_i \partial x_j} \right|_{\vec{x}=0} + \cdots \tag{2.1}$$

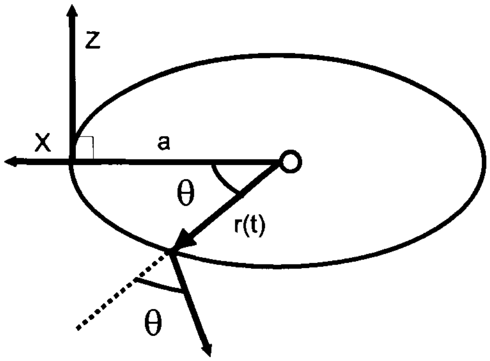

Figure 2.1: Position of satellelite spinning about the z-axis perpendicular to i^{th} orbital plane. θ denotes the position of the satellite on the orbit, and ϕ is the orientation of the satellite with respect to the semi-major axis of the orbit.

Here x_i refers to the distance along the i'th space-fixed axis from the center of mass of the satellite.

$$\left.\frac{\partial^2 V}{\partial x_i \partial x_j}\right|_{\vec{x}=0} = \text{diag}\left[\frac{2Gm}{r^3}, \frac{-Gm}{r^3}, \frac{-Gm}{r^3}\right] \tag{2.2}$$

Here m is the mass of the gravitational source (Saturn), and r is the distance from the source to the satellite. The first order term in Eq. (2.1) vanishes because the expansion is about the center of mass, and the second order term is related to the moments of inertia tensor,

$$I_{ij} = \int \rho[x^2\delta_{ij} - x_i x_j] d^3x \tag{2.3}$$

Using Kepler's third law, which states $GM/a^3 = 4\pi^2/T^2$, the Hamiltonian becomes

$$H = \frac{L_z^2}{2I_3} - \frac{3\pi^2}{T^2}\left(\frac{a}{r(t)}\right)^3 (I_2 - I_1)\cos(2[\phi - \theta(t)]) \tag{2.4}$$

Here T is the orbital period, a is the length of the semi-major axis of the orbit, L_z is the angular momentum about the z-axis, $I_3 = I_{zz}$ is the moment of inertia for rotations in the orbital plane, and r(t) and $\theta(t)$ are the orbital coordinates of the satellite, which are functions of the period T and the eccentricity e. These functions are found by numerically integrating the equations of motion for the center of mass, using the code provided in [11].

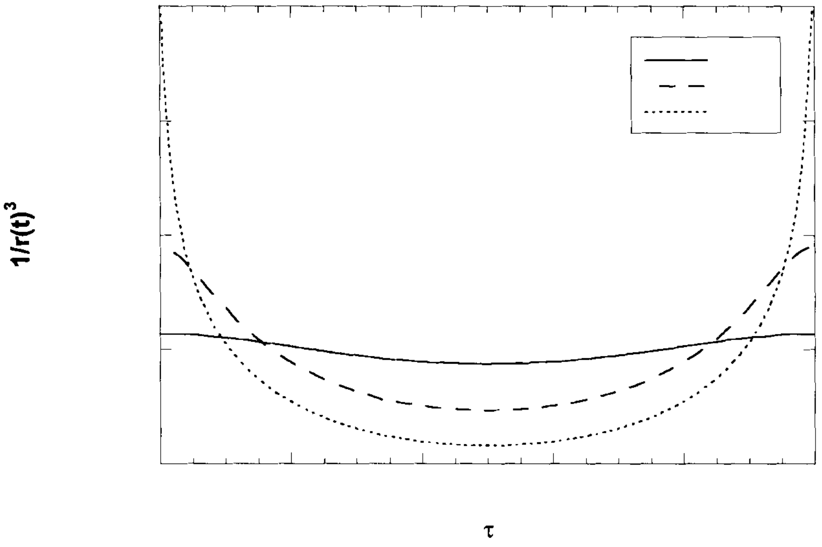

Figure 2.2: Plot of $1/[r(\tau)]^3$ vs τ for different values of e. This shows that in the high eccentricity limit, the potential energy approaches a delta function in time as $e \rightarrow 1$.

In the limit of high eccentricity, the satellite will spend most of its time far away from the planet and only a very brief period of time close to it. This tendency can be seen in figure 2.2. Since the gravitational gradient potential is proportional to $1/[r(\tau)]^3$, in the limit as $e \rightarrow 1$, the model approaches a delta kicked rotor. The connection between our model and the kicked rotor is important, because it is one of the most studied models in quantum chaos and its features may appear in the rotation of bodies with highly eccentric orbits such as comets. However from the Fig. 2.2, for Hyperion's eccentricity $e = 0.1$, $1/[r(\tau)]^3$ does not resemble a delta function and so we expect little similarity between our results for Hyperion and the kicked rotor.

2.1 Classical Equation Of Motion

It is convenient to express the equation of motion in terms of dimensionless variables. We introduce the anisotropy parameter,

$$\alpha = \frac{(I_2 - I_1)}{I_3} \tag{2.5}$$

a dimensionless time (in units of the orbital period),

$$\tau = t/T \tag{2.6}$$

and a dimensionless angular momentum J_z in terms of the dimensional angular momentum L_z

$$J_z = \frac{L_z T}{I_3} \tag{2.7}$$

To estimate α for Hyperion, we use the observed lengths of its principle axes (410 ± 10, 260 ± 10, 220 ± 10 km, see [42]), and assume that it is an ellipsoid of uniform mass density. Hence

$$I_3 = \frac{M}{5}(r_1^2 + r_2^2) \tag{2.8}$$

Here r_i is half the length of the i^{th} principle axis of the ellipsoid. The other moments of inertia are obtained by cyclically permuting the indices. Substituting Eq. (2.8) into Eq. (2.5) yields

$$\alpha = \frac{r_1^2 - r_2^2}{r_1^2 + r_2^2} \tag{2.9}$$

Hence $\alpha = 0.43 \pm 0.04$. In this work we used a slightly larger value, $\alpha = 0.5$, because it leads to a more purely chaotic motion, whereas for $\alpha = 0.43, e = 0.1$ there are large regular islands embedded in the chaotic sea. We wish to compare chaotic motions with regular motions, and the differences would be obscured by a mixed phase space.

Following Wisdom [45], we obtain the equation of motion (in dimensionless variables) to be

$$\begin{aligned} \dot{\phi} &= J_z \\ \dot{J}_z &= -6\pi^2 \left(\frac{a}{r(\tau)}\right)^3 \alpha \sin(2[\phi - \theta(\tau)]) \end{aligned} \tag{2.10}$$

2.2 Quantum Mechanics

The quantum mechanics will be solved by integrating the Schrödinger equation in angular momentum representation. The state vector is written as

$$|\psi(t)\rangle = \sum_m c_m(t)|m\rangle, \tag{2.11}$$

with $|m\rangle$ being an angular momentum eigenstate. The matrix elements of the Hamiltonian are

$$\langle m|\hat{H}|\psi\rangle = \frac{\hbar^2 m^2 c_m}{2I_3} - \sum_n \frac{3\pi^2}{2T^2} c_n \left(\frac{a}{r(t)}\right)^3 \times \\ (I_2 - I_1)\frac{1}{2\pi}\int_0^{2\pi} (e^{i(n-m+2)\phi} e^{-2i\theta} + e^{i(n-m-2)\phi} e^{2i\theta}) d\phi \tag{2.12}$$

Using (2.12) and (2.11), the matrix equation $\langle m|\hat{H}|\psi\rangle = i\hbar\langle m|\frac{\partial}{\partial t}|\psi\rangle$ becomes

$$i\hbar\frac{\partial c_m(t)}{\partial t} = \frac{\hbar^2 m^2 c_m}{2I_3} - \frac{3\pi^2}{2T^2}\left(\frac{a}{r}\right)^3 (I_2 - I_1) \times \\ (c_{m+2} e^{2i\theta(t)} + c_{m-2} e^{-2i\theta(t)}) \tag{2.13}$$

In addition to the dimensionless parameters τ and α, we now introduce a dimensionless $\hbar$ parameter,

$$\beta = \frac{\hbar T}{I_3} \tag{2.14}$$

The dimensionless Schrödinger equation then becomes

$$i\frac{\partial c_m}{\partial \tau} = \frac{\beta m^2 c_m}{2} - \frac{3\pi^2}{2}\frac{\alpha}{\beta}\left(\frac{a}{r(\tau)}\right)^3 \times \\ (c_{m+2} e^{2i\theta(\tau)} + c_{m-2} e^{-2i\theta(\tau)}) \tag{2.15}$$

A peculiar feature of Eq. (2.15) is that the coefficient c_m depends only on c_{m+2} and c_{m-2}, therefore the even c_m cannot interact with odd c_m. This coupling arises from the invariance of the Hamiltonian under rotations by π. But octapole and other odd moments are not invariant under rotations by π, so this symmetry is an artifact of the model.

2.3 Initial State

The initial quantum state is chosen to be a Gaussian in angular momentum,

$$|\psi\rangle = \sum_m \exp\left(-\frac{(\beta m - J_0)^2}{2\delta^2} - i\phi_0 m\right)|m\rangle \tag{2.16}$$

Here βm is a dimensionless angular momentum, J_0 is the average of the dimensionless angular momentum in the state, δ is its standard deviation, and ϕ_0 is the central angle of the initial state. These parameters will be varied to ensure that the initial states are in regions of phase space that are either purely chaotic or purely regular.

In principle, the sum is from $m = -\infty$ to $+\infty$, but in practice it is restricted to a range $\{-K \cdots K\}$. The value of K must be chosen so that this range includes all of the values of J_z that have significant amplitudes in the time-dependent state. By examining phase-space diagrams for the classical distributions, we find that $|J_z| < 20$ for all time, and so $K = 20/\beta$ is sufficient to contain the quantum distribution.

The initial classical probability distributions are chosen so that they match the angular momentum and angular distributions for the initial quantum state. Because the initial state is a minimum uncertainty state with fixed width in angular momentum, its width in angle is proportional to β. Thus β (dimensionless $\hbar$) enters into the classical calculation to ensure that the initial quantum and classical states correspond to each other.

As $\beta \longrightarrow 0$ the initial state's width in momentum is fixed, but its width in position vanishes. Because the state's width in momentum doesn't vanish in the classical limit, the state can not be interpreted as a single particle trajectory. As a result this work examines the Liouville rather than the Ehrenfest correspondence, and I will not discuss how single particle trajectories appear in the classical limit.

Chapter 3

Results for a Non-Chaotic State

The classical limit of the quantum tumbling of a satellite will now be examined for a non-chaotic state, to determine whether there is a qualitative difference between chaotic and non-chaotic systems in their approach to classicality.

Non-chaotic motion is ensured by choosing a circular orbit: $e = 0$, $r(\tau) = a$, $\theta(\tau) = 2\pi\tau$. The time dependence in Eq. (2.10) can be transformed away by the substitution $\Phi = \phi - 2\pi\tau$, yielding an integrable equation of motion,

$$\ddot{\Phi} = -6\pi^2\alpha\sin(2\Phi) \tag{3.1}$$

Fixed points for this equation occur at the angles $\Phi = 0, \frac{\pi}{2}, \pi, \frac{3\pi}{2}$. These fixed points describe motions in which Hyperion presents the same face to Saturn at all times. The stable fixed points correspond to the smallest moment of inertia pointing towards Saturn.

The initial state was chosen to be far from the unstable fixed point. It is centered at $J_0 = 4$, with a standard deviation in J_z of $\sigma = \frac{1}{\sqrt{2}}$ (see Fig. 3.1), and a central angle ϕ_0 equal to zero.

3.1 QC Differences in $\langle J_z \rangle$

The classical probability distributions are found by time evolving a finite ensemble of systems, using Eq. (2.10). The distributions of J_z and ϕ are found by randomly choosing the angular momentum and orientation of each member of the ensemble from probability distributions in J_z and ϕ that correspond to the initial quantum

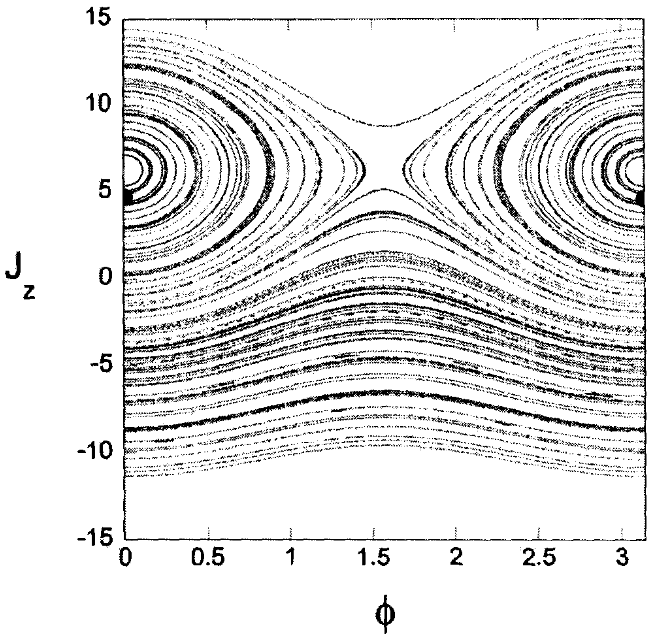

Figure 3.1: Poincare Section for $e = 0$, $\alpha = 0.5$. Black circle denotes a typical initial state.

state. For notational simplicity I will define $\Delta\langle J_z\rangle$ to be the difference between the quantum and classical expectation values in angular momentum.

The finiteness of the ensemble leads to statistical errors, which may be reduced by increasing its size. The standard deviation of the fluctuations in the mean is

$$\sigma_m = \frac{\sigma}{\sqrt{n}} \tag{3.2}$$

Here n is the number of members in the ensemble, σ is their standard deviation of the distribution. Any difference between the computed mean values of the quantum and the classical variables is not significant unless it is larger than σ_m. Ensembles of 10^6 to 2×10^6 particles were used to ensure that $\Delta\langle J_z\rangle$ is greater than σ_m, and the tolerance of the integrator routine was chosen so that decreasing the tolerance by a factor of 10 did not significantly change the results.

As $\beta \to 0$ $\Delta\langle J_z\rangle$ becomes smaller, and thus a larger ensemble is needed to reduce the statistical errors below that level. Hence different ensemble sizes were used for different values of β in Fig. 3.2. The ensemble sizes were chosen so that $\sigma_m = \{2 \times 10^{-4}, 7 \times 10^{-4}, 2 \times 10^{-3}\}$ for $\beta = \{0.0125, 0.05, 0.5\}$.

Ensembles were evolved for several values of β, ranging from $\beta = 0.5$ to $\beta = 0.002$.

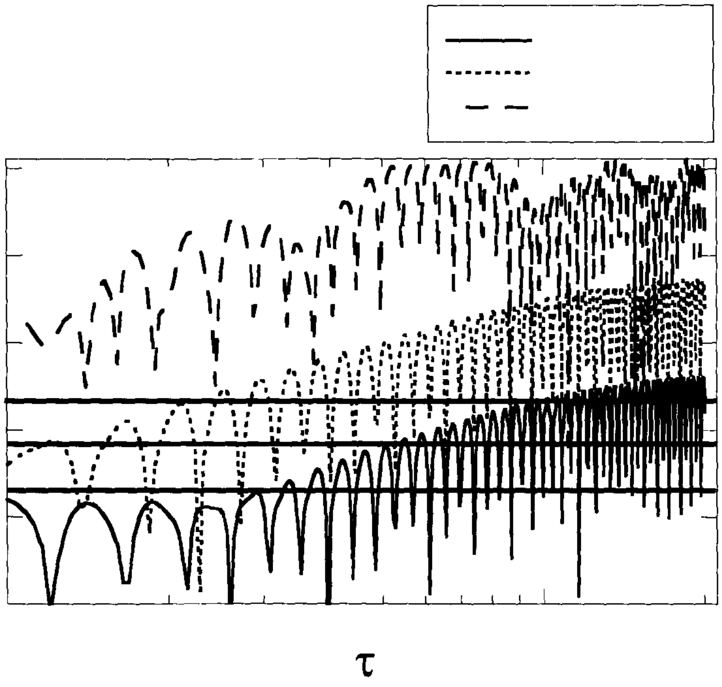

Figure 3.2: $\Delta\langle J_z\rangle$ vs τ, for several β, with $e = 0$, $\alpha = 0.5$. For $\beta = \{0.0125, 0.05, 0.5\}$ the statistical errors are $\sigma_m = \{2 \times 10^{-4}, 7 \times 10^{-4}, 2 \times 10^{-3}\}$. The black lines show the values of these statistical errors.

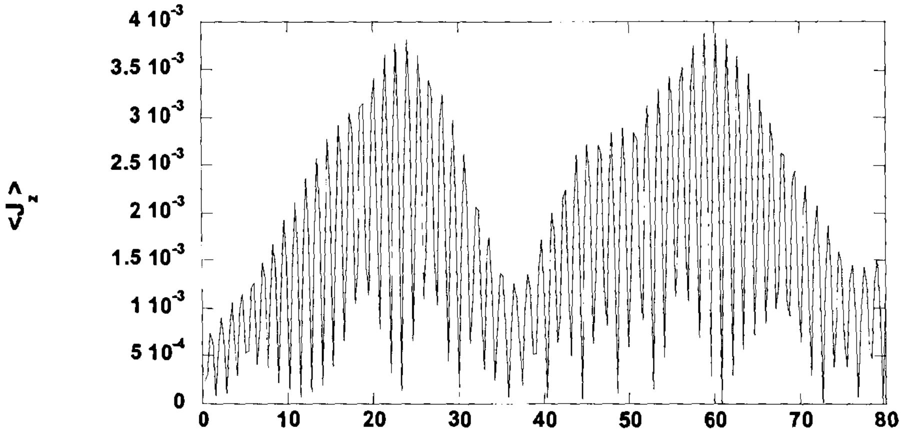

Figure 3.3: $\Delta\langle J_z\rangle$ for $\beta = 0.0125$, with $e = 0$, $\alpha = 0.5$, $\sigma_m = 0.7 \times 10^{-3}$

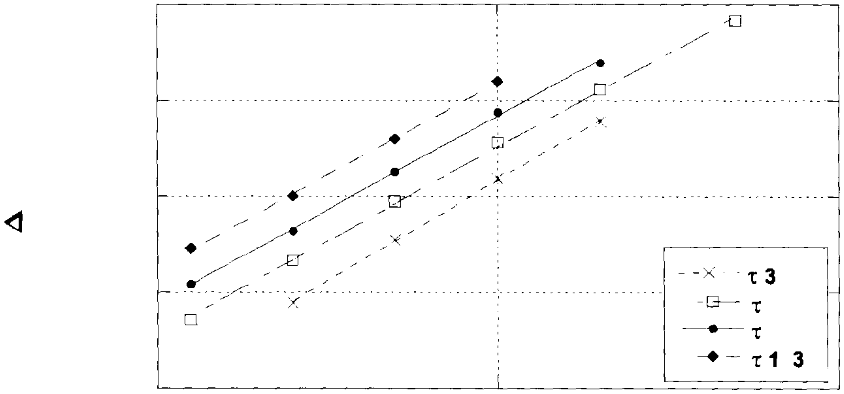

Figure 3.4: Scaling of $\Delta\langle J_z\rangle$ with β for early times, with $e = 0$, $\alpha = 0.5$. This shows that $\Delta\langle J_z\rangle$ is proportional to β^2.

For $\beta < 0.01$ $\Delta\langle J_z\rangle$ is far smaller than σ_m for any computationally feasible ensemble sizes, so no data will be presented for $\beta < 0.01$.

A plot of $\Delta\langle J_z\rangle$ versus time is shown in Fig. 3.2. In this and similar figures, any value of $\Delta\langle J_z\rangle$ smaller than σ_m should be ignored, since they are dominated by statistical errors. $\Delta\langle J_z\rangle$ oscillates on the scale of the driving force, and only the envelope of these oscillations is of intererest. From figure 3.2, it is apparent that at early times the envelope of the $\Delta\langle J_z\rangle$ grows as τ^2. For longer times the envelope of the QC differences is oscillatory, as can be seen in Fig. 3.3. Such recurrences are typical for non-chaotic systems [24]. Fig. 3.4 shows that, for fixed times, the QC differences in $\langle J_z\rangle$ scale as β^2.

This result has been observed in other systems. In [8] Ballentine and McRae perform a moment expansion of the Liouville equation and the Heisenberg equation of motion for a particle. They find that the differences between the equations of motion of the centroids are proportional to $\hbar^2$ for some two dimensional systems. As a specific example of they examine Henon-Heiles potential, and that $\Delta\langle J_z\rangle$ scales as $\hbar^2$, and the QC differences were found to increase as a polynomial in time for regular states. This potential is quite different from ours since it is two dimensional, in addition it is autonomous as opposed to our driven system.

Despite these differences, this work shows that the QC differences for our model of

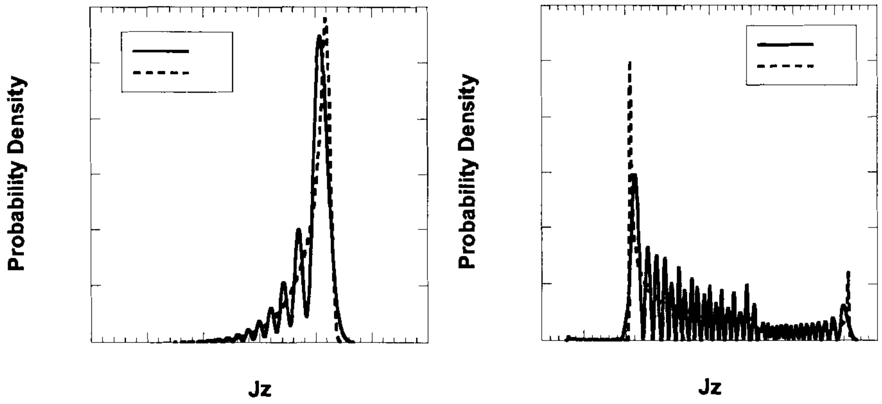

Figure 3.5: Quantum and classical probability distributions for $\tau = 2, 20$ with $e = 0$, $\alpha = 0.5$

Hyperion are typical for narrow regular states. This is important because we want to determine how the classical limit is reached in this model, and determine if we must introduce any new concepts to understand the classical limit of chaotic states.

3.2 QC Differences in Distributions

The differences in $\langle J_z \rangle$ alone are insufficient to fully describe the differences between quantum and classical systems because two different probability distributions can have the same mean but different variances and higher moments. We shall now examine the differences between probability distributions, and how they scale with β.

Since the angular momentum distributions are discrete, one can regard them as vectors, and measure the difference between the quantum and classical probability vectors by the 1-norm, defined as

$$|qm - cl|_1 = \sum_m |P_{cl}(m) - P_{qm}(m)| \tag{3.3}$$

Each probability distribution is normalized so that $\sum_m P(m) = 1$. Alternatively, one can define a probability density, which is normalized so that $\int \tilde{P}(\hbar m) d(\hbar m) = 1$. Then the 1-norm of the probability densities takes the form

$$|qm - cl|_1 = \int_{-\infty}^{\infty} |\tilde{P}_{cl}(\hbar m) - \tilde{P}_{qm}(\hbar m)| d(\hbar m) \tag{3.4}$$

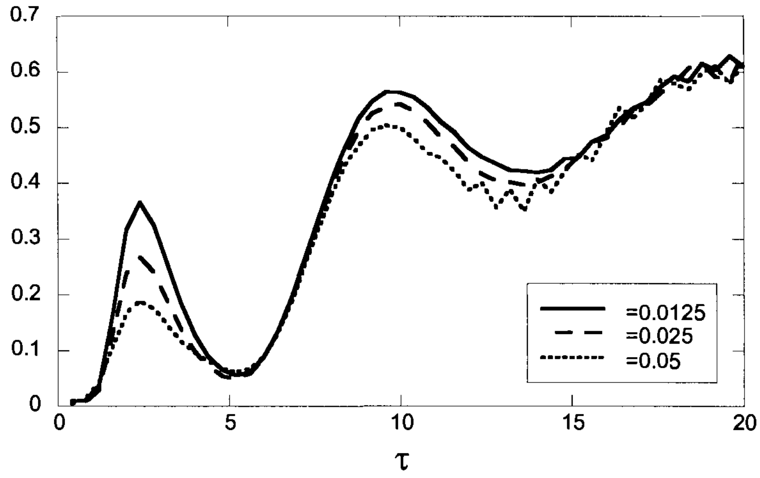

Figure 3.6: Scaling of $|qm - cl|_1$ [Eq. (3.3)] with time and β for the nonchaotic state ($e = 0$, $\alpha = 0.5$). Each classical ensemble has 1,000,000 members.

These two forms are equivalent because $\tilde{P}(\hbar m) = P(\hbar m)/\hbar$, and the additional factor of $\hbar$ is cancelled by the factor of $\hbar$ in the integral.

The probability distributions can be seen in figure 3.5, where it is obvious that the quantum probability distribution is approximately the classical probability distribution with interference patterns superimposed upon it. As is typical for quantum interference patterns, their frequencies were found to scale linearly with β (as seen in Fig. 3.7. So in the classical limit these interference patterns will occur over a very fine scale.

Fig. 3.6 shows that the 1-norm of the QC differences in the probability distributions do not tend to zero as $\beta \to 0$. These two probability distributions do not approach each other in a pointwise sense, since it is impossible to choose a value of β that will make the differences in probability density at any given point arbitrarily small. This lack of pointwise convergence of the quantum probability distributions to the classical limit has also been observed for other systems, such as a particle in a box and the kicked rotor [5]. In these one-dimensional driven system, the quantum probability distributions develop a fractal-like structure, and only the smooth background converges to the classical probability distribution. We will show in section 5.3 that a similar result holds for Hyperion.

In summary, we found that for a regular state, the QC differences in the expecta-

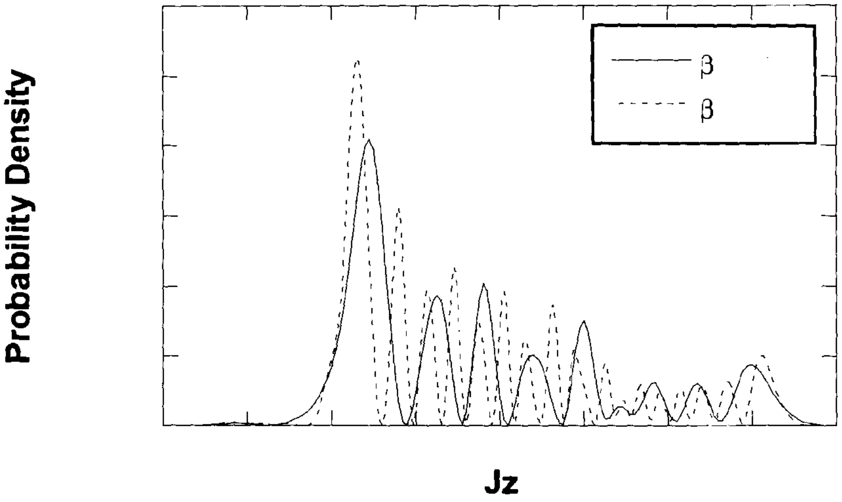

Figure 3.7: Quantum angular momentum probability densities for two different values of β. This shows that the width of quantum interference patterns is approximately linear β.

tion values were proportional to β^2. Since the value of β for Hyperion is on the order of 10^{-57}, these differences will be negligibly small for such a massive body. Although the differences in the expectation values will be small if Hyperion is prepared in a regular state, the probability distributions will not converge pointwise to the classical limit. From fig. 3.5, these differences should occur on a much finer scale than the classical structure. Hence the classical distribution is a coarse grained version of the quantum probability distribution.

Chapter 4

Results for a Chaotic State

In this section the rotation of a satellite is investigated for a chaotic initial state. The previous value of $\alpha = 0.5$ is used, but now the eccentricity is taken to be Hyperion's value of $e = 0.1$.

The results in this chapter should be contrasted to those of the previous section, where we found that the differences in $\langle J_z \rangle$ were proportional to β^2, and grew like a power law in time before eventually recurring. We also found that the probability distributions did not converge to the classical limit pointwise, but do so after smoothing the probability distribution over a width proportional to β. Here we will do similar analysis to see if the QC differences for chaotic states are as large as Zurek conjectures.

The initial state is centered at dimensionless angular momentum $J_0 = 10$, with a standard deviation of $\sigma = 0.5$, and a central angle $\phi_0 = 0$. This state is in the chaotic sea, far away from any regular torii, as can be seen in Figure 4.1. The maximum Lyapunov exponent for the chaotic sea is $\lambda = 0.85$.

4.1 Differences in $\langle J_z \rangle$

This state was evolved for several periods of the driving force, and the differences between the quantum and classical results were computed. In Fig. 4.2 the QC differences in $\langle J_z \rangle$ are initially dominated by statistical errors, which are approximately $\sigma_m = 2 \times 10^{-4}$. The QC differences in $\langle J_z \rangle$ grow exponentially with time until they saturate at $\tau \approx 6$. This saturation occurs when the classical trajectories ergodically fill the chaotic sea. For $\tau > 20$ the classical ensemble saturates at $\langle J_z \rangle \approx 8.2$. The quantum value of $\langle J_z \rangle$ also saturates at approximately the same value, but with ir-

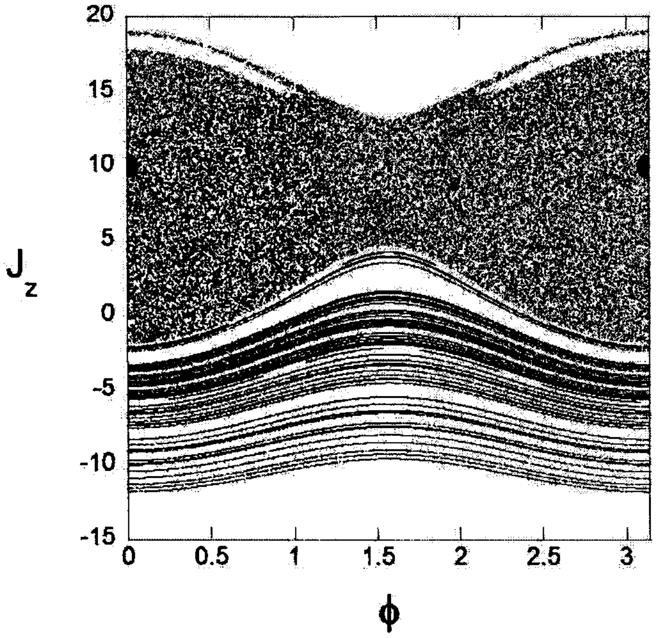

Figure 4.1: Poincare Section for a chaotic state, $\alpha = 0.5$, $e = 0.1$. The black circle denotes a typical initial state, with $J_z = 10$ and $\delta = 0.5$

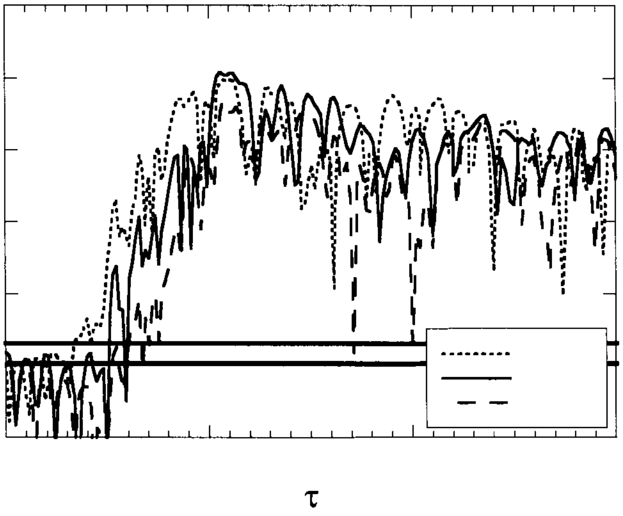

Figure 4.2: QC differences in $\langle J_z \rangle$ vs τ for a chaotic state, $\alpha = 0.5, e = 0.1$. For $\beta = \{1 \times 10^{-3}, 3 \times 10^{-3}, 8 \times 10^{-3}\}$ the statistical errors are $\sigma_m = \{1.4 \times 10^{-4}, 1.4 \times 10^{-4}, 2.2 \times 10^{-4}\}$. The black lines show the values of these statistical errors.

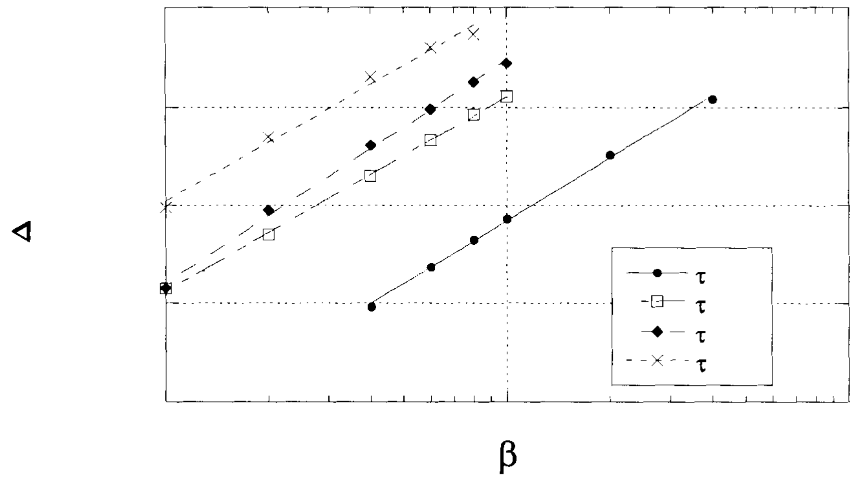

Figure 4.3: QC differences in $\langle J_z \rangle$ vs β, for a chaotic state before saturation is reached, showing a β^2 dependence.

regular fluctuations superimposed. This suggests that the QC differences here are dominated by quantum fluctuations once the probability distributions have saturated the chaotic sea.

This behavior has been noted in other chaotic systems, including two coupled spins [18] and for two coupled rotors [7]. So the cessation of exponential growth of the QC differences is not unique to this model of Hyperion.

4.1.1 QC Differences in $\langle J_z \rangle$ for Early Times

To determine how the QC differences in average momentum scale with β, we varied β with τ fixed at the times of the peaks in Fig. 4.2. As a notational convenience, we will label these QC differences by $\Delta\langle J_z \rangle$. From Fig. 4.3 it can be seen that the QC differences in $\langle J_z \rangle$ scale as β^2; the same scaling as was found for the non-chaotic states. This β^2 scaling agrees with the results predicted in [8]. The classical ensemble sizes were chosen so that $\sigma_m = \{1.6 \times 10^{-4}, 1.6 \times 10^{-4}, 2.2 \times 10^{-4}\}$ for $\beta = \{1 \times 10^{-3}, 3 \times 10^{-3}, 8 \times 10^{-3}\}$.

In the initial growth region of Fig. 4.2,the QC differences in $\langle J_z \rangle$ vary with time as

$$|\langle J_z \rangle_Q - \langle J_z \rangle_C| \propto e^{2.9\tau} \tag{4.1}$$

for $\tau = 2 \cdots 5.5$. The exponent in Eq. (4.1) appears to be independent of the value of β. The exponent is greater than 2λ, implying that the QC differences grow at a rate that is greater than the classical Lyapunov exponent. Because the growth occurs over a short interval in time, the differences might grow as a powerlaw with a large exponent rather than exponentially. However the exponential growth assumption agrees with the results of [8, 6], so it is more reasonable to assert that the differences grow exponentially in time rather than as a power law.

The exponential growth eventually saturates at $\tau \approx 6$. This cessation of exponential growth of the QC differences in $\langle J_z \rangle$ is relevant to Zurek's argument [46] that, absent decoherence, the QC differences for Hyperion should reach macroscopic size within about 20 years. That argument implicitly assumes that the QC differences will continue to grow exponentially forever. However, we will find below that this is not the case.

4.1.2 QC Differences in $\langle J_z \rangle$ for the Saturation Regime

The maximum QC differences occurs in the saturation regime. If these differences converge to 0 as $\beta \to 0$ then the classical limit will be reached for all times, and there will be no *break time* beyond which QC correspondence fails.

At the beginning of the saturation region (Fig. 4.2), $\Delta\langle J_z \rangle$ reaches a maximum, before decaying to a saturation level, about which it fluctuates irregularly. Because of this fluctuation in the saturation regime, we calculate the time average of the QC differences. Here $\Delta\langle J_z \rangle$ was averaged over the interval $\tau = 20 \cdots 100$. In Figure 4.5, these averaged QC differences tend to scale as $\beta^{2/3}$.

The peak QC differences also show a similar scaling with β (see Fig. 4.4), for sufficiently small β:

$$\max \Delta\langle J_z \rangle \propto \beta^{2/3} \tag{4.2}$$

This scaling also was found for the maximum QC differences in a model of coupled pendulums [7], so it might be generic for chaotic systems in the saturation regime.

4.2 QC Differences in Probability Distributions

The convergence of the quantum expectation values to the classical result is needed for the classical limit to be reached. However convergence of these values is not a sufficient

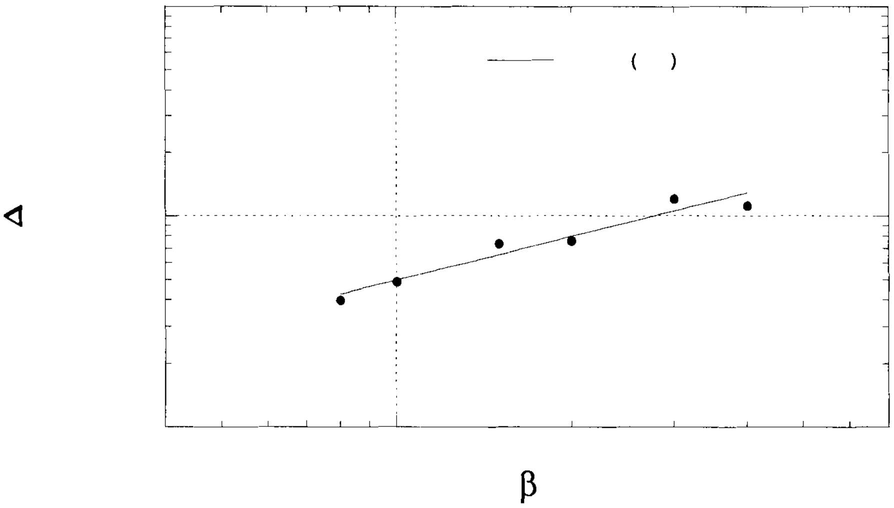

Figure 4.4: Maximum QC differences in $\langle J_z \rangle$ versus β for a chaotic state. $e = 0.1$, $\alpha = 0.5$. This suggests that the maximum $\Delta\langle J_z \rangle$ scales as $\beta^{2/3 \pm 0.03}$.

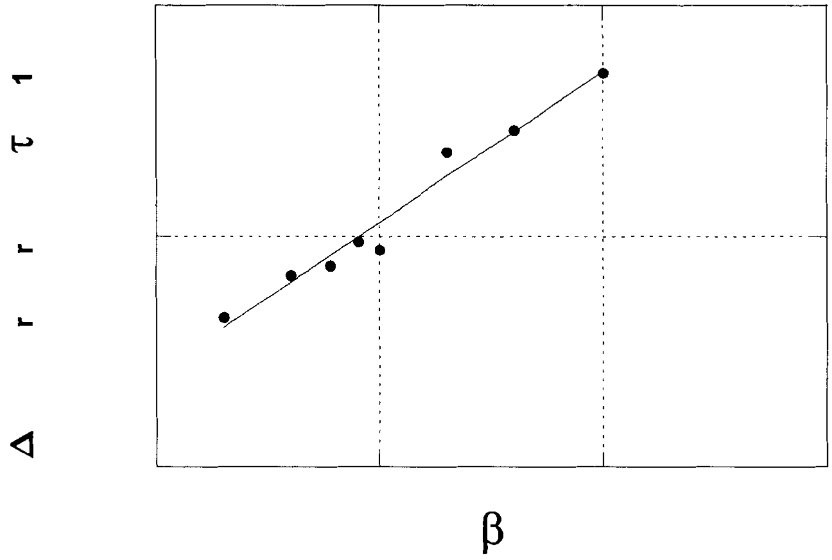

Figure 4.5: QC differences in $\langle J_z \rangle$, averaged over τ from 20 to 100. Initial state is in the chaotic sea. $e = 0.1$, $\alpha = 0.5$. This suggests that $\Delta\langle J_z \rangle \propto \beta^{2/3 \pm 0.01}$ in the saturation regime.

condition for the classical limit to be reached. It is possible for two probability distributions to have the same expectation value, while having inequivalent variances and higher moments. The entire moment hierarchy is composed within the probability distributions, so the convergence of the probability distributions to the classical limit is a stronger condition than the convergence of expectation value.

Zurek suggested that the QC differences in the probability distributions will be much larger for chaotic systems than for their non-chaotic brethren. We found in Chapter 3, that the probability distributions in the absence of chaos did not reach the classical limit. So we will investigate the differences in the same manner to determine if the chaotic probability distribution converges to the classical limit, and if there is a qualitative difference between the two results.

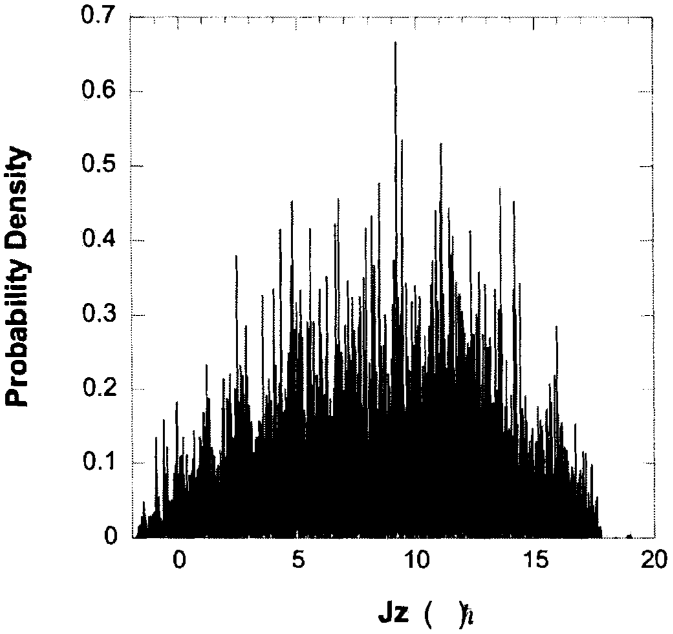

Figure 4.6: Quantum probability density for $\tau = 40.0$, $\beta = 0.002$

The probability distributions contain much more information than do the averages of observables. These probability distributions are shown in Figures 4.6 and 4.7. From these figures we see that at the finest possible scale the quantum probability distribution bears little resemblance to the classical probability distribution, however the quantum distribution appears to be much more classical when viewed on a coarser scale.

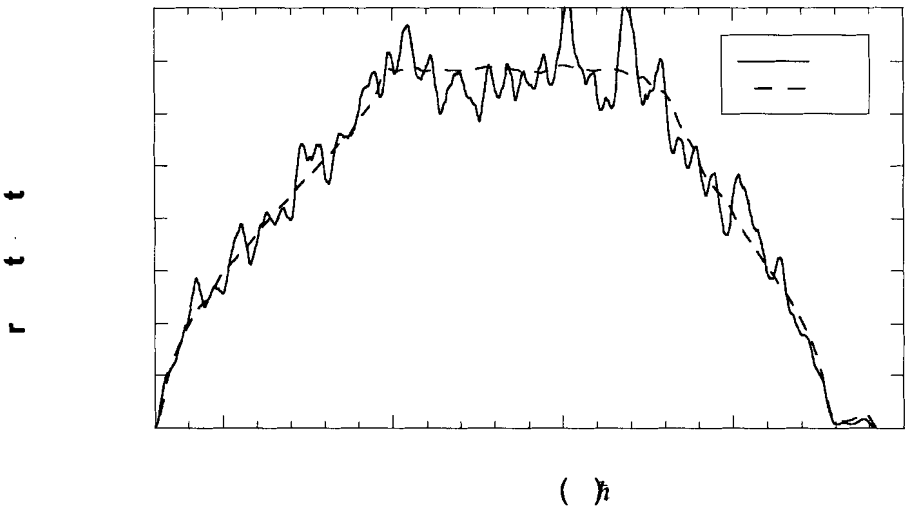

Figure 4.7: Quantum and classical probability densities for $\tau = 40.0$, $\beta = 0.002$. Both quantum and classical densities are convolved with a triangular filter of width 0.25 in J_z

We use the quantity $|qm - cl|_1$ (defined in Eq. (3.3)) as a measure of the QC differences in the probabilities. As can be seen from Fig. 4.8, $|qm - cl|_1$ increases with time before saturating, and fails to converge to 0 as $\beta \rightarrow 0$. Since pointwise convergence does not occur, neither for the chaotic nor for the non-chaotic states, this lack of pointwise convergence is not a result of chaos, but is more generic.

Most of the QC differences in the probabilities occur on a very fine scale, and a modest amount of smoothing is sufficient to cause the quantum probability distributions to better approximate the classical results. Fig. 4.7 shows that the differences between the two distributions are dramatically reduced by smoothing them over a small width. This smoothing process is discussed and compared to environmental interactions in greater detail in section 5.3.

To summarize the results of this section, for early times the QC differences in $\langle J_z \rangle$ scale as β^2, and increase exponentially with time. The exponential growth ceases when the probability distributions saturate the chaotic sea. Both the maximum values and the saturation levels of the QC differences were found to scale as $\beta^{2/3}$. A small amount of smoothing can dramatically reduce the QC differences in the probability distributions, since most of the differences come from very fine scale structures in the

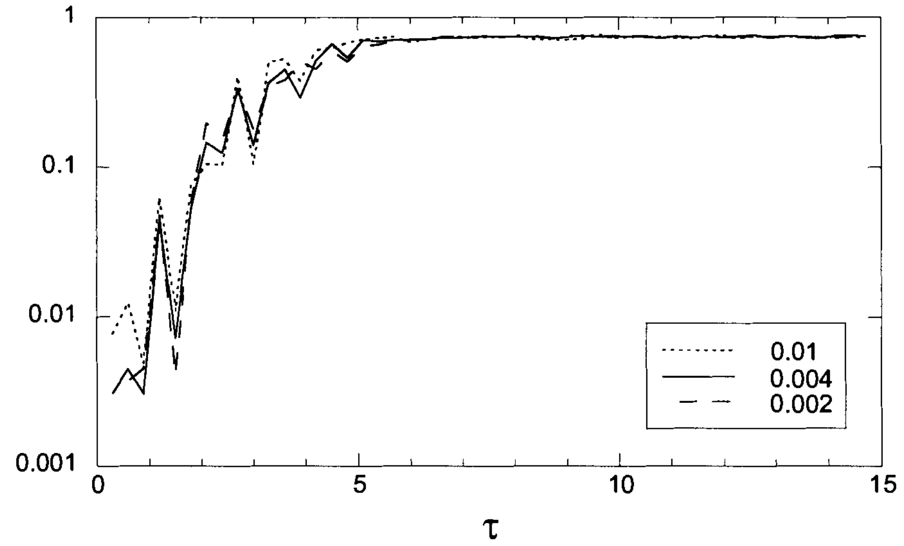

Figure 4.8: $|qm - cl|_1$ vs time for different values of β, for a chaotic state, $e = 0.1$

quantum probability distributions.

4.3 Fractal Probability Distributions

In classical mechanics the smooth initial state becomes more and more complex as time proceeds, as the distribution folds its self in phase space. At any finite time the probability distribution will be smooth except at a finite number of points which are associated with foldings. However in quantum mechanics, large oscillations may occur on a fine scale. These fine-scale oscillations increase in frequency as $\beta \longrightarrow 0$, and may lead to a fractal probability distribution in this limit [5] even at finite times.

A fractal curve is characterized by having a non-integer capacity dimension, which is a measure of the number of elements required to form a finite cover of the set in the limit as the size of the elements goes to zero [28]. This dimension is formally defined for a set as,

$$d_c = -\lim_{\epsilon \to 0} \left(\frac{\ln N(\epsilon)}{\ln \epsilon} \right) \tag{4.3}$$

where $N(\epsilon)$ is the minimum number of sets of size ϵ needed to cover the set whose dimension we want to find. The parameter ϵ is a measure of the resolution on which

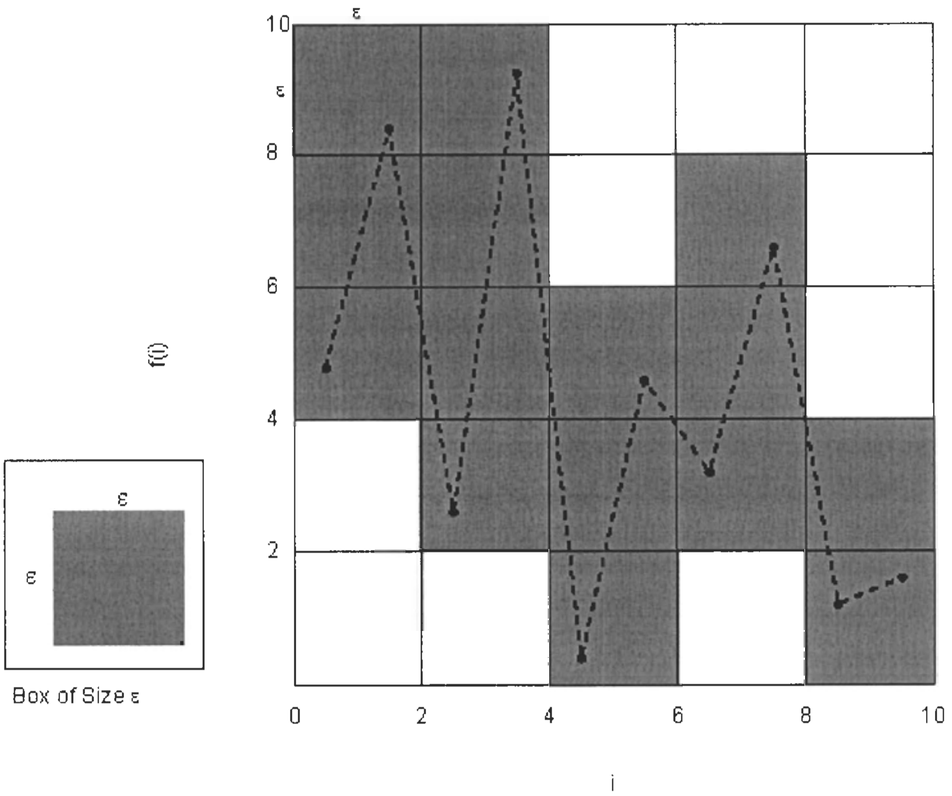

Figure 4.9: Diagram of boxes of size $r = 2$ forming a finite cover of a graph.

we are viewing the set. Any feature that has an area smaller than ϵ^2 will not be resolved until we examine a curve at a finer resolution.

The quantum angular momentum distribution $P(m)$ takes on only integer values of m. We can construct a lower resolution version of the sequence $P(m)$ by using the subsequence $P(ir)$, where i is an integer and r is the resolution of the distribution. Here r plays the role of ϵ in the definition of the capacity dimension given above. So to estimate the capacity dimension, we need to count the number of boxes of side length r needed to cover the probability distribution as $r \to 0$. This process is shown in Figure 4.9.

To estimate the number of boxes needed to cover the graph, we must first estimate the area that needs to be covered and then divide it by the area of the elements in the set. The area needed to cover the adjacent points $P(ir)$ and $P(ir+r)$ is approximately $|P(ir + r) - P(ir)|r$. So the area needed to cover the whole graph is approximately $r \sum_i |P(ir + r) - P(ir)|$. Hence the number of sets needed is approximately this area divided by r^2, which is the area of a box. Hence $N(r)$ is approximately

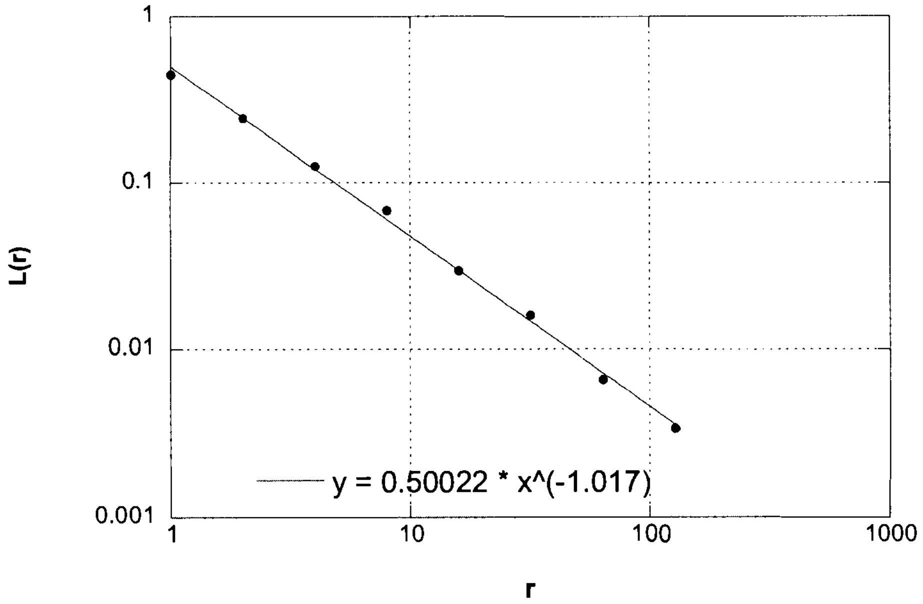

Figure 4.10: Log Log plot of Vertical length of quantum probability distribution versus resolution for $\beta = 0.002$, and $\tau = 10.5$

$$N(r) \approx \frac{\sum_i |P(ir+r) - P(ir)|}{r} \tag{4.4}$$

Using this approximation the capacity dimension is approximately

$$d_c = 1 - \lim_{r \to 0} \left(\frac{\ln L(r)}{\ln r} \right) \tag{4.5}$$

Where $L(r)$ is defined to be $\sum_i |P(ir+r) - P(ir)|$. Hence the capacity dimension can be estimated from the slope of $L(r)$ vs r on a log-log plot as $r \to 0$. This allows us a convenient way to estimate the capacity dimension for a quantum angular momentum distribution.

Fig. 4.10 shows that the slope is -1 when the curve reaches maximum complexity at $\tau = 10.5$, implying that the capacity dimension for the curve is 2. From Fig. 4.8, the probability distribution reaches its maximum complexity at $\tau \approx 5$. Hence the probability distribution should have fractal characteristics for all $\tau > 5$. Thus the limit of the quantum probability distribution is a space-filling curve. For a non-chaotic initial state, the quantum probability distribution exhibited no such fractal behavior. However it is possible that insufficient time was given for non-chaotic initial state to reach its maximum complexity.

The fractal behavior of the quantum distribution does not arise from the fact that the even parity states do not interact with the odd ones (as noted in section 2.2), which is an artifact of the model. If every even numbered element in the distribution was correlated to the nearest even numbers, then the value of the vertical distance between points should vary far more significantly from r=1 to r=2 than from r=2 to r=4. Since this does not occur in Figure 4.10, one is left with the conclusion that the fractal behavior does not arise from the even-even, odd-odd coupling induced in this model.

The most important result that follows from the fractal like behavior in the saturation regime, is that smoothing will be especially effective at reducing $|qm - cl|_1$ since the majority of the QC differences will occur on a very fine scale. Hence environmental effects on the satellite may be sufficient to cause the probability distributions to approach the classical limit in a pointwise sense.

Chapter 5

Environmental effects on Hyperion

Interaction with the environment leads to decoherence and dissipation. Decoherence is a quantum effect which causes interference patterns to decay. The time scale upon which this happens is model dependent, and for some systems there is no single decoherence timescale [2]. Strunz et al. [40] suggest that for the rapid decoherence expected in macroscopic bodies, the decay time varies as a small power of $\hbar$, and is not sensitive to the system Hamiltonian.

Dissipation is a classical effect which results in diffusive spreading of the probability distributions. Often, the timescale for dissipation is much longer than the timescale for decoherence, and dissipation is insensitive to $\hbar$, unlike decoherence. But both effects are present together, and it is not always easy to separate them.

The effect of the environment on a quantum system is often treated by a master equation that has non-unitary time evolution. Because an initially pure state can evolve into a mixed state, it is necessary to compute the density matrix, which requires much greater storage than does the computation of a state vector. The requirements for storage and computation time scale like K^2, where K is the number of basis vectors needed to store a state vector.

An alternative method is to perform n evolutions of the Schrödinger equation, Eq. (2.15), with a different realization of a random potential added for each run. Averaging the probability distributions that result from the each of the n runs is physically equivalent to tracing over the environmental variables. The advantage of this method is that the computational resources for each run scale as K, rather than K^2 for the master equation. On the other hand, to achieve good accuracy, a large number of realizations of the random potential must be considered, in order to reduce

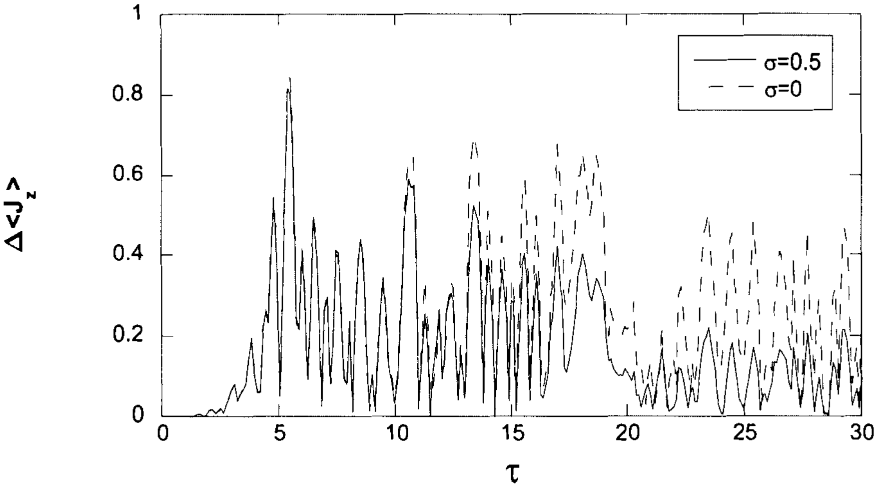

Figure 5.1: Variation of $\langle J_z \rangle$ with τ with and without the random potential with $\sigma/V_{ch} = 0.024$, $\tau_c = 0.01$. (chaotic state, $\beta = 0.05$)

the statistical errors in the quantum calculation. However the number of realizations of the random potential that was needed to get sufficient accuracy was considerably less than K, so this method was much more computationally efficient than integrating the master equation.

A stochastic potential is used, in both the quantum and classical mechanics, to model the effect of the environment on the rotor. The simplest stochastic potential that yields a random torque is,

$$H_{int} = \sigma R(t) \cos(\phi) \tag{5.1}$$

Here $R(t)$ is a correlated random function of zero mean and unit variance, V_0 is the amplitude of the random potential, and τ_c is its correlation time. A correlated random function is used because the fluctuations in the environment do not occur instantly, but rather they occur and decay on some time scale τ_c. The correlated random sequence $R(t)$ can be constructed from an uncorrelated sequence, as is shown in Appendix A. The results are not sensitive to the exact form of Eq. (5.1), and qualitatively similar results were obtained when $\cos(\phi)$ was replaced by $\cos(2\phi)$. As is shown in Appendices B and C, the effects of the environment are expected to depend mainly on the product $\sigma^2\tau_c$, rather than on the two parameters separately. Therefore we label the results by the momentum diffusion parameter, $D = \sigma^2\tau_c/6$, which is

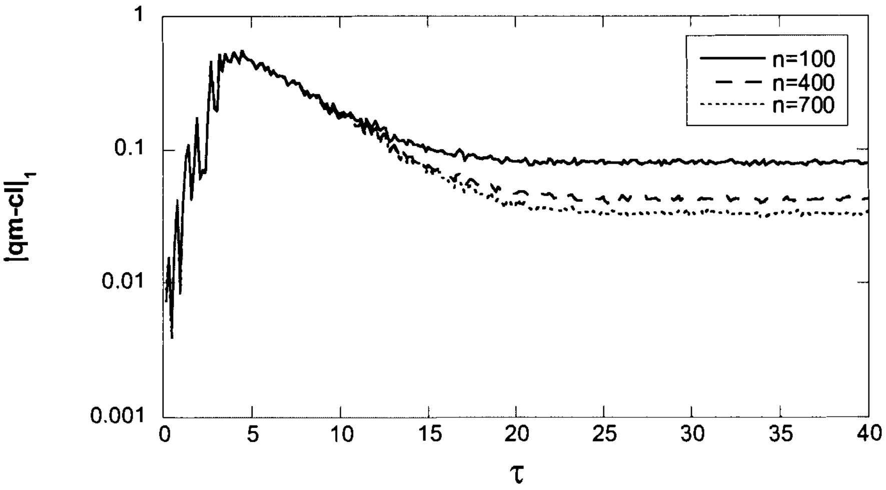

Figure 5.2: Variation of $|qm - cl|_1$ with τ for different numbers n of realizations of the random potential with $\sigma/V_{ch} = 0.012$, $\tau_c = 0.01$. (chaotic state)

derived in Appendix E.

The environmental perturbation should be much weaker than the tidal force on the satellite. Hence we compare the interaction potential Eq. (5.1) to the amplitude of the tidal potential, made dimensionless by dividing by I_3/T^2, which is approximately $V_{ch} = 3\sqrt{2}\pi^2\alpha$, or $V_{ch} \approx 21$ for $\alpha = 0.5$. In all cases reported in this thesis, the environmental perturbation was so weak as to have no significant effect on the classical results, so its only significant effect is to produce decoherence in the quantum results. The same parameters as in the previous chaotic case were used, $\alpha = 0.5$ and $e = 0.1$.

Many realizations of the random potential were computed, and the results averaged, to get an accurate measure of the effects of the environment. We used 500 realizations to obtain results that are not strongly affected by statistical errors. Fig. 5.1 shows the QC differences in $\langle J_z \rangle$, with and without the random environmental potential. The environment has no significant effect at early times, but in the saturation regime the QC differences are reduced. Since the primary effect of environmental decoherence is to destroy fine-scale structures in the probability distributions, which do not affect averages like $\langle J_z \rangle$, this result may seem surprising.

In fact, a typical trace of $\langle J_z \rangle$ versus time for a single realization of the random potential will look very much like that from a run without the random potential (Fig. 5.1). But as time progresses, the oscillations in $\langle J_z \rangle$ for different realizations

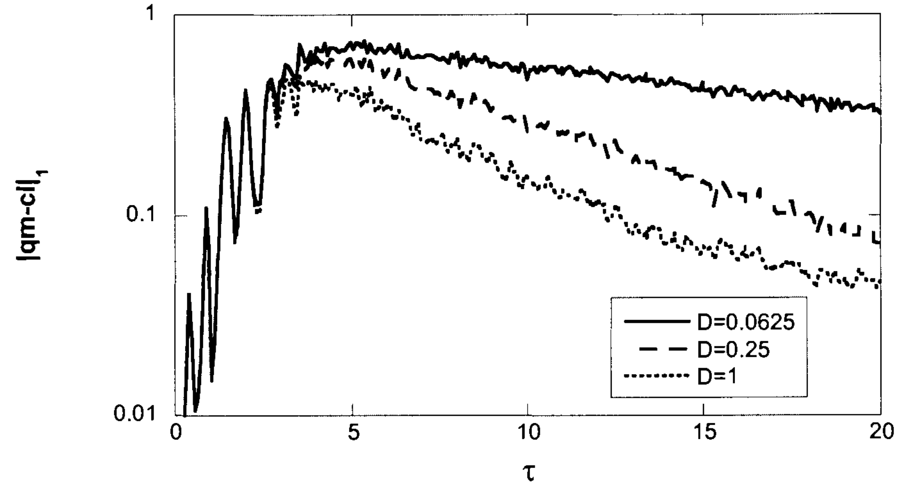

Figure 5.3: $|qm - cl|_1$ vs τ for $\beta = 0.05$, for varying $D = \sigma^2\tau_c/6$.

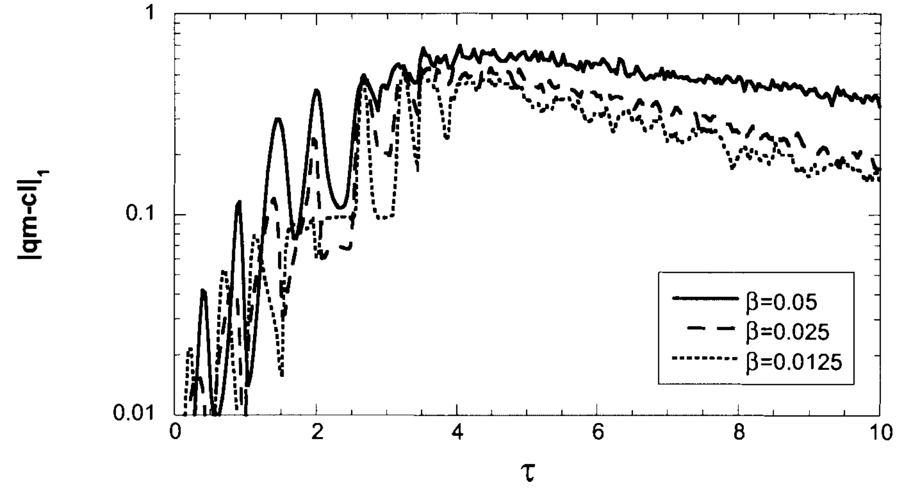

Figure 5.4: $|qm - cl|_1$ vs τ for varying β, with $\tau_c = 0.01$ and $\sigma/V_{ch} = 0.012$, for a chaotic state.

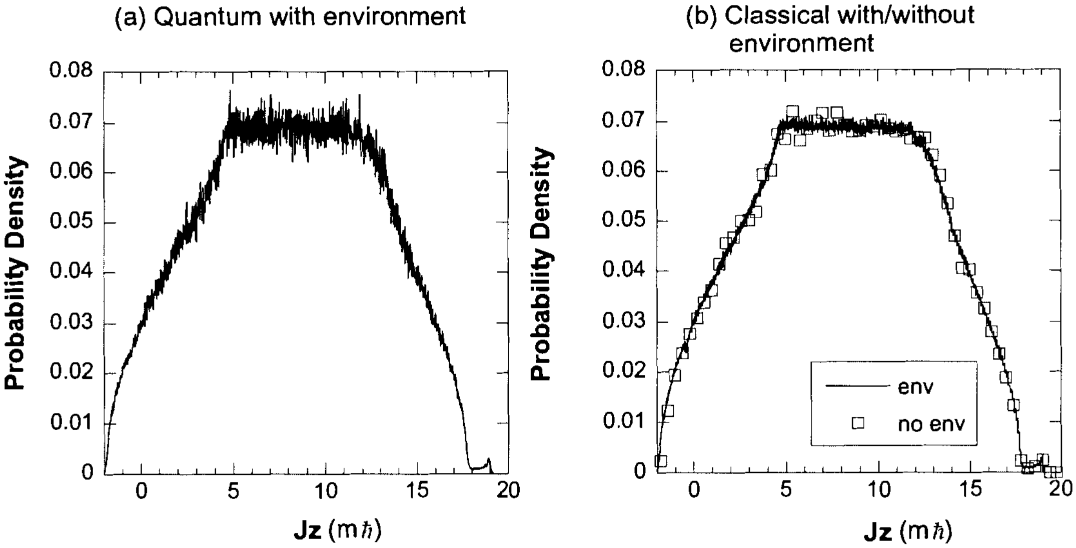

Figure 5.5: Quantum and Classical probability distributions at $\tau = 40$, with $\beta = 0.0125$, $\sigma/V_{ch} = 0.012$, and $\tau_c = 0.01$ for the chaotic state. In (b) the solid lines denote the results with the environment, and squares without the environment, showing that the classical probability distribution is not significantly affected by environmental effects.

of the random potential tend to get out of phase with each other, and the decreased amplitudes of the QC differences in Fig. 5.1 are due to the averaging over the many different realizations of the random potential.

In Fig. 5.2, 100 realizations of the interaction potential were sufficient to find the maximum QC differences in $|qm - cl|_1$. However, 700 realizations of the interaction potential were insufficient to resolve the QC differences in $|qm - cl|_1$ (Eq. (3.3)) in the saturation regime, and so for computational reasons, these will be estimated rather than directly computed. The variation of these differences with β and the environmental parameters can be seen in Figs. 5.3 and 5.4.

These figures show that for early times, decoherence does not substantially reduce the QC differences. When we vary D with β fixed, the QC differences are initially insensitive to decoherence. In the saturation regime decoherence becomes much more powerful, and these differences tend to decay exponentially. A similar result is seen for reducing β with D held fixed.

It can be seen in Fig. 5.5 that, with the inclusion of the environmental perturba-

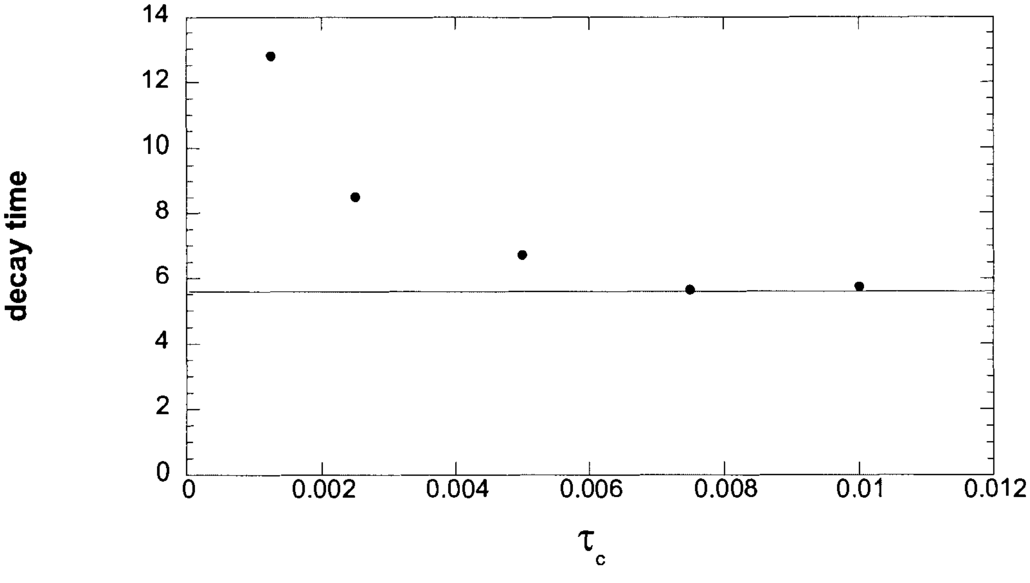

Figure 5.6: Decay times τ_d of $|qm - cl|_1$ vs the correlation time τ_c of the perturbing environment, with $\beta = 0.05$, $\sigma/V_{ch} = 0.012$ in the saturation regime ($\alpha = 0.5$, $e = 0.1$). The line shows the classical decay time for two different probability distributions.

tion, the quantum probability distribution is much closer to the classical distribution than without the environment (compare Fig. 4.6). This agrees with our intuition that environmental interactions will smooth out the finescale quantum interference patterns that appear in the saturation regime.

5.1 Environmental Effects in the Saturation Regime

In the saturation regime, the QC differences in $|qm-cl|_1$ (Eq. (3.3)) appear to decay exponentially from their maximum value to a saturation level (see Fig. 5.3 and 5.4). The rate of this decay is a diffusion time, and is not the decoherence time, as will be shown shortly. From Fig. 5.6 it is clear that, for sufficiently large values of τ_c, the decay time τ_d no longer depends on τ_c, but settles at $\tau_d \approx 5.6$. For sufficiently large σ and sufficiently small β, the decay time was found to also have approximately this same limit.

To test whether this decay rate is governed by quantum mechanics, we compared two classical ensembles with different initial values of J_0, $J_0 = 10$ and $J_0 = 11$, and

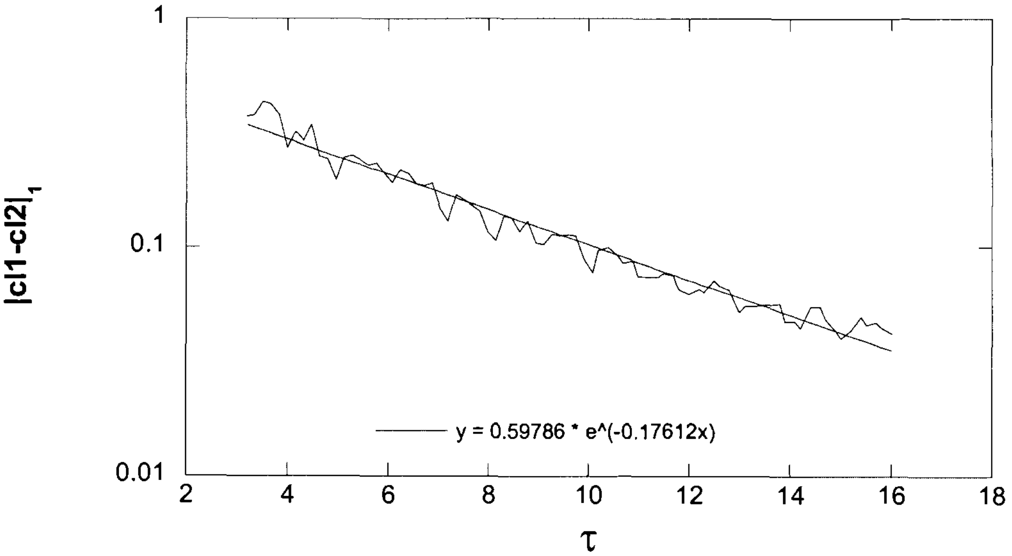

Figure 5.7: 1 norm of the difference between two classical ensembles, one with $\langle J_z \rangle = 10$, the other $\langle J_z \rangle = 11$. $\beta = 0.05$, $\sigma/V_{ch} = 0.012$, $\tau_c = 0.01$

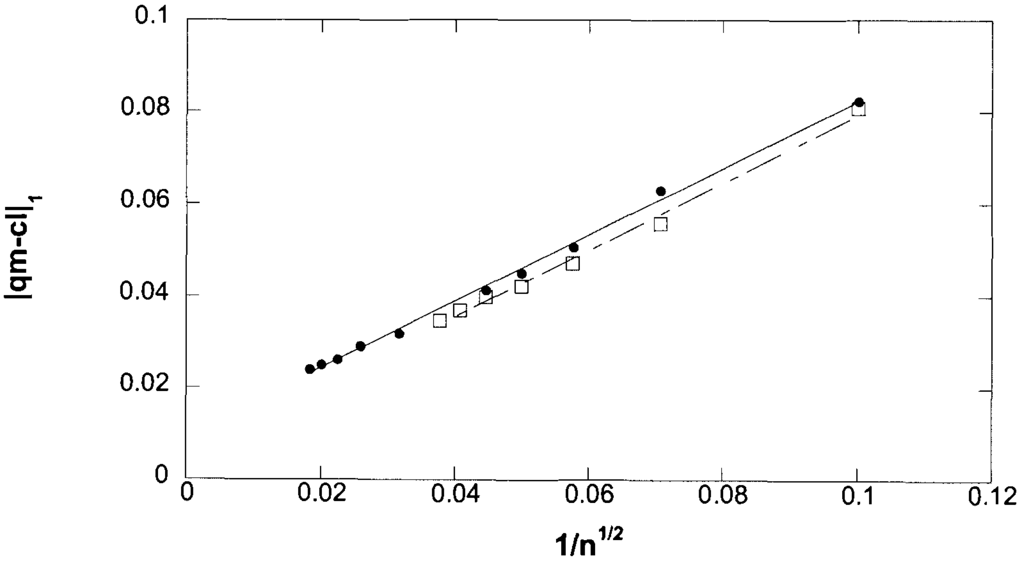

Figure 5.8: $|qm - cl|_1$ vs $n^{-1/2}$ at $\tau = 40$. n is the number of realizations of the random potential. ($\sigma/V_{ch} = 0.012$, $\tau_c = 0.01$ for the chaotic state). The statistical errors in the ensemble, unlike the statistical errors from the noise, do not diminish as $n \to \infty$. This causes a non-zero intercept for both these graphs.

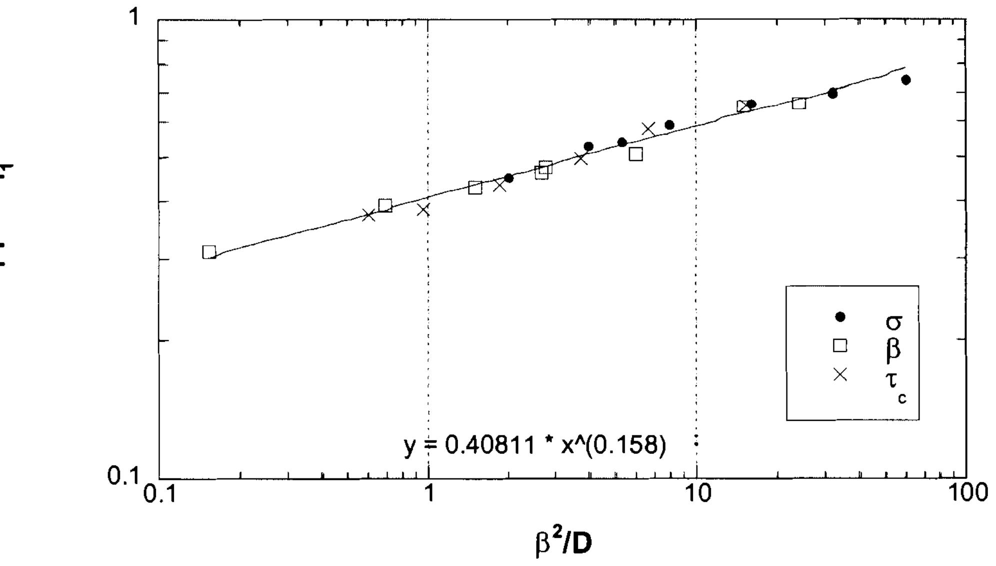

Figure 5.9: Maximum values of $|qm - cl|_1$ vs β^2/D. The points labeled β, σ, and τ_c represent data sets where β, σ, and τ_c were varied with the other two parameters held constant. This plot shows that $|qm - cl|_1 \propto (\beta^2/D)^{\frac{1}{6}\pm 0.01}$.

computed the 1-norm of the difference between them as a function of time. Fig. 5.7 shows that these initially different classical ensembles converge at a rate given by $\tau_d = 5.6$. So, apparently, this time scale measures how quickly the differences between two different distributions decrease as they both grow to fill the chaotic sea.

It is not clear from Fig. 5.3 and 5.4 whether the QC differences in the probability distributions eventually decrease to zero or reach a non-zero long-time limit. In Fig. 5.8 the long-time saturation level of $|qm - cl|_1$ is plotted as a function of the number n of realizations of the random potential. In the limit $n \to \infty$ the QC differences approach a small value that appears to be slightly positive. However that extrapolated limit is substantially smaller than the typical statistical errors for ensemble sizes of 10^6 to 2×10^6, and so is not significantly different from zero.

5.2 Scaling of the Maximum QC Differences

The maximum value of $|qm - cl|_1$ for the quantum and classical probability distributions must depend on the three parameters β, σ, and τ_c. However, in agreement with arguments presented by Pattanayak et al. [36], the data was found to collapse onto a single curve parameterized by $\xi = \beta^2/D$ (Fig. 5.9). From a least squares fit of $|qm - cl|_1$ vs ξ, the scaling relationship was found to be

$$\max(|qm - cl|_1) \propto \left(\frac{\beta^2}{D}\right)^{\frac{1}{6}\pm 0.01} \tag{5.2}$$

This scaling as $\hbar^{1/3}$ was also found for a coupled rotor model without decoherence [7]. This result suggests that the $\beta^{1/3}$ scaling found here might be generic for systems with more than one degree of freedom, and also suggests that the pointwise convergence of the quantum probability distribution to the classical distribution may occur because of other interacting degrees of freedom (not necessarily an external environment).

5.3 Effects of Decoherence vs Smoothing

In the previous section we showed that although the expectation values converged to the classical result as $\beta \to 0$, the probability distributions did not. Decoherence was found to cause the probability distributions to approach the classical result as predicted by Zurek. However if decoherence is *necessary* to understand the classical limit, then no other physically motivated process should be able to coax the classical probability distributions out of the quantum results.

Here we will show that the coarse graining or smoothing of these distributions will make them appear classical. This process is physically justified since for macroscopic systems, measuring their angular momentum to a resolution of $\hbar$ is well beyond the means of any measuring apparatus. If we assume that a measuring apparatus can only measure angular momentum to a resolution of Δ_s, then the observed probability distributions will be the quantum distributions smoothed over a range Δ_s in angular momentum.

Consider the smoothed probability distribution $P_s(q)$ which is found by the following convolution

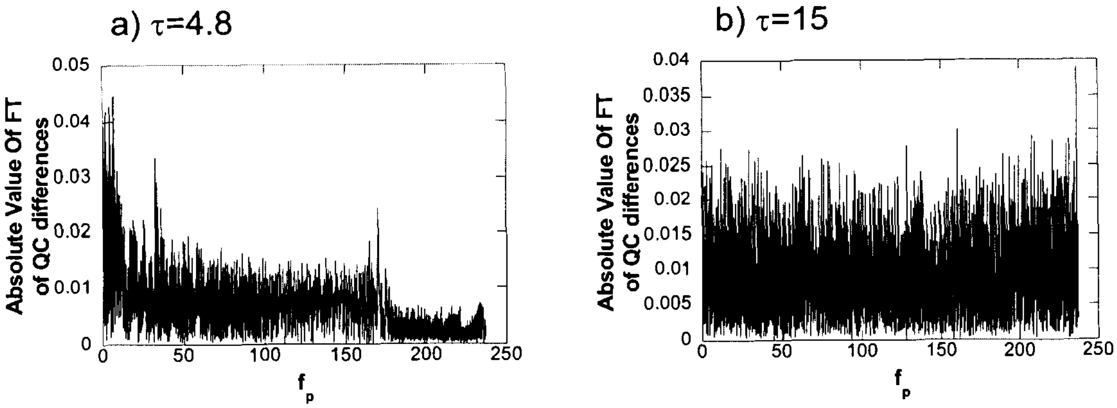

Figure 5.10: Amplitude of Fourier transform of the QC differences in probability distributions for chaotic state with $\beta = 0.002$, f_p represents the scale of QC differences in the probability distributions and is units of $1/J_z$

$$P_s(q) = \int_{-\infty}^{\infty} P(q')F(q-q')dq' \tag{5.3}$$

Here $F(q)$ is a filter function that represents the imperfect detection of an aparatus. The effects of smoothing are more transparent in Fourier space than in momentum space, and using the convolution theorem the smoothed probability distribution is

$$P_s(f_p) = P(f_p)F(f_p) \tag{5.4}$$

Where $P(f_p)$, and $F(f_p)$ are the Fourier transforms of the momentum probability distributions and the filter function respectively. A high f_p represents differences that occur over a very fine scale in momentum.

The effect that smoothing has on the differences in the probability distributions can also be easily understood using the convolution theorem. Since the Fourier transform is a linear operation, the Fourier transform of the smoothed QC differences will just be the Fourier transform of these differences multiplied by the Fourier transform of the filter function. This allows us to gain a much better understanding of what the filter does to the spectral components of the differences than we could get from just looking at them in momentum space.

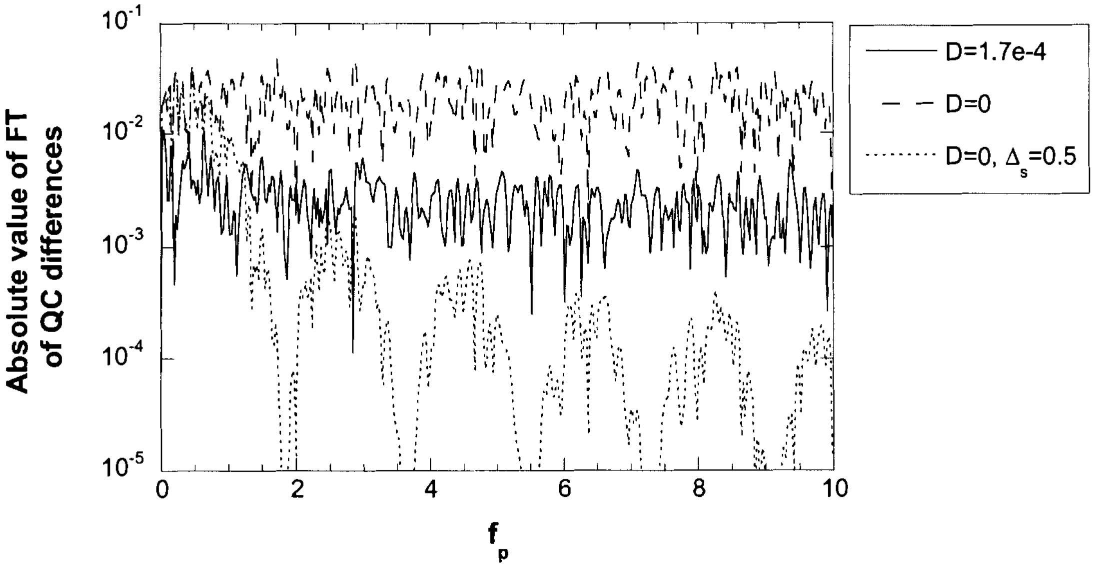

Figure 5.11: Spectrum of QC differences for $\beta = 0.05$ for cases without smoothing or decoherence, and smoothing or decoherence alone. f_p is the scale in momentum of QC differences and is proportional to $1/J_z$.

5.3.1 Smoothed Results for Hyperion

Here we will examine the effects of smoothing the quantum and classical probability distributions so that the effects of smoothing may be compared to decoherence. As mentioned earlier, the effectiveness of smoothing varies depending on the scale of the QC differences. So to see if smoothing will be effective in inducing classicality, we must examine how the spectral components of the QC differences vary with time.

From Fig. 5.10, the scale of oscillations in the momentum probability distribution varies with time. When the differences in $\langle J_z \rangle$ are largest, the differences in the probability distributions occur mostly at low f_p. However in the saturation regime they are roughly evenly spread throughout the spectrum. Since the differences in the momentum probability distributions occur on a finer scale at $\tau = 15$ than at $\tau = 4.8$, smoothing will be much more effective at late times than for earlier times.

As seen in Fig. 5.11, convoluting the probability distributions with a triangular filter of half width $\Delta_s = 0.5$ dramatically reduces the high frequency QC differences between them, but it does not substantially reduce differences which occur on a scale in momentum that is wider than the filter. Decoherence on the other hand reduces

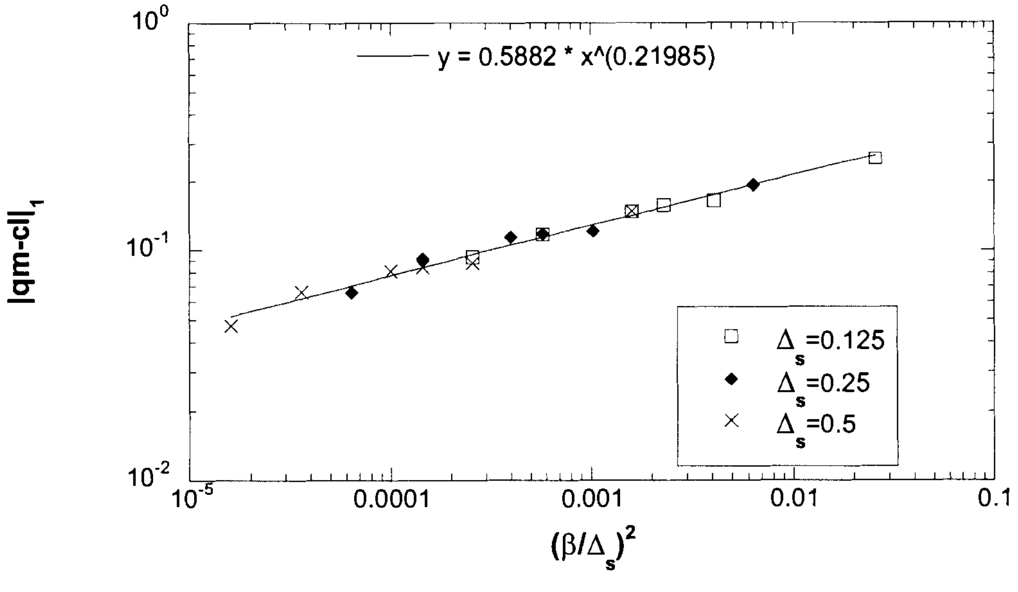

Figure 5.12: $|qm-cl|_1$ versus $(\beta/\Delta_s)^2$ for different values of Δ_s and β. The differences in the probability distribution are found to obey $|qm - cl|_1 \propto (\beta/\Delta_s)^{0.44\pm0.02}$

differences that occur at any scale in momentum.

If we focus on the saturation regime, then we find that $|qm-cl|_1$ obeys a powerlaw in (β/Δ_s) when smoothing is considered. This shows that smoothing can also dramatically reduce the differences in the saturation regime, and shows that the probability distributions in the saturation regime approach the classical limit as $\beta \rightarrow 0$ with Δ_s fixed.

However at any time a filter can be constructed to make the QC differences similar to those of decoherence. In Fig 5.5, they were made very small by an amount of thermal noise that was too weak to diffuse the classical distribution. So if a small amount of decoherence can be simulated by applying an appropriate filter, then this filter also must have a negligible effect on the classical probability distribution.

This is impossible because of the properties of Fourier transforms. The width of the Fourier transform of a function obeys an uncertainty relation of the form $\Delta f(q)\Delta f(k) \geq 1$, where $f(k)$ is the Fourier transform of $f(q)$. From this relation, to reduce QC differences with frequencies less than 0.25 in Fig. 5.11 we must take Δ_s to be greater than 4. By comparing to Fig. 5.5 this smoothing scale is on the order of the width of the probability distribution. So it is impossible to construct a filter that

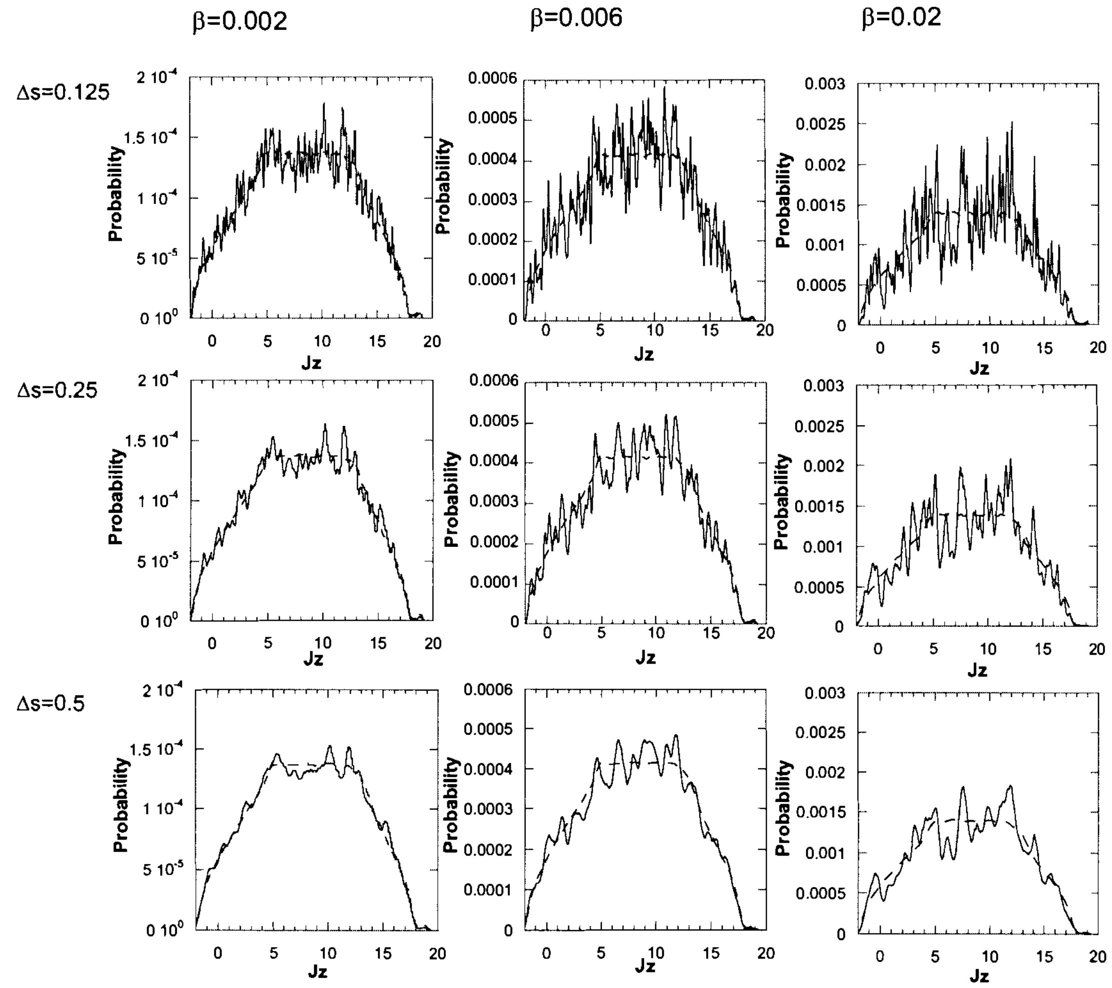

Figure 5.13: Smoothed quantum and classical probability distributions for different width smoothing filters for different values of β. The dashed line denotes the smoothed classical probability distribution, the solid line is the smoothed quantum distribution.

has the same effects as decoherence, since the corresponding filter will unrealistically spread the distribution.

Again this phenomenon is not unexpected since coarse graining is performed by convolution rather than averaging over a number of random evolutions. This causes decoherence to become stronger with time, whereas coarse graining does not, and so the two cannot be equivalent. This suggests that the two are different, but highly relevant factors in explaining the classical limit of quantum systems.

5.4 Summary

In summary, the environmental perturbations dramatically reduce the fine scale structure in the quantum distributions. The measure of the QC differences, $|qm - cl|_1$, was found to initially increase with τ in a form similar to the results in Sec. 4. After reaching a maximum value, $|qm - cl|_1$ then decreased exponentially with time. The decay time was found to be a classical diffusion time, and not a decoherence time. The maximum QC differences were found to scale as $(\beta^2/D)^{1/6}$, where D is the momentum diffusion parameter.

5.5 The Classical Limit of Hyperion

5.5.1 QC Differences Without Environment

Having calculated the QC differences for the chaotic rotation of a tidally driven satellite, and determined how they scale with the relevant parameters, we shall now use this information to estimate the magnitude of quantum effects on Hyperion. In particular, we shall assess Zurek's claim [47, 46] that environmental decoherence is needed to ensure its classical behavior. We first examine the magnitude of the QC differences for Hyperion if the effect of the environment is ignored.

First we must determine the dimensionless parameter $\beta = \frac{\hbar T}{I_3}$. Using Hyperion's mean density of $\rho = 1.4g$ cm^{-3}, and treating it as an ellipsoid with moments of inertia $I_3 > I_2 > I_1$, then $I_3 = 2.1 \times 10^{29}$ kg m^2. Using the value of $\hbar = 1.05 \times 10^{-34} Js$ and the orbital period $T = 1.8 \times 10^6 s$ then yields

$$\beta = 9.3 \times 10^{-58} \tag{5.5}$$

According to Eq. (4.2), the maximum QC differences in $\langle J_z \rangle$ are proportional to $\beta^{2/3}$. Hence the maximum QC difference in the dimensionless angular momentum, $\langle J_z \rangle$, for Hyperion should be approximately 5×10^{-37}. So there should be no observable difference between the quantum and classical averages of angular momentum for Hyperion.

This result contradicts Zurek's claim that, if decoherence is ignored, there should be a *break time* of no more than 20 years, beyond which the QC differences would become macroscopic. As was pointed out in section 1.2, if that break time is interpreted as the limit of the Ehrenfest regime, then it does not mark the end of the classical domain. But in [47] a *break time* of a similar order of magnitude was estimated for the end of the Liouville regime. Both of those estimates were based on an exponential growth of the QC differences that occur in a chaotic state. Now the deviations from Ehrenfest's theorem do, indeed, grow exponentially until they reach the size of the system, as is needed for Zurek's argument to succeed. But, as was shown in Sec. 4.1.2, the exponential growth of the differences between quantum state averages and classical ensemble averages will saturate before those differences reach the size of the system, and the saturation value scales with a small power of $\hbar$. Hence, for the actual (small) value of $\hbar$, the QC differences in the Liouville regime can remain small for all time, and there is no effective *break time* for the regime of classicality.

The differences in $\langle J_z \rangle$ become vanishingly small in the classical limit, but this does not imply that the full quantum probability distribution converges to the classical limit. We know that the quantum probability distribution will not converge to the classical distribution in a pointwise fashion. But we can ask what resolution is needed for a detector to be able to discriminate between these two distributions. Let us suppose that two probability distributions are practically indistinguishable when $|qm - cl|_1 < 0.01$. Using scaling result in Fig. 5.12, we find that a resolution Δ_s of 1 part in $10^{-60} rad/s$ is needed to resolve the two probability distributions. This suggests that it would be practically impossible to observe the quantum effects in the probability distributions, even without invoking environmental decoherence.

5.5.2 Environmental Effects on Hyperion

There are many environmental perturbations that can affect the satellite: random motion of the particles within the satellite, random collisions with interplanetary dust, and random light fluctuations from the sun, to name a few. We shall consider the random collisions with dust particles as an example.

To do this we treat the interplanetary dust as a dilute gas, and Hyperion as a sphere rotating about a fixed axis under the influence of random motion of the fluid. The dimensional momentum diffusion parameter is [14]

$$\tilde{D} = 16\pi k \mathcal{T} R_h^3 \eta \tag{5.6}$$

Using Eq. (E.4), the dimensionless momentum diffusion parameter D is

$$D = \frac{8\pi k \mathcal{T} R_h^3 \eta T^3}{I_3^2} \tag{5.7}$$

Here T is the temperature, k is Boltzmann's constant, R_h is the radius of Hyperion, and η is the kinetic viscosity of the dust fluid, which, following [37], is calculated to be

$$\eta = \frac{nm\bar{v}L}{3\sqrt{2}} \tag{5.8}$$

Here $\bar{v}$ is the rms velocity of the dust particles, m is their mass, n is their number density, and $L = 1/n\pi r^2$ is their mean-free-path, and r is the radius of a dust particle.

The properties of interplanetary dust was measured by the Voyager space probes. The average number density of particles near Saturn is $n = 4 \times 10^{-8}$ [23]. The average mass of the dust grains is estimated to be $m = 10^{-10}g$, and their radius is about $r = 10^{-6}$ m. The temperature in the vicinity of Saturn is about $\mathcal{T} \approx 135K$ [11].

Using Eq. (5.8), treating Hyperion as a sphere of radius $R_h = 150$ km, and using $\eta = 1.8 \times 10^{-6}$ Pa·s for the kinetic viscosity, we estimate the dimensionless angular momentum diffusion parameter to be $D \approx 6.4 \times 10^{-50}$. Even such a small value is sufficient to reduce $|qm - cl|_1$ substantially. Using Eq. (5.2), the order of magnitude of $|qm - cl|_1$ for Hyperion is found to be $|qm - cl|_1 \approx 10^{-10}$. This implies that the classical and quantum probability distributions will almost exactly agree for a large body such as Hyperion. Without the influence of the environment, the value of $|qm - cl|_1$ due to the very fine-scale differences between the quantum and classical probability distributions might be of order unity. But, of course, these differences would be impossible to resolve, because they exist on such a very fine scale. So the effect of decoherence is to destroy a fine structure that would be unobservable anyhow.

5.6 Summary

The regular and chaotic dynamics of a satellite rotating under the influence of tidal forces was examined, with application to the motion of Hyperion. Quantum and classical mechanics were compared for both types of initial state, and the scaling with $\hbar$ of the quantum-classical (QC) differences was determined. The effect of the environment was modeled, and its effect on the QC differences was estimated, so as to determine whether environmental decoherence is needed to account for the classical behavior of a macroscopic object like Hyperion. Two measures of the differences between quantum and classical mechanics were examined: the QC difference in the average angular momentum, $\Delta\langle J_z\rangle$, and the differences between the probability distributions, $|qm - cl|_1$ (Eq. (3.3)).

For early times, the QC differences in $\langle J_z\rangle$ grow in time as τ^2 for the non-chaotic state, and as $e^{2.9\tau}$ for the chaotic state. At longer times, the QC differences saturate for the chaoric state, but oscillate quasi-periodically for the non-chaotic state. The magnitude of the QC differences scale as β^2 (dimensionless $\hbar$) at early times, for both the chaotic and non-chaotic states. This β^2 scaling persists for all times for the non-chaotic state. But the QC differences that occurs in the saturation regime of the chaotic state scale as $\beta^{2/3}$. A similar scaling has also been observed for a model of two coupled rotors [7], so this result is not peculair to the particular model studied in this paper.

The value of the dimensionless $\hbar$ for Hyperion is $\beta = 9.3 \times 10^{-58}$, for which the $\beta^{2/3}$ scaling relation predicts a maximum value for the QC difference in $\langle J_z\rangle$ to be 5×10^{-37}. Therefore, there is no need to invoke environmental decoherence to explain the classical behavior of $\langle J_z\rangle$ for a macroscopic object like Hyperion.

Although the differences between the quantum and classical averages of observables become very small in the macroscopic limit, this need not be true for the differences between quantum and classical probability distributions. Indeed, the quantum probability distributions do not converge pointwise to the classical probability distributions, for either the non-chaotic or the chaotic states. A modest amount of smoothing of the quantum distribution reveals that it is made up of an extremely fine-scale oscillation superimposed upon a smooth background, and its is that smooth background that converges to the classical distribution. Similar behavior has been found for other one-dimensional systems [5]. This smoothing can be regarded as an inevitable consequence of the finite resolving power of the measuring apparatus. Alternatively, it may be impossible to observe the fine structure because of environmental decoherence. At the macroscopic scale of Hyperion, the primary effect of decoherence is to destroy a fine structure that is anyhow much finer than could ever be resolved by measurement.

When the environment was included, the results were found to follow a scaling relationship proposed by [36]: the maximum distance between the classical and the quantum probability distributions is proportional to $(\beta^2/D)^{1/6}$. Here D is the momentum diffusion parameter (see Appendix E). This suggests that the quantum probability distributions will approach the classical distributions pointwise as $\beta \to 0$, provided that D is non-zero. With environmental perturbations included, the QC differences in the probability distributions scaled as $|qm - cl|_1 \propto \beta^{1/3}$. A similar scaling was also found for two autonomous coupled rotors [7]. This suggests that pointwise convergence of the quantum probability distribution to the classical value may be typical for systems with more than one degree of freedom, and the lack of such convergence for systems with only one degree of freedom may be pathological. The role of the environment, in the model of this paper, is then to cure this pathology by supplying more degrees of freedom.

Taking D to be the momentum diffusion parameter for rotation of Hyperion due to collisions with the interplanetary dust around Saturn, we find (estimated from Eq. (5.2)) that the maximum of $|qm - cl|_1$ that Hyperion should exhibit should be of order 10^{-10}. Thus decoherence would cause the quamtum probability distribution to converge to the classical distribution in essentially a pointwise fashion.

Coarse graining (due to the finite resolution power of the measurement apparatus) will also decrease the QC differences in the probability distributions. In the saturation regime, the measure $|qm - cl|_1$ of that difference was found to be proportional to $(\beta/\Delta_s)^{0.44}$, where Δ_s is the width of the smoothing filter. This shows that decoherence and smoothing have similar effects. But they are not exactly equivalent, since their effects scale with somewhat different values of β.

In conclusion, we find that, for all practical purposes, the quantum theory of the chaotic tumbling motion of Hyperion will agree with the classical theory, even without taking account of the effect of the environment. Decoherence aids in reducing the quantum-classical differences, but it is not correct to assert that envoronmental decoherence is the root cause of the appearence of the classical world.

Chapter 6

Floquet States

Energy eigenstates do not exist in time dependent systems. However for systems with periodic potentials the eigenstates of the discrete time evolution operator can provide similar insights. The discrete time evolution operator, called the Floquet operator, is simply $\hat{U}(0,T)$, where T is the period of the potential.

The state vector for a system can be found at $t = nT$ by multiplying the initial state by the Floquet operator n times. This discrete time evolution operator cannot be deduced analytically this model of Hyperion our model when $e \neq 0$, but its matrix elements can be found numerically via

$$U_{nm} = \langle n|U(0;T)|m\rangle = \langle n|m(T)\rangle \tag{6.1}$$

Here U_{nm} is a matrix element of the Floquet operator, and $|m\rangle$ and $|n\rangle$ are angular momentum eigenstates. Any eigenvector of Eq. (6.1) satisfies

$$\hat{U}(0,T)|F_n\rangle = e^{i\phi_n}|F_n\rangle \tag{6.2}$$

ϕ_n is called the eigenphase or quasi-energy of the Floquet state $|F_n\rangle$.

In this chapter the properties of Hyperion's Floquet states are investigated, to determine whether chaotic states have different localization properties than non-chaotic ones. I will also show that individual Floquet states give little information about the classical limit, but ensembles of them do.

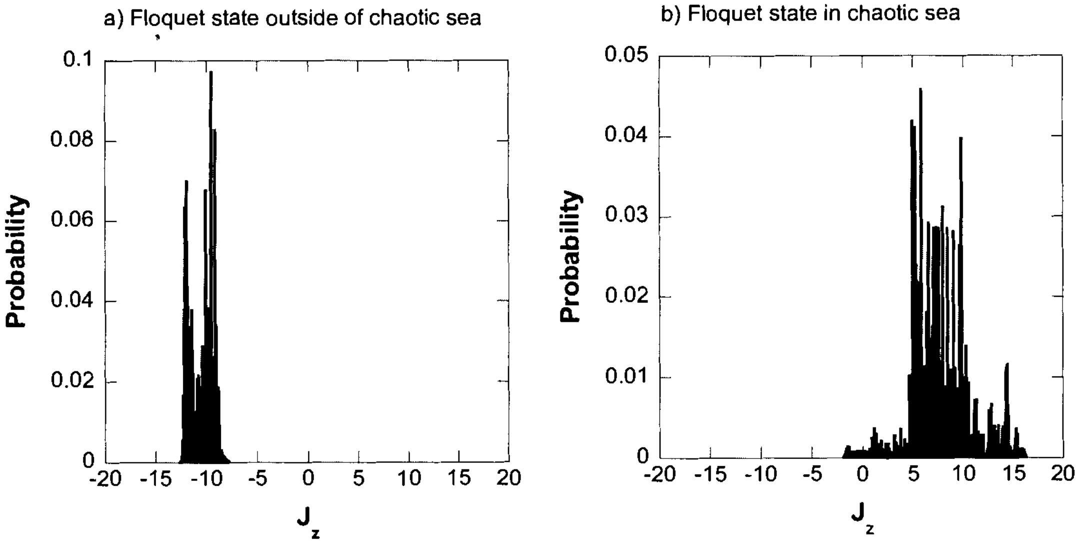

Figure 6.1: Floquet states for J=400 ($\alpha = 0.5$, $e = 0.1$, $\beta = 0.05$)

6.1 Localization Properties of Floquet States for Hyperion

Localization is an interesting phenomenon that occurs in some chaotic systems, and in this section we will examine if it occurs in our model. An eigenfunction is localized if it is primarily located in a restricted range in position or momentum. This phenomenon is particularly interesting because localization can occur in the chaotic sea, causing eigenstates to be much narrower than the microcanonical probability distribution would imply.

This was first observed in Anderson localization [1], where a disordered potential causes the eigenstates to decay exponentially in position about a site, as opposed to the Bloch functions which fill all space. More recently it was shown that the quantum kicked rotor is algebraically equivalent to Anderson localization [21], hence rotor's momentum eigenfunctions are also exponentially localized. This localization also occurs in the chaotic sea, and so these states can have widths there can be narrower than the microcanonical distribution would predict.

The kicked top, on the other hand, does not exhibit localization in the chaotic sea [24]. Its eigenstates tend to be spread over the entire accessible phase space, as the microcanonical distribution would predict. More importantly, eigenstates centered

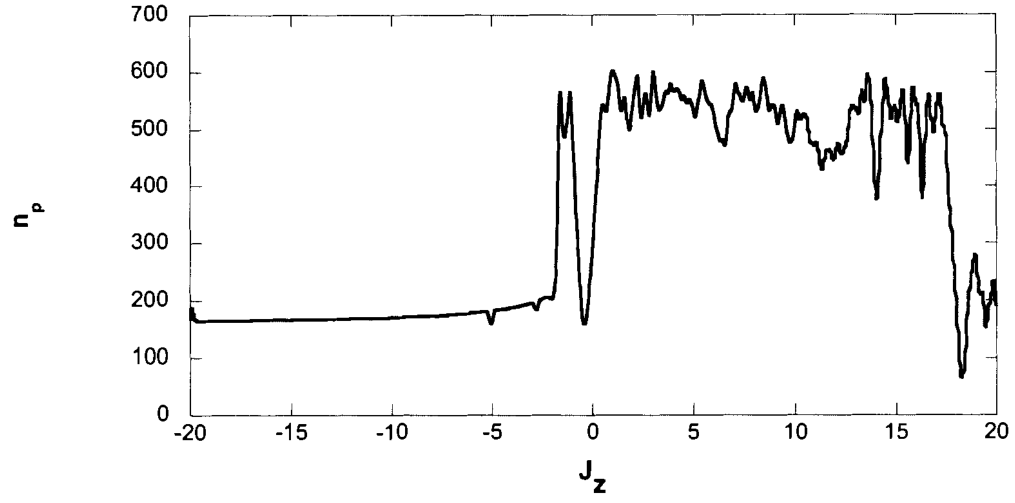

Figure 6.2: Participation numbers (n_p) for minimum uncertainty Gaussian state centered at $\phi = 0$ and $J_z = -20 \cdots 20$ for J=800 ($\beta = 0.025, \alpha = 0.5$, $e = 0.1$), measured in the basis of Floquet states.

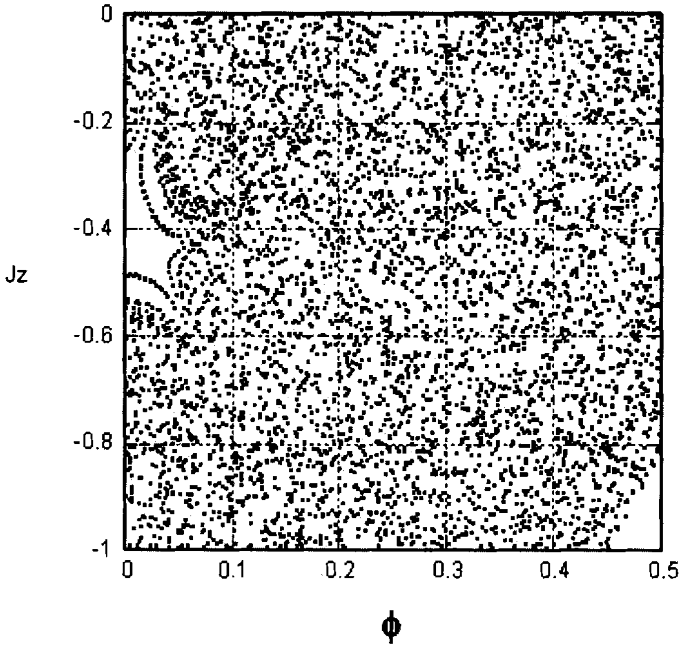

Figure 6.3: Poincare Section for $\alpha = 0.5, e = 0.1$, zoomed in to show that the anomaly in n_p actually corresponds to a small regular island (see Fig. 4.1).

in non-chaotic regions of phase space are dramatically narrower than their chaotic brethren. In Haake's work [24], these widths were measured by the number of eigenstates needed to represent a minimum uncertainty state in a regular or chaotic part of phase space, and he found these numbers were proportional to $\hbar^{-0.5}$ and $\hbar^{-1}$, for regular or chaotic states respectively. Since the size of the Hilbert space of the kicked top increases as $\hbar^{-1}$, the chaotic states will have constant width in the classical limit, but the regular states will have vanishing width even though their participation numbers increase.

Here we will carry out a similar analysis, to see if, like the kicked top the widths of the eigenstates differ radically between regular and chaotic eigenstates, or if the chaotic Floquet states are localized like the kicked rotor's. To measure the number of Floquet states needed to represent a state we use the participation number n_p which is defined by

$$n_p^{-1} = \sum_{n=-K}^{K} |a_n|^4 = \sum_{n=-K}^{K} |\langle F_n|\psi\rangle|^4 \tag{6.3}$$

Here a_n are the coefficients of the Floquet states used to represent the minimum uncertainty state, and $|\psi\rangle$ is given by

$$|\psi\rangle = \frac{1}{N}\sum_{m=-K}^{K} \exp(-(\beta^2 m^2 - J_0)^2/(2\beta) - i\phi_0)|m\rangle \tag{6.4}$$

The values of ϕ_0, J_0 can be chosen to center this state in any location in phase space, and because we know this function's width in phase space, we will be able to center it in a chaotic region of the Poincare section. By knowing that a state is regular or chaotic, we will be able to determine if the eigenstates that compose it are localized. This will allow us to determine if, like the kicked top, there is a difference in localization between regular Floquet states and chaotic Floquet states.

To show this I found n_p for a sequence of minimum uncertainty states along the line $\phi = 0$ from $J_z = -20 \cdots 20$. From Fig. 4.1, this line passes through both chaotic and regular regions of phase space, and so we will be able to determine whether there is a localization difference if n_p changes abruptly as we move from a regular to a chaotic region.

The localization differences between chaotic and non-chaotic Floquet states can be seen in figure 6.2. By comparing this figure to Fig. 4.1 it is clear that n_p is greater in chaotic regions than in non-chaotic regions. The abnormally low participation

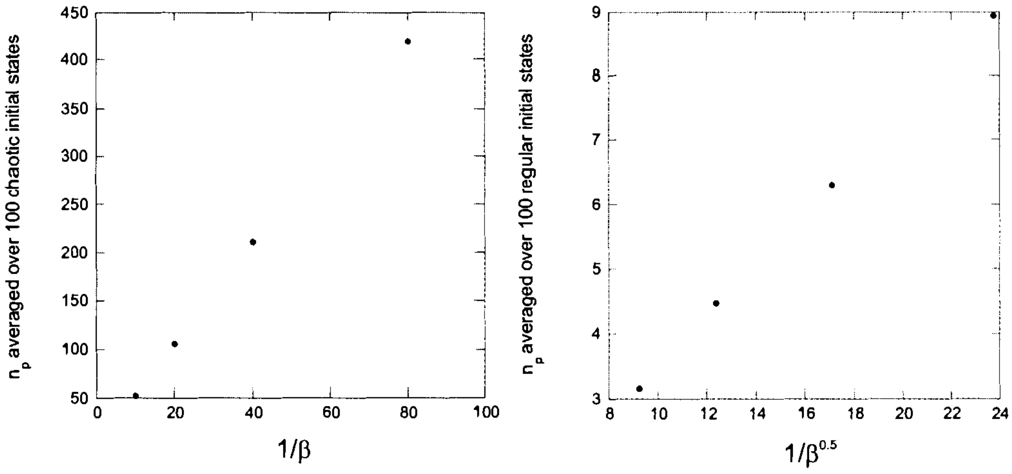

Figure 6.4: Participation number (n_p) measured in angular momentum basis, averaged over 100 chaotic and non-chaotic minimum uncertainty states vs β

numbers at $J_z \approx -0.5$ corresponds to a small regular island that is hard to see in Fig. 4.1 but can be seen more clearly in Fig. 6.3.

To see if this agrees with Haake's work, we must examine how n_p varies with β. From Fig. 6.2 the participation ratio does not assume a constant value for chaotic states, but is subject to fluctuations. These fluctuations can be reduced by averaging n_p for a large number of states, leaving a better estimate of the characteristic value of n_p for regular or chaotic states.

Figure 6.4 shows that regular and chaotic Floquet states have different localization behavior as $\beta \to 0$. To reduce the fluctuations in n_p, its value was averaged for 100 eigenstates for each β considered. For chaotic Floquet states n_p is proportional to β^{-1}, implying that the widths of the Floquet states remain constant as $\beta \to 0$ for this model. For non-chaotic Floquet states n_p is proportional to $\beta^{-0.5}$, implying that they are localized. These proportionalities were also noted for the kicked top in non-chaotic and chaotic states [24], suggesting that they may be typical for regular and chaotic systems.

6.2 Distributions in the Saturation Regime

Floquet states are the states that remain the same after evolving over one period of the potential. In classical mechanics the only probability distributions that remain constant as time progresses are the distribution that fills the chaotic sea and uniform distributions on the regular torii. So if the classical limit is reached, then the Floquet states must resemble the classical distribution in the saturation regime. In this section I will show how the classical probability distribution is encoded within Hyperion's Floquet states, and show why the expectation values converge to the classical limit in the saturation regime despite large quantum fluctuations.

We know from Fig. 6.1 and Fig. 5.5, that the probability distributions of individual Floquet states do not correspond to classical probability distributions in the saturation regime. However ensembles of Floquet states might do so. By combining the chaotic Floquet states with uniform weight, the resulting probability distribution does not appear to be qualitatively different from the quantum probability distribution in the saturation regime seen in figure 4.6. So the classical probability distribution does not emerge out of a uniform combination of these states.

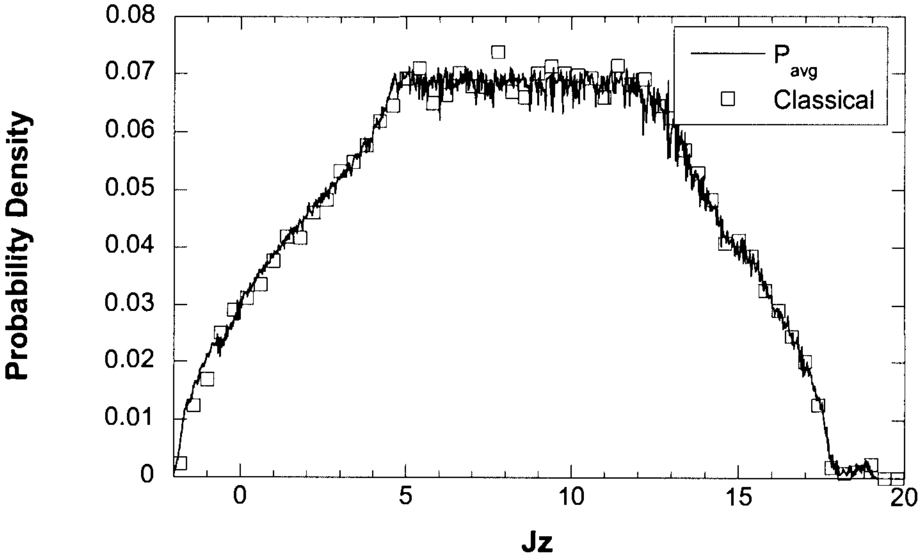

Figure 6.5: Average of all 533 chaotic Floquet probability distributions (denoted P_{avg}) for $\alpha = 0.5, e = 0.1, \beta = 0.025$, 1068 non-chaotic Floquet states were omitted.

There is more than one way to construct this combination, since the relative phases of the Floquet states are arbitrary. Another way to see if ensembles of chaotic Floquet states contain the classical probability distribution, is through the probability distribution $P_{\text{avg}}(m) = \sum_i^N |\langle m|F_i\rangle|^2/N$. That is to say, the classical probability distribution for the chaotic sea might be stored in the average of all N chaotic Floquet probability distributions.

This is exactly what we find in Fig. 6.5, where the classical probability distribution at $t = 40$ is recovered by averaging the momentum distributions of a sufficient number of chaotic Floquet states. This suggests that single Floquet probability distributions do not correspond to the classical distribution in the saturation regime, but their average does.

6.2.1 Randomness of the QC Differences

In the previous section we observed that when we average the chaotic Floquet probability distributions in the saturation regime, we find the classical result. This by its self is an interesting result, but we can also use it to explain why the QC differences in $\langle J_z\rangle$ are small for Hyperion in the saturation regime, even though the differences in $|qm - cl|_1$ are large. This may appear to be a conspiracy at first, since the large differences in the probability distributions must somehow cancel each other out in order for the expectation values to correspond to the classical result. This section shows that the quantum fluctuations about the classical probability distribution in the saturation regime are quasi-random, and will average to 0 in the classical limit.

To show the random nature of the QC differences, consider a wave function $\psi(k) = \sum_n c_n F_n(k)$, where $F_n(k) = \langle k|F_n\rangle$ is the Floquet wavefunction in angular momentum representation. Then the angular momentum probability distribution for this state at $\tau = NT$ is

$$P(k, NT) = \sum_n |c_n|^2 |F_n(k)|^2 + \sum_m \sum_{n\neq m} c_n c_m^* e^{iN(\phi_n - \phi_m)} F_n(k) F_m^*(k) \qquad (6.5)$$

Here ϕ_n is the eigenphase of the state $|F_n\rangle$. To eliminate the imaginary part of the above equation, the complex values will be expressed in polar form: $c_n F_n(k) = R_n(k) e^{i\Phi_n(k)}$. With this substitution Eq. (6.5) becomes

$$P(k,NT) = \sum_{n} |c_n|^2 |F_n(k)|^2 + 2\sum_{m}\sum_{n>m} R_n(k)R_m(k)$$
$$\cos(N[\phi_n - \phi_m] + \Phi_n(k) - \Phi_m(k)) \tag{6.6}$$

The first term in this expansion of the probability distribution is a weighted sum of the Floquet probability distributions. Because the Floquet states are delocalized in the chaotic sea, we expect c_n to be approximately $1/N_c$, where N_c is the number of chaotic Floquet states. This is reinforced by Figure 6.2, where we found that the participation numbers for chaotic Floquet states are approximately 550 which is approximately the number of chaotic eigenstates present there. This agrees with the assumption that $c_n \approx 1/N_c$, and so the first term in the expansion should be Hyperion's classical probability distribution.

The remaining terms are the quantum interference patterns that constitute the QC differences. For sufficiently large N, the quantity $N(\phi_n - \phi_m) + \Phi_n(k) - \Phi_m(k)$ modulo 2π typically forms a quasi-random sequence that uniformly fills the interval $[0, 2\pi)$. It will not uniformly fill this interval if $(\phi_n - \phi_m)$ divides 2π, but according to random matrix theory, the distribution of eigenphases should not have a preference for multiples of π over any other number, hence it will be exceedingly unlikely that $(\phi_n - \phi_m)$ divides 2π. This rare occurrence will be neglected, and so the resulting probability distribution should be the classical result with quasi-random quantum fluctuations.

The probability distribution can then be written as $P(k) = P_c(k) + P_r(k)$, where $P_c(k)$ is the classical probability distribution and $P_r(k)$ are quasi-random QC differences. We can easily show that $P_r(k)$ will have, on average, no effect on the expectation values in the classical limit. We begin by writting $P_r(k)$ as

$$P_r(k) = 2\sum_{m}\sum_{n>m} R_n(k)R_m(k)r_{nm}(k) \tag{6.7}$$

Here $r_{nm}(k) = \cos(N(\phi_n - \phi_m) + \Phi_n(k) - \Phi_m(k))$ which is for sufficiently large N is a random function in n and m with mean 0. This is important because this renders the choice of initial phase of c_n irrelevant, since time evolution will eventually randomize it.

Random matrix theory suggests that the joint probability distribution of $F_n(k) = \langle k|F_n\rangle$ should be uniform on the surface of a 2K+1 dimensional hypersphere of unit radius [24]. Because the distribution does not depend on the phase, the phases of $F_n(k) = \langle k|F_n\rangle$ should be uniformly distributed in $[0, 2\pi)$. The distribution of these phases for Hyperion's Floquet states appears to agree with this assumption. Hence, according to random matrix theory, r_{nm} should be a random function in n, m and k for large N.

To see how these differences behave in the classical limit, I will consider the effect of $P_r(k)$ on $\langle J_z\rangle$ as the size of the Hilbert space, K, goes to ∞,

$$\begin{aligned}
\lim_{K\to\infty} |\langle kP_r(k)\rangle| &= \lim_{K\to\infty}\left|\sum_m \sum_{n>m} \frac{2}{2K+1}\sum_{k=-K}^{K} kR_n(k)R_m(k)r_{nm}(k)\right| \\
&\leq \lim_{K\to\infty}\left|\sum_m \sum_{n>m} \frac{2}{2K+1}\sum_{k=-K}^{K} kr_{nm}(k)\right| \\
&= \lim_{K\to\infty}\left|\frac{2}{2K+1}\sum_{k=-K}^{K} k\tilde{r}(k)\right| \qquad (6.8)
\end{aligned}$$

Here $\tilde{r}(k) = \sum_m \sum_{n>m} r_{nm}(k)$. By the central limit theorem, $\tilde{r}(k)$ should have a Gaussian distribution for large K, but should still have the same mean value of 0. Hence,

$$\lim_{K\to\infty}\left|\frac{2}{2K+1}\sum_{k=-K}^{K} k\tilde{r}(k)\right| = 0 \qquad (6.9)$$

This shows that $\langle J_z\rangle$ will approach the classical limit if the average of the Floquet probability distributions is the classical probability distribution in the saturation regime, and if the system agrees at least qualitatively with RMT. Hence it is no coincidence that the large quantum fluctuations in the saturation regime have no effect on $\langle J_z\rangle$ in the classical limit of Hyperion.

6.3 Quasi-Energy Statistics

In this section we will see to what extent this system is faithful to random matrix theory (RMT) by comparing the quasi-energy spacing distributions to the theoretically predicted values. This might prove important for subsequent analysis, which may seek to understand the QC differences that we have observed in terms of RMT.

In section 1.1 I discussed the energy level spacing statistics for time independent Hamiltonians. These statistics are given for members of Gaussian ensembles of random Hermitian matrices, which are ensembles of matrices whose elements have a Gaussian distribution. It can be shown [24], that these elements must have a Gaussian distribution so that the eigenvalues remain invariant under infinitesimal orthogonal transformations.

For time dependent systems, the random matrices in question are Floquet operators, which are unitary as opposed to the Hermitian matrices considered earlier. These random matrices are said to belong to Dyson's circular ensemble, so called because its eigenvalues lie on the unit circle [30].

Although these unitary matrices are quite different from the Gaussian ensembles of Hermitian matrices considered earlier, it turns out that the same level spacing statistics apply as the dimension of the matrix increases [24]. So the eigenphase spacing statistics depend on the symmetry class of the Hamiltonian in just the same manner as do the energy level spacings. The only modification that must be made to these distributions, is that they are now in units of the mean eigenphase spacing S, rather than the mean energy level spacing. Dyson's circular ensemble predicts that if we have N eigenvectors then the mean spacing is $2\pi/N$ hence,

$$S = \frac{N\Delta\phi}{2\pi} \tag{6.10}$$

For systems with a mixed phase space, eigenstates can be centered either in a chaotic or a regular part of phase space. From RMT the eigenphase spacing distribution for chaotic eigenstates should have a Wigner distribution, whereas regular states should have a Poissonian eigenphase distribution. Since there are both regular and chaotic eigenvectors here, the spacing distribution should be a mix between a Poisson and a Wigner distribution.

Since we are more interested in Hyperion's chaotic rotation than its non-chaotic rotation, we will find the eigenphase statistics for only the chaotic Floquet states, to see if they agree with the Wigner distribution predicted by RMT.

To determine whether a Floquet state is chaotic or not, I used the participation number. Since we know that the chaotic states are wider than non-chaotic states, we can easily determine whether the state is chaotic. For $\beta = 0.025$, states that are composed of more than 120 angular momentum states are chaotic.

The level distribution statistics for chaotic and non-chaotic states is given in figure 6.6. The level distribution for the integrable system agrees with the RMT prediction of a Poisson distribution. Our model of Hyperion obeys time reversal

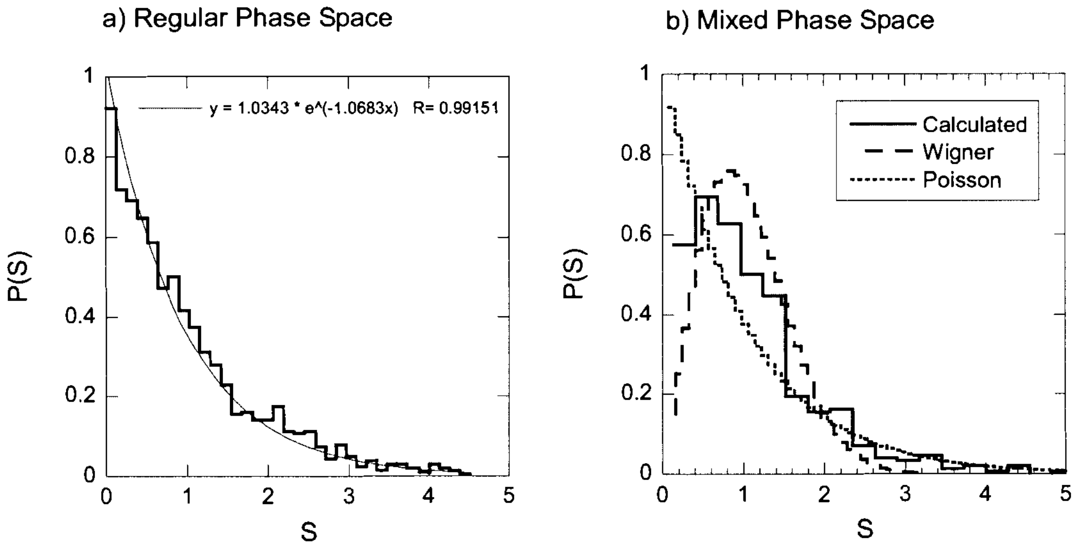

Figure 6.6: a) Quasi-energy spacing for regular phase space ($e = 0$, $\alpha = 0.5$, $\beta = 0.0125$, 3201 quasi-energies included) b) Quasi-energy spacing for mixed phase space ($e = 0.1$, $\alpha = 0.5$, $\beta = 0.025$, 561 out of 1601 quasi-energies included, selection criteria: $n_p > 120$

symmetry. RMT then predicts that the level spacing statistics should be given by $P(S) = (S\pi/2)e^{-S^2\pi/4}$.

Even after discarding any non-chaotic eigenvectors, the level distribution appears to be in between a Poisson distribution and the Wigner distribution. This is not surprising since RMT assumes that the values of matrix elements are randomly distributed. For a system with a divided phase space, there must be some ordering of these elements in order to ensure that the phase space remains divided. So we do not expect the eigenphase spacing to perfectly correspond to the predictions of random matrix theory because the Floquet operator for this system may not be random [24].

To conclude, random matrix theory does not perfectly predict the eigenphase spacing distribution for this model of Hyperion. This is not surprising because the phase space is mixed, and we typically expect the eigenphase distribution to be somewhere between the level spacing statistics for regular systems and chaotic systems. So if random matrix theory is to be used as a tool to understand this system, it should be used qualitatively.

Chapter 7

3D Motion Of Hyperion

In the previous chapters we examined the 1D rotation of an asymmetric satellite whose CM is in an elliptical orbit around a planet. Here we will extend this work to the more general case of 3D rotations. This extention is non-trivial because of problems in both the quantum and classical mechanics. When Euler angles are used, problems occur in the coordinate system at the pole. These problems cause the angles that parameterize trajectories that pass near the pole to change very rapidly, which can potentially make numerical integration unstable. In the quantum mechanics, one is faced with problems in finding the matrix elements of the potential as well as computational problems posed by the fact that the size of the Hilbert space is proportional to β^{-3}.

In this chapter I will address these problems through introducing a singularity-free parameterization of the rotation matrix, and present the recursion relations needed to find the matrix elements of the potential in angular momentum representation. I will also perform stability analysis to verify that any 1D rotation in the chaotic sea is unstable, estimate the Lyapunov exponent for Hyperion's 3D rotation, and use this to estimate how long the 1D rotation can remain stable in the chaotic sea. The quantum mechanics is left unexplored because it is too computationally expensive to solve, but the the theory is developed sufficiently so that it could be investigated when sufficient computing power becomes available.

7.1 Classical 3D Rotation

7.1.1 Euler Parameters

There is a well known problem with describing the orientation of a body by Euler angles. For any set of Euler angles there always is a point where the parameterization of the orientation is not unique. This problem is similiar to the problem of the longitude at the north pole, which is undefined. This problem with Euler angles at the pole can be understood through the rotation matrix which is given below

$$\mathbf{R} = \begin{pmatrix} \cos\phi\cos\theta\cos\psi - \sin\phi\sin\psi & \cos\phi\cos\theta\sin\psi + \sin\phi\cos\psi & -\cos\phi\sin\theta \\ -\sin\phi\cos\theta\cos\psi - \cos\phi\sin\psi & -\sin\phi\cos\theta\sin\psi + \cos\phi\cos\psi & \sin\phi\sin\theta \\ \sin\theta\cos\psi & \sin\theta\sin\psi & \cos\theta \end{pmatrix} \tag{7.1}$$

This can be written more compactly as the matrix product $\mathbf{R_z}(\psi)\mathbf{R_y}(\theta)\mathbf{R_z}(\phi)$, where $\mathbf{R}_z$ corresponds to rotation about the z-axis etc. It is clear that when $\theta = 0$, $\mathbf{R_y}$ becomes the identity which commutes with the other two rotation matrices. The net rotation then is $\phi + \psi$ about the z-axis. Hence there are an infinite number of angles ϕ and ψ which describe the same rotation, and so Euler angles are ambiguous when $\theta = 0$. In addition, for trajectories passing close to this singular point, ϕ and ψ can vary rapidly even though the rotation matrix describing the orientation does not change significantly. This implies that the tolerance on a numerical integrator will be severely tested for these trajectories.

These singular points are clearly problematic, but since they are artifacts of the coordinate system they can be removed by choosing a better parameterization of the rotation. There are other coordinates that do not have singular points, such as the complex valued Cayley Klein parameters [22], and an algebraically equivalent set of quaternions called Euler parameters. Here we will restrict our attention to these parameters, which are defined through the $\mathbf{SO(3)}$ rotation matrix:

$$\mathbf{R} = \begin{pmatrix} B_0^2 + B_1^2 - B_2^2 - B_3^2 & 2B_1B_2 - 2B_0B_3 & 2B_1B_3 + 2B_0B_2 \\ 2B_1B_2 + 2B_0B_3 & B_0^2 + B_2^2 - B_3^2 - B_1^2 & 2B_2B_3 - 2B_0B_1 \\ 2B_1B_3 - 2B_0B_2 & 2B_2B_3 + 2B_0B_1 & B_0^2 + B_3^2 - B_1^2 - B_2^2 \end{pmatrix} \tag{7.2}$$

In contrast to the Euler angle representation of the matrix, there are no trigonometric functions present. Instead of trig functions, a set of 4 parameters B_i are used. To guarantee that the matrix will rotate the coordinate system and not stretch it, the following constraint must be imposed

$$\bar{B}^T\bar{B} = 1 \tag{7.3}$$

where $\bar{B}^T = [B_0, B_1, B_2, B_3]$. Unlike the Euler angles, any set of 4 Euler parameters corresponds to a unique $\mathbf{SO(3)}$ rotation matrix. This can be seen by considering a particular rotation matrix $\mathbf{R}$ and finding the particular $\bar{B}$ that corresponds to that matrix. By setting the elements of $\mathbf{R}$ equal to those of Eq. (7.2) we obtain a set of 6 linearly independant quadratic equations. These equations, combined with the constraint $\bar{B}^T\bar{B} = 1$, are sufficient to find a unique representation of $\mathbf{R}$ in terms of $\bar{B}$. By solving the system of equations, we obtain the following solutions for $\bar{B}$ in terms of the elements of the rotation matrix [10]

$$\begin{aligned} \mathrm{tr}\,\mathbf{R} \neq -1 : B_0 &= \frac{1}{2}\sqrt{1 + \mathrm{tr}\,\mathbf{R}}, \quad B_i = -(\mathbf{R}_{jk} - \mathbf{R}_{kj})/(4B_0) \text{ i,j,k cyclic} \\ \mathrm{tr}\,\mathbf{R} = -1 : B_0 &= 0, \qquad\qquad\quad B_i = \mathrm{sign}(B_i)\sqrt{(1 + \mathbf{R}_{ii})/2} \end{aligned} \tag{7.4}$$

Here $\mathrm{sign}(B_1) = 1$, $\mathrm{sign}(B_2) = \mathrm{sign}(\mathbf{R}_{12})$, $\mathrm{sign}(B_3) = \mathrm{sign}(\mathbf{R}_{13})$. Although any set of Euler angles may be converted into Euler parameters using Eq. (7.4), the converse is not necessarily true. For example Euler angles have more than one representation for the pole, thus it is impossible to uniquely convert Euler parameters to Euler angles there.

7.1.2 Derivation of Equation of Motion

The dynamics of rotating bodies using the Euler parameters is derived elegantly in a paper by Harold J. Morton Jr. [32] from the Euler equations for rigid body rotation. Here I will present a brief summary of the derivation of these equations of motion for a rigid body.

To begin we need to find the composition rule for rotations using Euler parameters. Assume the set of angles $\bar{B}'$ give the orientation of the frame F_1 with respect to the frame F, and $\bar{B}''$ gives the orientation of the frame F_2 with respect to F_1. Then the rotation matrix $\mathbf{R}(\bar{B})$ that transforms F into F_2 directly can be directly found by the relation

$$\mathbf{R}(B) = \mathbf{R}(\bar{B}'')\mathbf{R}(\bar{B}') \tag{7.5}$$

This equation can be algebraically solved for B using Eq. (7.4), but rather than giving the resulting expressions, it is more convenient to write the solution in terms of a matrix product

$$\bar{B} = \mathbf{Q}(\bar{B}'')\bar{B}' \tag{7.6}$$

Here $\mathbf{Q}$ is a rotation matrix of the form

$$\mathbf{Q}(\bar{B}) = \begin{bmatrix} B_0 & -B_1 & -B_2 & -B_3 \\ B_1 & B_0 & B_3 & -B_2 \\ B_2 & -B_3 & B_0 & B_1 \\ B_3 & B_2 & -B_1 & B_0 \end{bmatrix} \tag{7.7}$$

This matrix $\mathbf{Q}$ and a related matrix $\mathbf{S}$ are extremely convenient to use because of their algebraic properties. The most relevant of these are

$$\begin{aligned} \mathbf{Q}(\bar{a})\mathbf{Q}^T(\bar{a}) &= |\bar{a}|^2\mathbf{I} = \mathbf{S}(\bar{a})\mathbf{S}^T(\bar{a}) \\ \mathbf{Q}(\bar{a})\bar{b} &= \mathbf{S}(\bar{b})\bar{a} \end{aligned} \tag{7.8}$$

$\mathbf{S}$ is similar to the matrix $\mathbf{Q}$ but with the lower right 3×3 block transposed

$$\mathbf{S}(\bar{B}) = \begin{bmatrix} B_0 & -B_1 & -B_2 & -B_3 \\ B_1 & B_0 & -B_3 & B_2 \\ B_2 & B_3 & B_0 & -B_1 \\ B_3 & -B_2 & B_1 & B_0 \end{bmatrix} \tag{7.9}$$

We will now turn our attention to relating the time derivatives of the Euler parameters to angular velocities. If ω_i can be written in terms of $\bar{B}$, then we can substitute this into Euler's equations for rigid body motion to find the equation of motion for $\bar{B}$. To do this we consider a time dependant infinitesimal rotation parameterized by $\bar{B}$ of the form

$$\mathbf{R}(B(t)) = \begin{bmatrix} 1 & \omega_3 t & -\omega_2 t \\ -\omega_3 t & 1 & \omega_1 t \\ \omega_2 t & -\omega_1 t & 1 \end{bmatrix} \mathbf{R}(\bar{B}(0)) \tag{7.10}$$

By finding the Euler parameters using 7.4 that correspond to the rotation matrix $\mathbf{R}(\bar{B}(t))$, and differentiating the result with respect to t we obtain

$$\frac{\partial \bar{B}}{\partial t} = \frac{1}{2}\mathbf{Q}(\bar{\omega})\bar{B} \tag{7.11}$$

Here $\bar{\omega}$ is the angular velocity of the rotation, promoted to a 4 vector of the form $\bar{\omega}^T = [0, \omega_1, \omega_2, \omega_3]$. This relation allows us to write angular velocities in terms of $\dot{\bar{\beta}}$. Or equivalently we can use Eq. (7.8) to solve for $\bar{\omega}$,

$$\bar{\omega} = 2\mathbf{S}^T(\bar{B})\dot{\bar{B}} \tag{7.12}$$

To make the connection to Euler's equations, we must convert this to an angular momentum, which can easily be done by

$$\frac{\partial \bar{L}}{\partial t} = \mathbf{I}\bar{\omega} = 2\mathbf{I}\mathbf{S}^T(\bar{B})\dot{\bar{B}} \tag{7.13}$$

Here $\mathbf{I}$ is the moment of inertia tensor promoted to 4 dimensions. This tensor can be expressed in a principle axis body fixed frame as

$$I_{\mu,\nu} = \delta_{\mu,\nu} I_{\mu,\nu} \tag{7.14}$$

The value of $I_{0,0}$ is largely irrelevant to the dynamics, since ω_0 is 0. It cannot be given a value of 0, because then the matrix would not be invertible. This is a mathematical technicality because the inverse of this matrix is needed in order to find the equations of motion using this approach. Hence $I_{0,0}$ can be given any non-zero value without altering the dynamics.

From Eq. (7.13), the time derivative of the angular momentum is

$$\frac{\partial \bar{L}}{\partial t} = 2\mathbf{I}\mathbf{S}^T(\dot{\bar{B}})\dot{\bar{B}} + 2\mathbf{I}\mathbf{S}^T(\bar{B})\ddot{\bar{B}} \tag{7.15}$$

This differential equation must be equivalent to Euler's equation, which in terms of these matrices reads

$$\frac{\partial \bar{L}}{\partial t} = \frac{1}{2}[\mathbf{Q}(\bar{\omega}) - \mathbf{S}(\bar{\omega})] + \bar{M} \tag{7.16}$$

Where $\bar{M}$ is the torque promoted to a 4-vector of the form $[0, T_1, T_2, T_3]$. This choice of $M_0 = 0$ is justified because $L_0 = 0$ for all time. Using Eq. (7.11) and Eq. (7.6) this expression can be converted into

$$\frac{\partial \bar{L}}{\partial t} = \mathbf{Q}(\dot{\bar{B}})\mathbf{Q}^T(\bar{B}) - \mathbf{S}^T(\bar{B})\mathbf{S}(\dot{\bar{B}}) + \bar{M} \tag{7.17}$$

Equating Eq. (7.15) to Eq. (7.17) and solving for $\ddot{\bar{B}}$ yields the Lagrange equations of motion (A pair of sign errors are present in Morton's paper [32] and they are corrected here).

$$\begin{bmatrix} \ddot{B}_0 \\ \ddot{B}_1 \\ \ddot{B}_2 \\ \ddot{B}_3 \end{bmatrix} = -\left(\sum_{i=0}^{3} \dot{B}_i^2\right) \begin{bmatrix} B_0 \\ B_1 \\ B_2 \\ B_3 \end{bmatrix} + \frac{1}{2} \begin{bmatrix} -B_1K_1 - B_2K_2 - B_3K_3 \\ B_0K_1 - B_3K_2 + B_2K_3 \\ B_3K_1 + B_0K_2 - B_1K_3 \\ -B_2K_1 + B_1K_2 + B_0K_3 \end{bmatrix} \tag{7.18}$$

Here the K's are:

$$\begin{aligned} K_1 &= [(I_2 - I_3)\omega_2\omega_3 + M_1]/I_1 \\ K_2 &= [(I_3 - I_1)\omega_3\omega_1 + M_2]/I_2 \\ K_3 &= [(I_1 - I_2)\omega_1\omega_2 + M_3]/I_3 \end{aligned} \tag{7.19}$$

Here ω_i is the angular velocity about the body fixed i-axis, and M_i represents the torque about that axis. The similarity to Euler's equations in Eq. (7.19) is striking, but not surprising considering since they are used as a starting point for the derivation of the Lagrange equations.

The torque as a function of $\partial_{B_i} V(\bar{B})$ can be found using the Lagrangian or Hamiltonian formalism. This process is fairly lengthy [32], and for brevity we will omit the details of this derivation and provide the result,

$$\bar{M} = \frac{-1}{2}\mathbf{Q}^T(\bar{B}) \begin{bmatrix} \partial V/\partial B_0 \\ \partial V/\partial B_1 \\ \partial V/\partial B_2 \\ \partial V/\partial B_3 \end{bmatrix} \tag{7.20}$$

Using this method, the rotation of any body in 3 dimensions can be calculated, and the resulting $\dot{\bar{B}}$ can be converted back into angular velocities if desired using Eq. (7.11).

7.1.3 Potential Energy in Euler Parameters

Here we will express the potential energy of Hyperion in terms of the Euler parameters. For this model of Hyperion, the potential depends on the moments of inertia. These moments of inertia depend in turn on the orientation of the body, causing the potential energy to be a function of these parameters. This function is,

$$V(\bar{B}) = \frac{1}{2}\frac{Gm}{r^3}(2I_1(\bar{B}) - I_2(\bar{B}) - I_3(\bar{B})) \tag{7.21}$$

We can find these elements of the moment of inertia tensor by rotation using $\mathbf{I}(\bar{B}) = \mathbf{R}(\bar{B})\mathbf{I}_0\mathbf{R}^{-1}(\bar{B})$. The potential can then be found by substituting $\mathbf{I}(\bar{B})$ into Eq. (7.21). Thus we obtain

$$\begin{aligned}
V(\bar{B}) = {} & \frac{Gm}{4r^3}\{[(3\,{B_0}^4 - 18\,{B_0}^2\,{B_3}^2 + 3\,{B_1}^4 - 18\,{B_1}^2\,{B_2}^2 + 3\,{B_2}^4 + 3\,{B_3}^4)\,A \\
& + (-24\,B_1\,B_3\,B_0\,B_2 + 6\,{B_1}^2\,{B_3}^2 - 6\,{B_0}^2\,{B_1}^2 - 6\,{B_2}^2\,{B_3}^2 + 6\,{B_0}^2\,{B_2}^2)\,C) \\
& \times\cos(2\,\gamma) + ((12\,B_3\,{B_0}^3 - 12\,B_2\,{B_1}^3 + 12\,{B_2}^3\,B_1 - 12\,{B_3}^3\,B_0)\,A \\
& + (-12\,{B_3}^2\,B_2\,B_1 + 12\,{B_0}^2\,B_2\,B_1 - 12\,{B_1}^2\,B_3\,B_0 + 12\,{B_2}^2\,B_3\,B_0)\,C)\sin(2\,\gamma) \\
& + (-24\,B_1\,B_3\,B_0\,B_2 - 6\,{B_0}^2\,{B_2}^2 + 6\,{B_2}^2\,{B_3}^2 + 6\,{B_0}^2\,{B_1}^2 - 6\,{B_1}^2\,{B_3}^2)\,A \\
& +(-2\,{B_1}^2\,{B_2}^2 - {B_3}^4 + 4\,{B_0}^2\,{B_1}^2 - {B_2}^4 + 4\,{B_0}^2\,{B_2}^2 + 4\,{B_2}^2\,{B_3}^2 + 4\,{B_1}^2\,{B_3}^2 \\
& - 2\,{B_0}^2\,{B_3}^2 - {B_1}^4 - {B_0}^4]C\}
\end{aligned} \tag{7.22}$$

Here $A = I_2 - I_1, C = I_1 + I_2 - 2I_3$, and γ is the orientation of the satellite's cm with respect to the space fixed x-axis.

This potential is more general than the one derived in section 2, so it should reduce to 2.4 when the rotations are 1D. From Eq. (7.2) it can be seen that $B_0 = \cos(\phi/2), B_1 = 0, B_2 = 0, B_3 = \sin(\phi/2)$ describes a 1D rotation about the z-axis, and as expected this substitution results in the potential becoming

$$V = \frac{3\pi^2}{T^2}(I_2 - I_1)\cos(2\phi - 2\theta) \tag{7.23}$$

This is the potential for 1D rotations that was found in chapter 2, verifying that this potential reduces to the correct limit for 1D rotations. With the potential written in terms of $\bar{B}$ we have all the tools we need to derive the equations of motion for the system.

7.1.4 Test of 3D Integrator

A pair of tests were performed to ensure that the classical integrator for 3D rotations is working properly. The first test was to see if the integrator agrees with the plots of force free rotation presented in Morton's paper [32]. The initial conditions used to generate these plots were

$$(I_1, I_2, I_3) = (400, 307.808385, 200)$$
$$\bar{B}(0) = [1, 0, 0, 0]$$
$$\vec{\omega}(0) = [0.866025404, 0, -1]$$

Fig. 7.1 appears to be identical to the one presented in Morton's paper, suggesting that the integrator behaves correctly in the absense of torque.

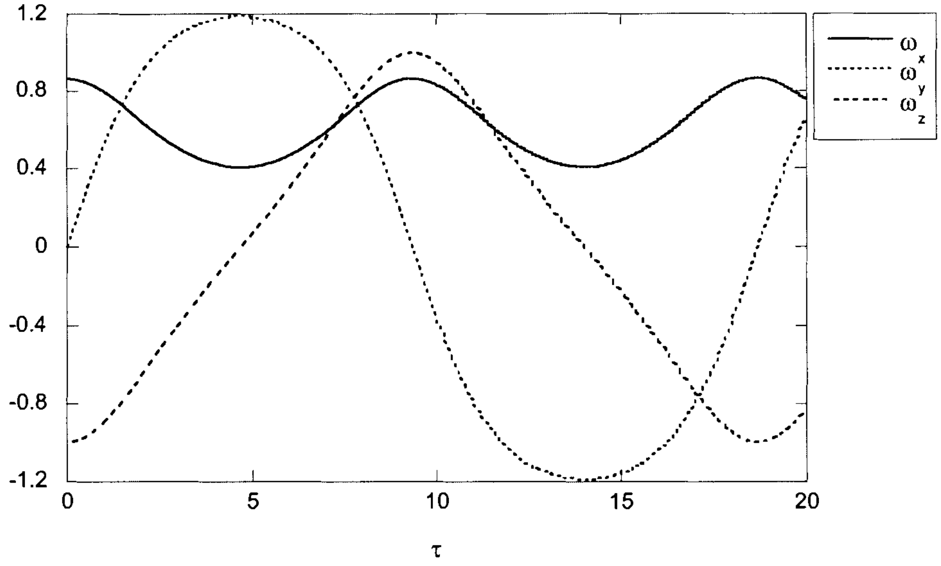

Figure 7.1: Plot of angular velocities versus time for force free rotor, performed to compare against the results in [32]

We will now show the program gives the 1D result in the correct limit when torque is included. It was verified to produce them by choosing the initial orientation to be $\bar{B}^T = [B_0, 0, 0, B_3]$, which forces the rotation to be 1D. An ensemble of trajectories were chosen from the chaotic initial state used in chapter 4, and the Euler angles generated from this state were converted to Euler parameters using Eq. (7.20) (The branch $\psi = 0$ was arbitrarily chosen for the 1D rotation). The ensemble averages are compared in Fig. 7.2 where it is found that the differences are smaller than statistical errors in $\langle J_z \rangle$, which using $\Delta\langle J_z \rangle = \sigma/\sqrt{N}$ are at most 0.05.

These tests show that our 3D integrator code correctly replicates the results found earlier for 1D rotation, as well as Morton's published results. This suggests that

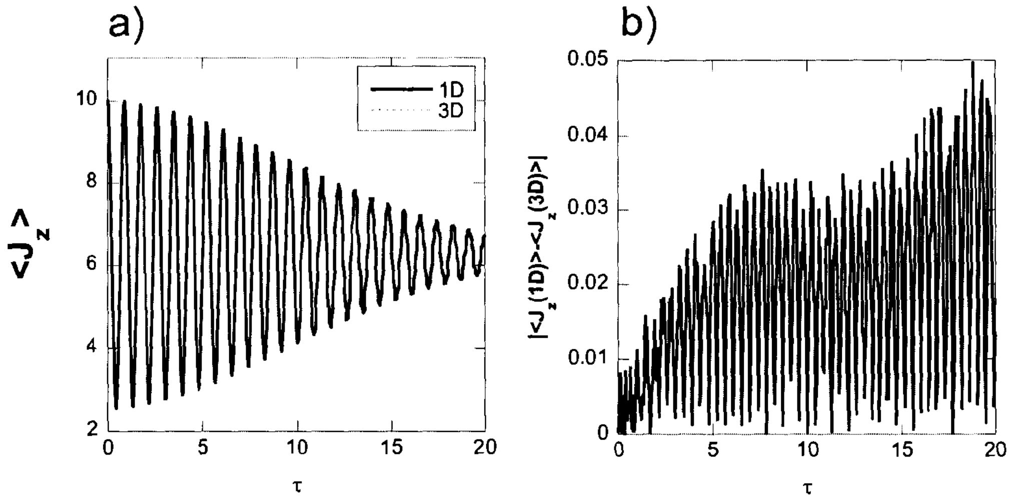

Figure 7.2: a)Plot of angular velocities versus time for Hyperion ($\alpha = 0.5$, $e = 0$, $J_0 = 10$, $\sigma = 0.5$) for both 1D and 3D cases. b) Plot of differences between 3D and 1D calculations 40,000 trajectories in ensemble.

the code is working properly, and so we can proceed with some confidence that the numerical results presented later are correct.

7.2 Stability of 1D rotation

In Wisdom's paper, it was stated without proof [45] that a small perturbation away from 1D rotation will result in Hyperion tipping into 3D rotation for any chaotic trajectory. This section will verify this claim by showing that the chaotic sea contains regions of azimuthal instability, causing the entire chaotic sea to be unstable.

An orientation is azimuthally stable if a small rotation of I_3 away from the z-axis, will result in the satellite precessing slowly about that axis (see Fig. 7.3), and unstable if these small perturbations cause I_3 to tip into the plane of the orbit.

The form of this perturbation will vary depending on the choice of coordinates. Although this perturbation is described conveniently in Euler angles as $\theta \to \theta + \delta\theta$, this perturbation is about a singular point in Euler angles, so stability analysis cannot be performed. We can remove this singularity by performing the analysis using the Euler parameters, $\bar{B}$, presented in the previous section. So these parameters are the natural way to see if 3D rotations are azimuthally stable.

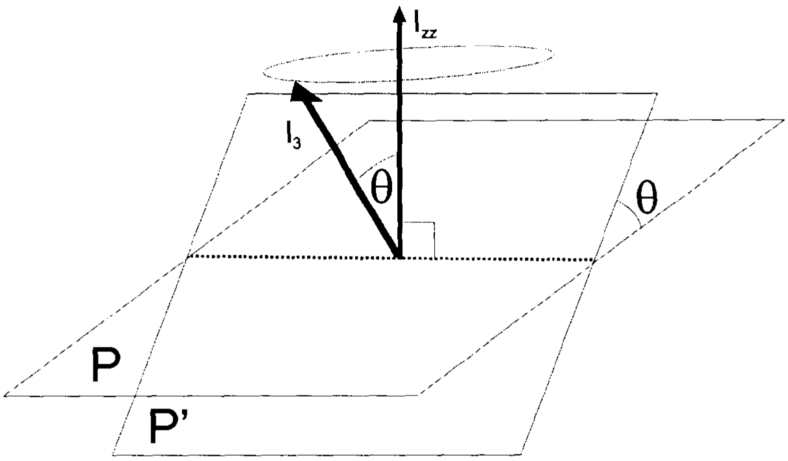

Figure 7.3: Diagram of the type of perturbation considered for azimuthal stability. I_3 is rotated down towards the orbital plane **P**, and it is called azimuthally stable if it precesses about I_{zz} as a function of time.

1D rotation can be parameterized in Euler parameters as,

$$\begin{aligned} B_0 &= \cos(\phi/2) \\ B_3 &= \sin(\phi/2) \\ \dot{B}_0 &= -J_z \sin(\phi/2) \\ \dot{B}_3 &= J_z \cos(\phi/2) \\ B_1 = B_2 = \dot{B}_1 &= \dot{B}_2 = 0 \end{aligned} \tag{7.24}$$

J_z is the dimensionless angular velocity, or equivalently the angular momentum used, in the previous chapters. In order to get 3D rotations we will have to perturb B_1 or B_2, so we will consider small perturbations in B_1 and B_2 of the form $\{B_1, B_2\} \to \{B_1 + \epsilon, B_2 + \epsilon\}$. For a sufficiently small value of ϵ these perturbations will not substantially affect the constraint $\bar{B}^T\bar{B} = 1$, and so we can hold B_0, B_3 constant as we perturb B_1, B_2.

The rotation will be stable under small perturbations in B_1, B_2 if the following criteria holds [13]:

$$K = \left| \begin{array}{cc} \frac{\partial^2 H}{\partial B_1^2} & \frac{\partial^2 H}{\partial B_1 B_2} \\ \frac{\partial^2 H}{\partial B_2 B_1} & \frac{\partial^2 H}{\partial B_2^2} \end{array} \right|_{\bar{B}} > 0 \tag{7.25}$$

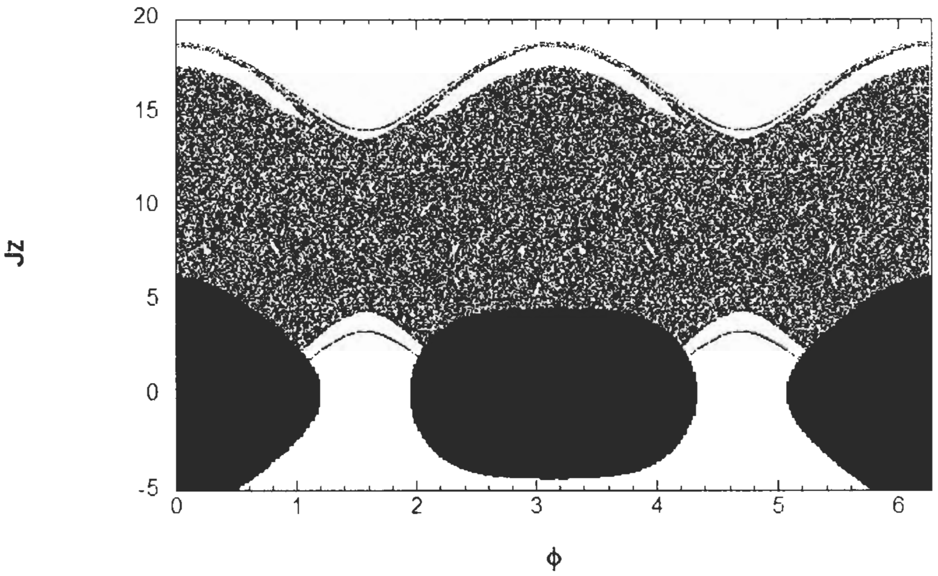

Figure 7.4: Regions of stability for 1D rotation at $\tau = 0$ for hyperion's approximate moments of inertia: $I_1 = 0.49, I_2 = 0.92, I_3 = 1$ superimposed on the 1D poincare section. The solid black regions represent areas where the rotation is azimuthally unstable.

Substituting the Hamiltonian for 3D rotation into this formula yields

$$\begin{aligned} K &= -48\,\frac{\pi^2 a^3 \left(Jz^2 T^2 \left(r\left(\tau\right)\right)^3 + 6\,\pi^2 a^3\right) AB\cos\left(2\,\Phi\left(\tau\right)\right)}{T^4 \left(r\left(\tau\right)\right)^6} \\ &+ \left(16\,AIyy + 16\,Iyy^2\right) Jz^4 + \left(-64\,\frac{\pi^2 a^3 Iyy\,B}{T^2} - 48\,\frac{\pi^2 a^3 A^2}{T^2} - 32\,\frac{\pi^2 a^3 AB}{T^2}\right) \\ &\quad Jz^2 \left(r\left(\tau\right)\right)^{-3} + \left(-144\,\frac{\pi^4 a^6 A^2}{T^4} - 80\,\frac{\pi^4 a^6 B^2}{T^4}\right) \left(r\left(\tau\right)\right)^{-6} \end{aligned} \tag{7.26}$$

$\Phi = \phi - \gamma(t)$ is the orientation of the satellite in the co-rotating frame, $A = I_2 - I_1$, $C = I_1 + I_2 - 2I_3$. $r(t)$ is the distance between the satellite and the planet, and a is the semi-major axis of the orbit. The regions of stability were found by plotting this function at $\tau = 0$ when $r = a$. The strategy behind this is simple. Since a chaotic trajectory will eventually pass through any open disk in the chaotic sea, it will be azimuthally unstable if there is any overlap between the chaotic sea and an unstable region.

Figure 7.4 shows the regions of instability for the satellite superimposed on Hyperion's Poincare section, the black regions are regions of instability and the non-black regions are stable. These two regions overlap and hence Hyperion's 1D rotation is unstable.

This analysis shows Hyperion cannot be expected to exhibit 1D rotation, since even the most subtle interactions would cause it to tip from a 1D orbit after billions of years of chaotic evolution. This is in agreement with the claims made by Wisdom [45]. However this orientation, is classically possible, and if care is taken to prepare it in an upright orientation and if we neglect quantum mechanics and environmental interactions, it would remain in that configuration indefinitely. An estimate of the maximum time that Hyperion can exhibit 1D rotation due to quantum effects will be presented in section 7.5.1.

7.3 3D Quantum Mechanics

In this section I will discuss the quantum mechanics of Hyperion's rotation in 3D. The quantum mechanics of angular momentum is a complicated topic, and aspects of it are beyond the scope of most standard text books. A more advanced treatment is given in books by Biedenharn and Louck [10], and Khersonskii et al. [15]. This section is devoted to discussing the issues that arise in finding the matrix elements of the Hamiltonian.

7.3.1 Kinetic Energy in Angular Momentum Basis

In this section we will find the matrix elements of the kinetic part of the Hamiltonian in angular momentum representation. These eigenstates are denoted by $|J, m, m'\rangle$, and are defined by the following relations:

$$\begin{aligned} \hat{J}^2|J,m,m'\rangle &= J(J+1)\hbar^2|J,m,m'\rangle & (7.27)\\ \hat{J}_z|J,m,m'\rangle &= m\hbar|J,m,m'\rangle & (7.28)\\ \hat{\mathcal{J}}_z|J,m,m'\rangle &= m'\hbar|J,m,m'\rangle & (7.29) \end{aligned}$$

Here $\hat{J}_z$ is the space fixed angular momentum about the z-axis, $\hat{J}^2 = \hat{J}_x^2 + \hat{J}_y^2 + \hat{J}_z^2$ is the total angular momentum squared, and $\mathcal{J}_z$ is the angular momentum about the body fixed 3-axis. This can be written more conveniently as

$$\mathcal{J}_j = \sum_i \mathbf{R}_{ij}(\phi, \theta, \psi) \hat{J}_i \tag{7.30}$$

These eigenstates form a convenient basis for the kinetic part of the Hamiltonian, which can be written as

$$\hat{H} = \frac{\hat{\mathcal{J}_z}^2}{2I_3} + \frac{\hat{\mathcal{J}_y}^2}{2I_2} + \frac{\hat{\mathcal{J}_x}^2}{2I_1} + \hat{V}(\phi, \theta, \psi) \tag{7.31}$$

The commutation properties of body fixed angular momentum operators is different than for space fixed operators [4, 10]. The body fixed operators satisfy

$$[\mathcal{J}_i, \mathcal{J}_j] = -i\hbar\epsilon_{ijk}\mathcal{J}_k \tag{7.32}$$

This result has the opposite sign to the space fixed result. The reversal of sign leads to a different form for the raising and lowering operators for body fixed angular momentum [10]

$$(\mathcal{J}_1 - i\mathcal{J}_2)|J, m, m'\rangle = \hbar\sqrt{(J - m')(J + m' + 1)}|J, m, m' + 1\rangle \tag{7.33}$$

$$(\mathcal{J}_1 + i\mathcal{J}_2)|J, m, m'\rangle = \hbar\sqrt{(J + m')(J - m' + 1)}|J, m, m' - 1\rangle \tag{7.34}$$

Using these ladder opperators, the matrix elements of the kinetic part of the Hamiltonian are

$$
\begin{aligned}
&\langle J,m,m'|H|J',m'',m'''\rangle = \frac{\hbar^2 m'^2}{2I_3}\delta_{m''',m'} + \frac{\hbar^2}{8}(1/I_1 - 1/I_3)\\
&\Big(\sqrt{(J-m''')(J+m'''+1)(J-m'''-1)(J+m'''+2)}\delta_{m',m'''+2}+\\
&\sqrt{(J+m''')(J-m'''+1)(J-m'''-1)(J-m'''+2)}\delta_{m',m'''-2}\Big)\\
&\frac{\hbar^2}{2}(1/I_1 + 1/I_2)(j+m''')(j+m'''+1)\delta_{m',m'''} + \langle J,m,m'|\hat{V}|J,m'',m'''\rangle
\end{aligned}
\tag{7.35}
$$

7.3.2 Matrix Elements of 3D Potential

Our derivation of the matrix elements of the potential is similar in spirit to the derivation in chapter 2. We will use the position (angle) representation of the angular momentum states, and use orthogonality relations to find the matrix elements. To do this we must find these angular momentum states in position representation.

Since the potential is diagonal in position representation, it is easiest to find these matrix elements by converting the angular momentum states to position representation and then invert the process. This conversion can be performed using

$$
\begin{aligned}
|J,m,n\rangle &= \int_0^{2\pi}\int_0^{2\pi}\int_0^{\pi} |\phi,\theta\psi\rangle\langle\phi,\theta,\psi|J,m,m'\rangle \; d\theta \; d\phi \; d\psi\\
&= \int_0^{2\pi}\int_0^{2\pi}\int_0^{\pi} D^{J*}_{m,m'}(\phi,\theta,\psi)|\phi,\theta,\psi\rangle \; d\theta \; d\phi \; d\psi
\end{aligned}
\tag{7.36}
$$

Here $D^{J}_{m,m'}(\phi,\theta,\psi) = \langle J,m,m''|\mathbf{R}(\phi,\theta,\psi)|J,m',m''\rangle$. The body fixed quantum number m'' is irrelevant here because the body fixed angular momentum is invariant under rotations, and therefore the matrix elements of R do not depend on it.

These matrix elements can be simplified using

$$
D^{J*}_{m,m'}(\phi,\theta,\psi) = e^{i(m\phi+m'\psi)} d^{j}_{m,m'}(\theta) \tag{7.37}
$$

The function $d^{j}_{m,m'}(\theta)$ has many useful algebraic properties, but most importantly $\frac{1}{2}\int_0^{\pi} d^{j}_{m,m'}(\theta) d^{k}_{n,n'}(\theta)\sin(\theta)d\theta = \delta_{j,k}\delta_{m,n}\delta_{m',n'}$. This orthoganality relation will prove invaluable in deriving the Schrodinger equation in angular momentum representation.

From Eq. (7.36) the matrix elements of the potential are

$$\begin{aligned}&\langle J, m, m'|\hat{V}|J, m'', m'''\rangle = \\ &\qquad \int_0^{2\pi}\int_0^{2\pi}\int_0^{\pi} e^{i(m''-m)\phi}e^{i(m'''-m')\psi}d^J_{m,m'}(\theta)d^{J'}_{m'',m'''}(\theta)V(\phi,\theta,\psi)\end{aligned} \tag{7.38}$$

The potential energy V can be written in terms of Euler angles as

$$\begin{aligned} V &= 3\frac{Gm}{r^3}([2\cos(2\theta - 2\psi) - 4\cos(2\psi) + \cos(-2\phi + 2\gamma + 2\theta + 2\psi) \\ &+ \cos(2\phi - 2\gamma + 2\theta + 2\psi) + \cos(2\phi - 2\gamma + 2\theta - 2\psi) \\ &- 4\cos(2\gamma - 2\phi + 2\psi + \theta) - 4\cos(-2\gamma + 2\phi - 2\psi + \theta) \\ &+ 4\cos(-2\gamma + 2\phi + 2\psi + \theta) + 6\cos(-2\gamma + 2\phi - 2\psi) \\ &+ 4\cos(2\gamma - 2\phi - 2\psi + \theta) + 6\cos(-2\gamma + 2\phi + 2\psi) \\ &+ 2\cos(2\theta + 2\psi) + \cos(-2\phi + 2\gamma + 2\theta - 2\psi)]A \\ &+ [8\cos(2\theta) + 4\cos(2\theta - 2\phi + 2\gamma) - 8\cos(2\phi - 2\gamma) \\ &+ 8/3 + 4\cos(2\theta + 2\phi - 2\gamma)]B) \end{aligned} \tag{7.39}$$

Here $A = I_2 - I_1$ and $B = I_3 - (I_1 + I_2)/2$, and γ is the position of the satellite in its orbit (previously labeled θ).

The trigonometric functions in Eq. (7.39) are proportional to $\cos(2\phi)$ and $\cos(2\psi)$. So the ϕ, ψ integrals in Eq. (7.38) are trivial, and are 0 unless $m'' = m, m'' = m \pm 2$ and $m''' = m', m''' = m' \pm 2$.

The exact form of these matrix elements is defered to appendix F, since they are cumbersome and do not provide deep insight into the classical limit. Instead we will examine the selection rules to see whether the quantum calculation is feasible using the computers we have available. From the selection rules that arise from the ϕ, ψ dependence, all but 9 possible couplings are elliminated. Now we will examine the θ dependance to find the remaining selection rules.

Once ϕ,ψ have been integrated out, the matrix elements depend on $\cos(\theta)$ and $\cos(2\theta)$, which can be converted to $\cos(\theta)^2$, requiring the following integrals to be performed:

$$\int_0^{\pi} d^J_{m,m'}(\theta)d^{J'}_{m'',m'''}(\theta)\cos\theta\sin\theta d\theta \tag{7.40}$$

$$\int_0^{\pi} d^J_{m,m'}(\theta)d^{J'}_{m'',m'''}(\theta)\cos^2\theta\sin\theta d\theta \tag{7.41}$$

These can be done using the recursion relation [15]

$$\begin{aligned}\cos(\theta)D^{J}_{m,m'}(\phi,\theta,\psi) &= \frac{\sqrt{(J^2-m^2)(J^2-m'^2)}}{J(2J+1)}D^{J-1}_{m,m'} + \frac{mm'}{J(J+1)}D^{J}_{m,m'} + \\ &\quad \frac{\sqrt{[(J+1)^2-m^2][(J+1)^2-m'^2]}}{(J+1)(2J+1)}D^{J+1}_{m,m'} \qquad (7.42)\end{aligned}$$

To deal with $\cos^2\theta$, the above recursion relation will be applied twice. This implies that each quantum state $|J,m,m'\rangle$, couples to the corresponding states with total angular momentum $J\pm 2, J\pm 1, J$. As a result the θ dependence of the potential alone causes $|J,m,m'\rangle$ to couple to 5 other states. The ϕ and ψ dependence causes it to couple to 9 other angular momentum states. An additional 5 possible couplings to states with other total angular momentum occur due to the θ dependence of the potential. Hence the total number of states that a basis vector is coupled to is: $5\times 9 = 45$. These matrix elements can be generated using the Maple code in Appendix F.

7.4 SU(2) Coherent States

7.4.1 Initial Quantum State

To compare the classical and quantum mechanics for our model of Hyperion, we must have equivalent initial states. Here I will introduce the **SU**(2) coherent states as an initial state, and an analogous classical state, so that the classical and quantum mechanics of Hyperion can be compared.

The **SU**(2) coherent states are minimum uncertainty states in which the angular momentum is as focused in one direction as quantum mechanics will permit. The simplest of these states is $|J,J,J\rangle$. This state maximizes the angular momentum in the z-direction, and because $\hat{\mathcal{J}}_z|J,J,J\rangle = \hat{J}_z|J,J,J\rangle$ the orientation is as close to $\theta=0$ as is possible.

There is nothing special about the z-axis, and analogous coherent states can be created that have their angular momentum pointing in any direction. These coherent states will be denoted $|J,\phi,\theta\rangle$, defined as

$$|J,\phi,\theta\rangle = \mathbf{R}(\phi,\theta,0)|J,J,J\rangle \qquad (7.43)$$

Any $\mathbf{SU}(2)$ coherent state can be found by rotating $|J, J, J\rangle$. This state in angular momentum representation is,

$$\langle J', m', m''|\mathbf{R}(\phi, \theta, 0)|J, J, J\rangle = \delta_{J',J} D_{m',J}(\phi, \theta, 0) \tag{7.44}$$

The initial quantum state can then be efficiently found using recursion relations [10].

7.4.2 Classical Initial State

There is a problem in comparing quantum to classical mechanics for 3D rotations, because it is impossible to construct a classical state that replicates all the moments of a quantum state (except as the size of the Hilbert space, $K \to \infty$) [17]. Therefore I will choose the classical distributions to match the low order moments of the quantum distribution.

As we saw previously, any $\mathbf{SU}(2)$ coherent can be constructed by rotating the state $|J, J, J\rangle$. Hence if we can find a classical distribution that is analogous to $|J, J, J\rangle$, the analogue of the other coherent states can be found by rotating this distribution.

As the classical analogue of the state $|J, J, J\rangle$, we choose the distribution

$$P(J_z, J_x, J_y) = \frac{\delta(J_z - J\beta)}{\pi} \exp\left(\frac{-L_x^2 - L_y^2}{\beta^2}\right) \tag{7.45}$$

This satisfies the quantum relations $\langle J_z\rangle = \beta J$, $\langle J^2\rangle = \beta^2 J(J+1)$, and $\langle J_x\rangle = \langle J_y\rangle = 0$.

The angular distribution will be chosen to match the quantum angular probability distribution. The form of the wave function for $|J, J, J\rangle$ [10], is

$$|\langle \phi, \theta, \psi|J, J, J\rangle|^2 = [d^J_{J,J}(\theta)]^2 = \cos(\theta/2)^{2J} \tag{7.46}$$

Hence the distribution of ψ, ϕ is uniform on the interval $[0, 2\pi)$, and the distribution in θ is given by 7.46. The classical trajectories are randomly generated from these probability distributions.

Random trajectories for the analogue of the coherent state $|J, \phi, \theta\rangle$ can be generated by rotating the angular momentum vectors generated from the analogue of the state $|J, J, J\rangle$ and the orientations can similarly be found by solving $\mathbf{R}(\phi', \theta', \psi') = \mathbf{R}(\phi, \theta, 0)\mathbf{R}(\phi_0, \theta_0, \psi_0)$. The angles $\{\phi', \theta', \psi'\}$ parameterize the trajectory taken from the classical analogue of $|J, \phi, \theta\rangle$, and $\{\phi_0, \theta_0, \psi_0\}$ are the angles describing the trajectory randomly chosen from the analogue of $|J, J, J\rangle$.

The classical integrator is written in terms of Euler parameters, so the Euler angles must be converted into Euler angles. This conversion from angular momentum to $\dot{\bar{B}}$ can be performed easily using Eq. (7.6), and the orientation can also be found in terms of $\bar{B}$ using Eq. (7.4).

7.5 Lyapunov Exponents and Breaktime for 3D Rotation

3D motions of bodies are difficult to visualize, because the phase space is 6 dimensional. We cannot use a poincare section to see the chaotic and the non-chaotic regions of phase space, so a different approach must be used.

To characterize the phase space, the classical ensembles corresponding to 100 coherent states on the sphere $|J| = 10$ (here J is in units of I_3/T) were sampled, and the average Lyapunov exponent was found for each of these states. These Lyapunov exponents determine whether a state is chaotic or regular. This provides us some intuition about the structure of phase space for this system, even though we cannot readily visualize it.

It was found that for $\alpha = 0.43$ (where $\alpha = (I_2 - I_1)/I_3$), that all of the states in question had an average Lyapunov exponent of $\lambda = 2.0$ in units of the orbital period. This also shows that the sphere $|J| = 10$ lies within a chaotic sea, but it tells little else about the structure of phase space.

This calculation took 3 weeks to complete, using 10 nodes on the Bugaboo cluster, and so it was deemed to be impractical to continue the search to characterize more of the phase space. However this does give an estimate for the Lyapunov exponent for Hyperion's 3D rotation, which can be used to estimate how long Hyperion can rotate perpendicular to the orbital plane before the uncertainty principle predicts it should tip.

7.5.1 Breaktime for 1D Rotation

As mentioned in section 7.2, the 1D rotation for Hyperion is azimuthally unstable at places in the chaotic sea. Thus if the width of the state becomes too large in θ the rotation will no longer obey the 1D approximation. This tipping is inevitable since chaos causes the width in θ to increase exponentially with time, and an estimate similar to the Ehrenfest breaktime can be made to find the typical length of time this 1D assumption is valid for. To do this the initial width of the coherent state $|J, J, J\rangle$ is estimated, using the following asymptotic relation [38].

$$d^j_{J,J}(\theta) = [\cos(\theta/2)]^{2J} \rightarrow \exp(-J\theta^2/4) \tag{7.47}$$

The quantum number J is approximately $L_z/\hbar$ where L_z is a typical value of the angular momentum in the z-direction. This equation is valid for all values of θ (IE $\theta \in [0, \pi)$) in the limit of large J. From Eq. (7.47) the width of the distribution in angle is approximately $\Delta\theta = \sqrt{2\hbar/L_z}$. This width should increase exponentially at a rate given by the Lyapunov exponent, and if we assume that the rotation will no longer be one dimensional when $\Delta\theta = 0.01$, then

$$t_{1D} = \frac{1}{2\lambda} \log\left(\frac{0.05 L_z}{\hbar}\right) \tag{7.48}$$

Using a characteristic action $L_z = 10I_3/T$ in Eq. (7.48), $\hbar = \beta I_3/T = 9 \times 10^{-58} I_3/T$, and $\lambda = 2$ yields a breaktime of $t_{1D} \approx 32 = 2.1$ years, which is well after saturation occurs. Since the 1D approximation to Hyperion's motion is valid over the timescales in question where dynamically interesting behavior occurs, then the previous results are meaningful since they are used primarily to estimate how Hyperion would behave for short times if its rotation were perpendicular to the orbital plane.

7.6 Feasibility Of the Quantum Calculation

Hyperion's classical probability distributions can be found using the computers currently available. However the quantum analogs cannot be found because of the number of operations grows too rapidly with the size of the Hilbert space for existing computers to approximate the classical limit.

The majority of the operations in a numerical integral occur in function evaluations, so by counting the number of number of operations that must be made per call for 3D rotation and dividing this by the number of operations needed for the 1D program we will be able to estimate the ratio between the computing times for the two algorithms.

From the selection rules found in section 7.3.2, the number of operations required for the 3D algorithm is proportional to $45(2K+1)^3$, whereas the complexity of the

1D case is approximately $3(2K+1)$. The maximum value of K used in the 1D case was $K = 25000$. In the 3D case, the quantum number which produces this degree of complexity is $K = 12$. This would allow a purely quantum mechanical calculation, but not one that would likely reveal any classical behavior. To obtain the classical limit we would need $J > 100$ which would require approximately 1000 times the computing power we currently have available, which is a Pentium 4, 2.7 GHz computer. Hence the quantum calculation was not done, and at present it is not possible to meaningfully compare quantum and classical mechanics for Hyperion's rotation in 3D.

7.7 Summary

In this section we have examined the motion of Hyperion using Euler parameters. The equations of motion were found to reduce to the 1D case in the limit $B_1 = B_2 = 0$. By analyzing the stability of Hyperion's rotation using Euler parameters, we have shown (in agreement with Wisdom [45]), that the 1D rotation will be unstable in the chaotic sea. The chaotic tumbling of Hyperion was found to have a Lyapunov exponent of 2.0 inverse orbital periods, which is approximately Hyperion's observed value [45].

The instability of Hyperion's orbit suggests that, from quantum uncertainty, it can only exhibit a 1D rotation for approximately 4.2 years, but since the dynamics we are interested in occurs over a shorter period in time than this, the 1D rotation of Hyperion is reasonable to consider.

The quantum mechanics proved to be too computationally demanding to carry sufficiently far towards the classical limit to meaningfully compare to classical mechanics. Because the number of operations in the numerical integration of the Schrödinger equation scales as K^3, it is not feasible to carry out the calculation to $K > 12$ since a 1000 fold increase in power would be required to calculate $K = 100$.

Chapter 8

Summary

In this thesis I examined the quantum mechanics of the rotation of an asymmetric satellite in a gravitational field. Particular emphasis was placed on the one-dimensional rotation of the satellite, which occurs when its rotational axis is perpendicular to the orbital plane. The quantum mechanics of this rotation was compared to the classical mechanics, and the effects that the environment has on the quantum classical differences was also considered. Finally the structure of the Floquet states of this system was discussed, and the model was extended to include three dimensional rotation. This chapter reviews the important results covered in the previous chapters, and discuss how Hyperion reaches the classical limit.

8.1 QC differences for Regular and Chaotic Motion

For regular motion, the QC differences in $\langle J_z \rangle$ are proportional to $[\hbar T/I_3]^2$, where T is the orbital period and I_3 is the moment of inertia for rotations about the z-axis. These differences grow as t^2 before reaching a maximum value. After this maximum value these differences are quasi-periodic in time. Because the differences in $\langle J_z \rangle$ are proportional to $[\hbar T/I_3]^2$, these QC differences for Hyperion would be negligible if its rotation were not chaotic.

The probability distributions do not approach the classical limit in a pointwise sense for regular motion. However, the distributions appear to be the classical result with quantum oscillations superimposed on them. The amplitude of these oscillations does not diminish as $[\hbar T/I_3] \to 0$, but they occur over a much finer scale than the classical distribution and they will not be noticeable in the classical limit.

For chaotic motion, the QC differences in $\langle J_z \rangle$ are proportional to β^2 for early times but unlike the regular case, grow exponentially in time until the differences saturate. The level that these differences saturate at is proportional to $[\hbar T/I_3]^{2/3}$. This suggests that the classical limit of $\langle J_z \rangle$ should be reached for Hyperion even without environmental effects.

The probability distributions for a chaotic initial state do not resemble the classical probability distributions, despite the fact that the quantum expectation values will be nearly in agreement with the classical result. The differences between these distributions tend to be quasi-random, and occur on such a fine scale that they become very difficult to resolve in the classical limit.

Although there are qualitative differences between the chaotic and non-chaotic cases, their results are similar. The expectation values for both cases converge to the classical limit. In addition neither of their probability distributions converge to the classical limit without either environmental effects or imperfect detectors. So although the results for the two systems are qualitatively different, the classical limit is reached in a similar manner for both regular and chaotic states.

8.2 Effects of Coarse Graining and Decoherence

Coarse graining and environmental effects have a similar effect on the QC differences in the angular momentum probability distributions. The probability distributions were coarse-grained by convoluting them with a triangular filter function, which represents the resolution of a detector. Assuming the detector can measure features of a size Δ_s, the integrated differences in the probability distributions are proportional to $(\hbar T/[I_3\Delta_s])^{0.44}$. From this relationship I found that the detector must have a resolution of at least 10^{-60} rad/s in order to notice a substantial difference between the quantum and classical probability distributions. Hence for all practical purposes, Hyperion's probability distribution will appear classical even without the environment.

Environmental effects were modeled by random interactions between Hyperion and the space dust surrounding Saturn. The maximum values of the integrated QC differences in the probability distribution are proportional to $(\hbar^2/[DI_3])^{1/6}$, where D is the momentum diffusion parameter. The smoothing that the environment performs on the momentum probability distribution is proportional to $\sqrt{D}$, so this power law depends on a similar composite parameter to the composite parameter for coarse graining. Using this relationship, I find that even the dilute interplanetary gas around Saturn is sufficient to reduce the integrated QC differences from 0.7 to 10^{-10}.

Either decoherence or coarse graining can explain the classical appearance of Hyperion. Because either of these effects can explain the classical appearance of the Satellite, it is wrong to think of the classical limit of Hyperion as only a result of environmental interactions, as claimed by Zurek [46, 47].

Some might argue that fundamentally, the quantum differences are suppressed by the environment and so classical physics is in some sense a result of environmental influences. However because these differences are so small as to be irrelevant, we do *need* to include environmental effects to understand the classical appearance of macroscopic chaotic bodies even if they do eliminate these effects.

8.3 Floquet States and 3D Rotation

In chapter 6 I investigate the structure of the Floquet states for this system. For this model of Hyperion, the chaotic Floquet states are not localized. This means that a state in the chaotic sea will be composed of more Floquet states than a non-chaotic state, and allows us to distinguish between a regular and chaotic region of phase space by comparing the number of Floquet states in the two regions. Also the classical probability distribution in the late time limit can be found by averaging the quantum angular momentum distributions. This also explains why the classical expectation values are reached in the saturation regime even though large quantum fluctuations are present.

Finally in chapter 7, I extend the model into 3D. The classical mechanics of 3D rotations can be efficiently solved using a set of quaternionic coordinates called Euler parameters [32]. By using these coordinates I find that 1D rotation in the chaotic sea is azimuthally unstable. In addition it was found that the Lyapunov exponent for 3D rotation is approximately 2 orbital periods. Using this I find that the 1D rotation of Hyperion can only persist for 4.2 years, before quantum uncertainty will cause it to tip.

The QC differences were not compared for 3D rotation because the computing resources needed to numerically integrate the Schrödinger equation are far beyond what is currently available. Fortunately 3D rotation is not as interesting as 1D rotation, because in 3D rotation the extra degrees of freedom will create an effect similar to decoherence. Hence one dimensional rotations should be more pathological than 3D rotations for Hyperion, and since the one-dimensional rotations reach the classical limit without decoherence, the 3D rotations should do so as well.

This work does leave many questions unanswered, such as why the average of the Floquet probability distributions is the classical probability distribution and why the QC differences follow the power laws that I have found here. Perhaps a random matrix theory treatment of QC differences could help explain the origin of these differences, but at present I see no way to justify them. However this work does lay to rest any questions about the classical limit of Hyperion, and the debate about the role of decoherence in chaotic systems should be relegated to mesoscopic bodies where decoherence undoubtedly can have a profound influence [39].

There is a question of which of these effects will dominate for mesoscopic bodies. Unfortunately we have only shown that environmental effects are not needed to understand the classical limit of Hyperion, and we cannot say that in general the classical limit is reached without environmental effects. However if this system is typical, then chaotic mesoscopic systems could seem classical because of environmental interactions, difficulties in resolving interference patterns, or a combination between these two effects.

Appendix A

Integrator Test For Schrödinger Equation

In this appendix I will show that the routine that finds the numerical solution to the Schrödinger equation behaves correctly. This is done by finding an eigenfunction of the Schrödinger equation when the satellite has a circular orbit. When $e = 0$ the time dependance of the Hamiltonian can be removed by examining the system in a co-rotating frame, allowing energy eigenfunctions to be calculated. Since these eigenfunctions are stationary in the co-rotating frame, they should rotate but retain the same form in the fixed frame. By finding these eigenfunctions numerically, and by verifying that the integrated result rotates appropriately in position representation we can check to see if the integrator is working properly.

To find the Eigenvalue equation and the appropriate boundary conditions, we will transform the Schrödinger equation to remove the time dependence. The Schrödinger equation in position representation is

$$i\hbar\frac{\partial\psi(\phi,t)}{\partial t} = -\frac{\hbar^2}{2I_3}\frac{\partial^2\psi(\phi,t)}{\partial\phi^2} - \frac{3\pi}{T^2}\left(\frac{a}{r}\right)^3 (I_2 - I_1)\cos(2[\phi - \theta(t)])\psi(\phi,t) \qquad \text{(A.1)}$$

The transformation to the co-rotating frame is performed through:

$$\begin{aligned} \Phi &= \phi - 2\pi t' \\ t &= t' \end{aligned} \qquad \text{(A.2)}$$

This transformation may be applied to a wave function through [4]

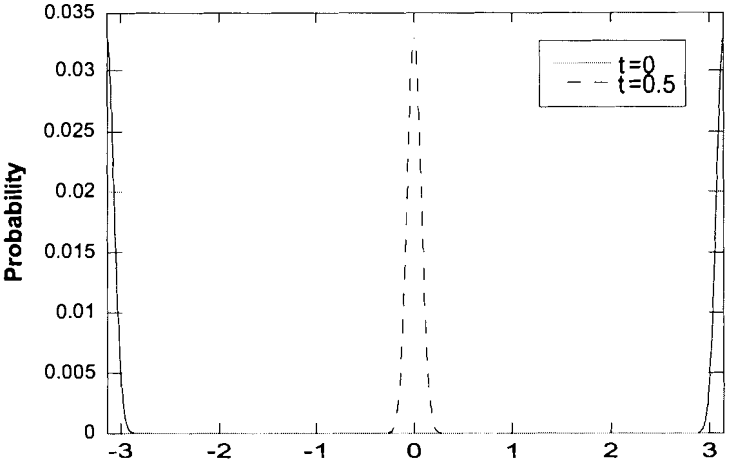

Figure A.1: Plot of Eigenfunction($E = -14.75$) for Eq. (A.4) in fixed frame

$$\begin{aligned} \psi'(\Phi) &= e^{-if(\phi,t)}\psi(\phi,t) \\ f(\phi,t) &= \frac{2\pi\phi - \frac{4\pi^2}{2}\tau}{\beta} \end{aligned} \tag{A.3}$$

Performing this transformation on the wave function yields the following eigenvalue equation

$$E\psi'(\Phi) = -\frac{\beta^2}{2I_3}\frac{\partial^2\psi'(\Phi,t)}{\partial\Phi^2} + [2\pi^2 - 3\pi^2\alpha\cos(2\Phi)]\psi'(\Phi) \tag{A.4}$$

Eq. (A.4) is the Mathieu equation, and its solutions are eigenfunctions in the co-rotating frame. Since the eigenfunctions are fixed in the rotating frame then they will rotate in the fixed frame. Mathieu functions are well known, but there is no simple closed form for these functions, so it is more convenient to numerically solve for the eigenfunction.

Although periodic boundary conditions apply in the fixed frame, they do not apply in the co-rotating frame. To transform from the boundary conditions from the fixed to the co-rotating frame, Eq. (A.3) must be applied to the boundary conditions resulting in

$$\psi'(-\pi) = \exp\left(\frac{4\pi^2 i}{\beta}\right)\psi'(\pi) \tag{A.5}$$

Using this boundary condition, and $\beta = 0.08$, the lowest eigenvalue for Eq. (A.4) was found using Matlab to be $E = -14.75$. This wavefunction was then transformed back into the fixed frame, and then converted to angular momentum representation via a fast fourier transform. The wavefunction was then integrated in angular momentum representation, and periodically transformed back into angular representation and compared to the original wave function.

In Fig. A.1 it can be seen that the Mathieu function is rotated by π at $\tau = 0.5$ as expected, confirming that the quantum integrator is working properly.

Appendix B

Scaling Parameter for QC Differences

The QC differences for an arbitrary quantum system depend on the Hamiltonian, and for chaotic systems it is difficult to predict these differences at late times. Pattanayak et al. [36] showed that when environmental interactions are included, the QC differences will eventually become a function of ξ, where $\xi = \hbar^a \lambda^b D^c$ and a, b, c are real numbers. This scaling relationship is very useful because it states that the QC differences are not a function of all of the system and environmental parameters, but rather is a function of only the composite parameter ξ.

The argument here is similar to the one presented in [46]. It is assumed that the differences between quantum and classical mechanics arise when the Moyal terms in the time evolution of the Wigner function are non-negligible. For a chaotic system the probability distribution will vary over a progressively finer scale in momentum as it fills the accessible phase space. Then after sufficient time the fine structure in the quantum distriubtion will settle to an equilibrium scale in momentum given by [35, 36]

$$\frac{\partial \rho^w}{\partial p} \approx \sqrt{\frac{\lambda}{2D}} \tag{B.1}$$

Since each of the moyal terms in Eq. (1.14) are $\propto \hbar^{2n} \partial_x^{2n+1} V(x) \partial_p^{2n+1} \rho^w$, the first term in the Moyal expansion is

$$\xi = \hbar^{2n} \lambda^{2n+1/2} D^{-(n+1/2)} \frac{\partial^{2n+1} V(x)}{\partial x^{2n+1}} \tag{B.2}$$

Here n is included because the first non-zero Moyal term may not necessarily be $\propto \hbar^2$.

If the probability distribution has reached the equilibrium scale given by Eq. (B.1), then if the state still has minimal uncertainty, the state's variation in position should be proportional to $\sqrt{D/\lambda}$. To find the dependance of the composite parameter ξ on $\hbar$ and D to lowest order on x, the characteristic variation of $\partial_x^3 V(x) \propto \sin(x)$ is needed.

Expanding the potential about any given x_0 to lowest order will not give a measure of the characteristic variation of $\sin(x)$, since in the chaotic sea since x_0 can take on any value. So expanding $\sin(x)$ about an arbitrary point x_0, and averaging over x_0 will give a better estimate of the characteristic variation of $\sin(x)$.

To second order $\sin(x)$ expanded about an arbitrary point is:

$$\begin{aligned} \frac{\partial^3 V(x)}{\partial x^3} &\propto \sin\left(x_0\right) + \cos\left(x_0\right)\left(x - x_0\right) \\ &- 1/2 \sin\left(x_0\right)\left(x - x_0\right)^2 + O\left(\left(x - x_0\right)^3\right) \end{aligned} \tag{B.3}$$

Averaging this equation over $x_0 = 0 \cdots 2\pi$ and dropping all but the lowest order term yields:

$$\frac{\partial^3 V(x)}{\partial x^3} \propto x \approx \sqrt{D/\lambda} \tag{B.4}$$

Inserting Eq. (B.4) into Eq. (B.2) yields:

$$\xi \propto \frac{\hbar^2}{D} \tag{B.5}$$

This shows that for sufficiently late times, the QC differences for our model of Hyperion should depend on a single parameter $\hbar^2/D$.

Appendix C

Calculation of Lyapunov Exponents

Attention must be given to the method used to calculate Lyapunov exponents since if the program to find them is not written carefully it will yield a poor estimate of λ. This appendix is devoted to explaining how Lyapunov exponents were calculated in this work. The maximum Lyapunov exponent is defined as [28],

$$\lambda = \lim_{t\to\infty} \lim_{d\to 0} \frac{1}{t} \ln\left(\frac{|\mathbf{d}(t)|}{|\mathbf{d}(0)|}\right) \tag{C.1}$$

Here $\mathbf{d}$ is the distance between the two nearby trajectories x_1, x_2. This formula can be rewritten in a more convenient form by considering the distance only at discrete times $t = k\tau$,

$$\begin{aligned} \lambda &= \lim_{k\to\infty} \frac{1}{k\tau} \ln\left(\frac{|\mathbf{d}(k\tau)|}{|\mathbf{d}([k-1]\tau)|}\frac{|\mathbf{d}([k-1]\tau)|}{|\mathbf{d}([k-2]\tau)|}\cdots\frac{|\mathbf{d}(\tau)|}{|\mathbf{d}(0)|}\right) && \text{(C.2)} \\ &= \lim_{k\to\infty} \frac{1}{k\tau} \sum_{i=1}^{k} \ln\left(\frac{|\mathbf{d}(i\tau)|}{|\mathbf{d}([i-1]\tau)|}\right) && \text{(C.3)} \end{aligned}$$

As mentioned in the introduction, this formula alone will not accurately produce the Lyapunov exponent because the distance between the two trajectories will increase until they no longer exponentially seperate. As a result the distance between them must be occaisonally rescaled to ensure that $\mathbf{d}$ does not become too large [33]. Rescaling will reduce the distance between the trajectories x_1 and x_2 without changing the direction of the distance vector. This was done by the following rescaling,

$$\vec{x}_2 \to \vec{x}_1 + 1 \times 10^{-2} \frac{\vec{x}_2 - \vec{x}_1}{|\vec{x}_2 - \vec{x}_1|} \tag{C.4}$$

$\mathbf{d}$ was rescaled whenever $|\vec{x}_1 - \vec{x}_2|$ is greater than 10^{-3}. The values used here were arbitrarily chosen to be values that yielded good results for the Lyapunov exponent. In Eq. (C.2) for the Lyapunov exponent it is hard to see how to incorporate this rescaling, so for our purposes Eq. (C.3) is far easier to implement.

In Eq. (C.3) there are three quantities that have to be kept in memory, $\mathbf{d}(i\tau)$, $\mathbf{d}([i-1]\tau$, and $\sum_{j=1}^{i} \ln\left(\frac{|\mathbf{d}(j\tau)|}{|\mathbf{d}([j-1]\tau)|}\right)$. After calculating the jth term in this sum if rescaling is found to be needed, then $\mathbf{d}(j\tau)$ is rescaled according to Eq. (C.4). This rescaled $\mathbf{d}$ is then used in the calculation of the next term and not in the current term, becuase doing so would artificially reduce the Lyapunov exponent.

x_1 is chosen to be somewhere in the chaotic sea. Its location is irrelevant because λ should be constant over the entire chaotic sea. x_2 was chosen to be a distance of 1×10^{-5} from x_1, and the Lyapunov exponent was found by performing the sum in Eq. (C.3) and rescaling the distance as needed. The value of τ chosen was the orbital period of Hyperion or $\tau = 1$ in the dimensionless units of chapter 2.

Lyapunov exponents for Hamiltonian systems are also notoriously difficult to calculate because the partial sums in Eq. (C.3) fluctuate and converge very slowly to the maximum Lyapunov exponent. The Lyapunov exponent may be constant for a long time before suddenly falling off to a smaller value. To reduce these problems k was chosen to be 50,000 which appeared to be more than sufficient to cause the Lyapunov exponent to converge.

The Lyapunov exponents were calculated for the 3D rotation using a slightly modified version of the code used to calculate the 1D Lyapunov exponents. It was modified to work with a set of 4 Euler parameters and their derivatives rather than ϕ and $\dot{\phi}$. Also since the Euler parameters must satisfy $|\bar{B}| = 1$. The perturbed angles must always satisfy this constraint, and the previous and the rescaling proceedure mentioned previously will not necessarily yield a set of valid Euler parameters. To correct this problem Eq. (C.3) was used and then the resulting vector was renormalized through

$$\bar{B} \rightarrow \frac{\bar{B}}{|\bar{B}|} \tag{C.5}$$

$$\dot{\bar{B}} \rightarrow \dot{\bar{B}} - \dot{\bar{B}} \cdot \bar{B} \tag{C.6}$$

For computational reasons the maximum value of k for the 3D rotation was reduced to 10,000 but the program would stop at 5000 if the sum appeared to have converged. Increasing k to 50,000 did not substantially change the results for a test run considered.

Appendix D

Generation of Correlated Random Numbers

To describe the effect of environmental perturbations, we require a sequence of correlated random numbers. Random number generators for uncorrelated random variates are commonly available, but algorithms for generating a correlated sequence are not common. We show here how to generate a random sequence having a controled amount of correlation from a standard sequence of independently distributed random numbers. Let $\{r_i\}$ be such a sequence, with zero mean and unit variance.

$$\langle r_i \rangle = 0 \tag{D.1}$$

$$\langle r_i r_j \rangle = \delta_{ij} \tag{D.2}$$

To generate a correlated sequence $\{R_i\}$ from the uncorrelated sequence, we simply form linear combination as follows:

$$R_{i+1} = cR_i + (1-c)r_{i+1} \tag{D.3}$$

where c is a chosen constant and $R_1 \equiv r_1$. It follows from Eq. (D.3) that

$$R_{i+1} = c^{i-1}r_1 + \sum_{m=0}^{i-1} c^m (1-c) r_{i+1-m} \tag{D.4}$$

From this result, we can calculate the degree of correlation in our new sequence. Taking $i > j$, and using Eq. (D.4) and Eq. (D.2), we obtain

$$\langle R_i R_j \rangle = \sum_{m=0}^{i-2} \sum_{m'=0}^{j-2} c^{m+m'} (1-c)^2 \langle r_{i+1-m} r_{j+1-m'} \rangle +$$

$$\sum_{m=0}^{i-2} c^m(1-c)c^{j-1}\langle r_1 r_{i+1-m}\rangle +$$
$$\sum_{m'=0}^{j-2} c^{m'}(1-c)c^{i-1}\langle r_{j+1-m'} r_1\rangle + c^{i-j-2}\langle r_1^2\rangle \tag{D.5}$$

Eq. (D.5) can be simplified using Eq. (D.2). Performing the resulting geometric sums then yields

$$\langle R_i R_j\rangle = \left(\frac{1-c}{1+c}\right) c^{i-1}(c^{1-j} - c^{j-1}) \tag{D.6}$$

For $j \gg 1$ Eq. (D.6) becomes:

$$\langle R_i R_j\rangle \approx \left(\frac{1-c}{1+c}\right) c^{i-j} \tag{D.7}$$

This discrete sequence must now be converted into a function of time. Each R_i refers to the correlated random function at time t_i. Taking the time interval between the random numbers to be Δt, then it is appropriate to define a correlation time $\tau_c = -\Delta t/\ln(c)$ for the correlated random function, for which we have

$$\langle R(0)R(\tau)\rangle \approx \left(\frac{1-c}{1+c}\right) e^{-\tau/\tau_c} \tag{D.8}$$

Appendix E

Momentum Diffusion Parameter

The momentum diffusion parameter (D) is needed the calculate the effect of the environment on the system [43, 2, 40]. In particular, the form of D is needed to show that the scaling result in [36] applies also to our model.

Consider the random potential of the form $V = V_0 \cos(\phi)$. The random torque is then $F = V_0 R(t) \sin(\phi)$. Here $R(t)$ is a correlated random function, as defined in Appendix A. From this, we can find the momentum diffusion parameter through the relation

$$\tilde{D} = \lim_{t \to 0} \frac{\langle s(t)^2 \rangle}{t} \tag{E.1}$$

The integral of the torque over time yield the angular momentum, hence the variance of the angular momentum under this random torque is given by

$$\begin{aligned} \langle s^2(t) \rangle &= \frac{V_0^2}{2} \int_0^t \int_0^t \mathrm{dt'dt''} \langle R(t') R(t'') \rangle \\ &= \frac{V_0^2}{2} \int_0^t \int_0^t \mathrm{dt'dt''} \left(\frac{1-c}{1+c} \right) c^{|t'-t''|/t_c} \\ &= V_0^2 \left(\frac{1-c}{1+c} \right) (t_c^2 + t_c t + t_c^2 \exp(-t/t_c)) \end{aligned} \tag{E.2}$$

The quantity $s(t)$ is the standard deviation of the angular momentum for a random walk under the influence of Eq. (5.1), and σ is the standard deviation of the random potential. For $t \gg t_c$ we have

$$\langle s^2(t) \rangle \approx t t_c V_0^2 \left(\frac{1-c}{1+c} \right) \tag{E.3}$$

Using E.1 and choosing the value $c = 1/2$, we obtain momentum diffusion constant $\tilde{D}$ to be

$$\tilde{D} = \frac{V_0^2 t_c}{3} \tag{E.4}$$

In the body of this paper, we use a dimensionless momentum diffusion parameter D. The relation between these two quantities is

$$D = \tilde{D}\frac{T^3}{2I_3^2} = \frac{\sigma^2 \tau_c}{6} \tag{E.5}$$

where τ_c is defined to be $\tau_c = t_c/T$, and $\sigma = V_0 T^2/I_3$.

Appendix F

Maple Code for Matrix Elements of the Potential

This maple code generates the matrix elements for the potential energy of Hyperion for 3D rotation in angular momentum representation. The output is the non-zero elements of $< J, m, m'|V|J', m'', m''' >$.

```
> restart:
> with(linalg):
```

Here we define the rotation matrix in terms of Euler angles. The terms ct, st refer to $cos(\theta), \sin(\theta)$. They are left in this form in order to prevent them from being included in trig functions during simplification.

```
> mom:=matrix([[I_1,0,0],[0,I_2,0],[0,0,I_3]]):
> Rz1:=matrix([[cos(phi),sin(phi),0],[-sin(phi),cos(phi),0],[0,0,1]]):
> Ry:=matrix([[ct,0,-st],[0,1,0],[st,0,ct]]):
> Rz2:=matrix([[cos(psi),sin(psi),0],[-sin(psi),cos(psi),0],[0,0,1]]):
> rot:=multiply(Rz1,Ry,Rz2):
```

The above defines the rotation matrix in terms of the 3 Euler angles (phi,theta,psi) and gamma which is the orientation of the center of mass, the subsequent code finds the moments of inertia in terms of these angles. To do this we must define the orientation of the center of mass. This orientation is denoted γ and to prevent them from being included in trig functions we will use the variables, $sg = \sin(\gamma), cg = \cos(\gamma)$.

```
> rm:=matrix([[cg,sg,0],[-sg,cg,0],[0,0,1]]):
> ans:=multiply(transpose(rm),(rot),mom,transpose(rot),(rm)):
```

Now we will find the potential in terms of cos(2 phi) etc, in order to easily find the non-zero matrix elements of the potential given in [7.21]

```
> V:=simplify(Gm/r^3/2*(-2*ans[1,1]+ans[2,2]+ans[3,3])):
> s1:=cos(phi)^2=combine(cos(phi)^2,trig):
> s2:=cos(psi)^2=combine(cos(psi)^2,trig):
> s3:=sin(psi)^2=combine(sin(psi)^2,trig):
> s4:=sin(phi)^2=combine(sin(phi)^2,trig):
> V2:=subs(s1,s2,s3,s4,V):
> s1:=sin(phi)=sin(2*phi)/cos(phi)/2:
> s2:=sin(psi)=sin(2*psi)/cos(psi)/2:
> V3:=subs(s1,s2,V2):
```

V3 now contains the potential in terms of $\sin(2\phi), \cos(2\phi), \sin(2\psi), \cos(2\psi)$. These define a new set of substitutions using the orthoganality properties of the trig functions,

```
> s1:=cos(2*phi)=(d[2,0]+d[-2,0])/2:
> s2:=sin(2*phi)=(d[2,0]-d[-2,0])/2/I:
> s3:=cos(2*psi)=(d[0,2]+d[0,-2])/2:
> s4:=sin(2*psi)=(d[0,2]-d[0,-2])/2/I:
```

Here d[2,0] denotes $\delta_{m,m'+2}$ and d[0,2] denotes $\delta_{m',m'''+2}$. We will now apply these orthoganality relations to find the matrix C[n,m] which contains the coefficients of the terms d[n,0]*d[0,m].

```
> a1:=simplify(subs(s1,s2,s3,s4,V3)):
> C[2,2]:=coeff(coeff(a1,d[2,0]),d[0,2]):
> C[2,-2]:=coeff(coeff(a1,d[2,0]),d[0,-2]):
> C[-2,2]:=coeff(coeff(a1,d[-2,0]),d[0,2]):
C[-2,-2]:=coeff(coeff(a1,d[-2,0]),d[0,-2]):
```

The above terms are the terms do not give C[0,n],c[m,0], to get these we will eliminate the double coupling terms from our expression allowing us to find the single coupling terms.

```
> ared:=simplify(a1-C[2,2]*d[2,0]*d[0,2]-C[2,-2]*d[2,0]*d[0,-2]-C[-2,-2]
> *d[-2,0]*d[0,-2]-C[-2,2]*d[-2,0]*d[0,2]):
> C[2,0]:=coeff(ared,d[2,0]):
> C[-2,0]:=coeff(ared,d[-2,0]):
> C[0,-2]:=coeff(ared,d[0,-2]):
> C[0,2]:=coeff(ared,d[0,2]):
```

Finally we will eliminate these single coupling terms from our expression, and the remaining term will be C[0,0] or the coefficient that measures the self coupling of a state vector.

```
> C[0,0]:=simplify(ared-C[2,0]*d[2,0]-C[-2,0]*d[-2,0]-C[0,2]*d[0,2]-C[0
,-2]*d[0,-2]):
```

The orthoganality properties of the trig functions in phi, psi have been used. Now we will use recursion relationships in Eq. (7.42) to find the matrix elements of the Hamiltonian.

Here we will convert sin into cosine, because it is easier to use recursion relationships for cosine than for sin.

```
> C2[0,0]:=simplify(subs(st^2=1-ct^2,sg^2=1-cg^2,C[0,0])):
> C2[0,2]:=simplify(subs(st^2=1-ct^2,sg^2=1-cg^2,C[0,2])):
> C2[0,-2]:=simplify(subs(st^2=1-ct^2,sg^2=1-cg^2,C[0,-2])):
> C2[2,0]:=simplify(subs(st^2=1-ct^2,sg^2=1-cg^2,C[2,0])):
> C2[-2,0]:=simplify(subs(st^2=1-ct^2,sg^2=1-cg^2,C[2,0])):
> C2[2,2]:=simplify(subs(st^2=1-ct^2,sg^2=1-cg^2,C[2,2])):
> C2[2,-2]:=simplify(subs(st^2=1-ct^2,sg^2=1-cg^2,C[2,-2])):
> C2[-2,2]:=simplify(subs(st^2=1-ct^2,sg^2=1-cg^2,C[-2,2])):
> C2[-2,-2]:=simplify(subs(st^2=1-ct^2,sg^2=1-cg^2,C[-2,-2])):
```

Now we will use the rotation matrix elements recursion relations to find the matrix elements of cos(2θ) and $cos(2\theta)^2$. We will denote the krocecker delta functions $\delta J, J' + 1$ as dj[1] in the subsequent work.

```
> cttemp:=sqrt((J^2-m^2)*(J^2-m1^2))/J/(2*J+1)*dj[-1]+m*m1/J/(J+1)*dj[0
> ]+sqrt(((J+1)^2-m^2)*((J+1)^2-m1^2))/(J+1)/(2*J+1)*dj[1]:
> cttemp2:=subs(J=J-1,dj[-1]=dj[-2],dj[0]=dj[-1],dj[1]=dj[0],cttemp):
> cttemp3:=subs(J=J+1,dj[-1]=dj[0],dj[0]=dj[1],dj[1]=dj[2],cttemp):
> cos2:=subs(dj[-1]=cttemp2,dj[1]=cttemp3,dj[0]=cttemp,cttemp):
```

cos2 contains the matrix elements of $cos(2\theta)$. Now we will make these orthoganality substitutions to effectively integrate out the remaining theta dependence of the components $C[n, m]$.

```
> C4[0,0]:=simplify(C2[0,0]-coeff(C2[0,0],ct)*ct-coeff(C2[0,0],ct^2)*ct
> ^2)*dj[0]+coeff(C2[0,0],ct)*ct+coeff(C2[0,0],ct^2)*ct^2:
> C4[0,2]:=simplify(C2[0,2]-coeff(C2[0,2],ct)*ct-coeff(C2[0,2],ct^2)*ct^
> 2)*dj[0]+coeff(C2[0,2],ct)*ct+coeff(C2[0,2],ct^2)*ct^2:
> C4[0,-2]:=simplify(C2[0,-2]-coeff(C2[0,-2],ct)*ct-coeff(C2[0,-2],ct^2)
> *ct^2)*dj[0]+coeff(C2[0,-2],ct)*ct+coeff(C2[0,-2],ct^2)*ct^2:
> C4[2,0]:=simplify(C2[2,0]-coeff(C2[2,0],ct)*ct-coeff(C2[2,0],ct^2)*ct^
> 2)*dj[0]+coeff(C2[2,0],ct)*ct+coeff(C2[2,0],ct^2)*ct^2:
> C4[2,-2]:=simplify(C2[2,-2]-coeff(C2[2,-2],ct)*ct-coeff(C2[2,-2],ct^2)
> *ct^2)*dj[0]+coeff(C2[2,-2],ct)*ct+coeff(C2[2,-2],ct^2)*ct^2:
> C4[2,2]:=simplify(C2[2,2]-coeff(C2[2,2],ct)*ct-coeff(C2[2,2],ct^2)*ct^
> 2)*dj[0]+coeff(C2[2,2],ct)*ct+coeff(C2[2,2],ct^2)*ct^2:
> C4[-2,0]:=simplify(C2[-2,0]-coeff(C2[-2,0],ct)*ct-coeff(C2[-2,0],ct^2)
> *ct^2)*dj[0]+coeff(C2[-2,0],ct)*ct+coeff(C2[-2,0],ct^2)*ct^2:
> C4[-2,-2]:=simplify(C2[-2,-2]-coeff(C2[-2,-2],ct)*ct-coeff(C2[-2,-2],c
> t^2)*ct^2)*dj[0]+coeff(C2[-2,-2],ct)*ct+coeff(C2[-2,-2],ct^2)*ct^2:
> C4[-2,2]:=simplify(C2[-2,2]-coeff(C2[-2,2],ct)*ct-coeff(C2[-2,2],ct^2)
> *ct^2)*dj[0]+coeff(C2[-2,2],ct)*ct+coeff(C2[-2,2],ct^2)*ct^2:
```

```
> C3[0,0]:=subs(ct^2=cos2,ct=cttemp,cg^2=(1-c2g)/2,cg=c2g/2/sg,C4[0,0])
> :
> C3[0,2]:=subs(ct^2=cos2,ct=cttemp,cg^2=(1-c2g)/2,cg=c2g/2/sg,C4[0,2]):
> C3[0,-2]:=subs(ct^2=cos2,ct=cttemp,cg^2=(1-c2g)/2,cg=c2g/2/sg,C4[0,-2]
> ):
> C3[2,0]:=subs(ct^2=cos2,ct=cttemp,cg^2=(1-c2g)/2,cg=c2g/2/sg,C4[2,0]):
> C3[-2,0]:=subs(ct^2=cos2,ct=cttemp,cg^2=(1-c2g)/2,cg=c2g/2/sg,C4[-2,0]
> ):
> C3[2,-2]:=subs(ct^2=cos2,ct=cttemp,cg^2=(1-c2g)/2,cg=c2g/2/sg,C4[2,-2]
> ):
> C3[2,2]:=subs(ct^2=cos2,ct=cttemp,cg^2=(1-c2g)/2,cg=c2g/2/sg,C4[2,2]):
> C3[-2,2]:=subs(ct^2=cos2,ct=cttemp,cg^2=(1-c2g)/2,cg=c2g/2/sg,C4[-2,2]
> ):
> C3[-2,-2]:=subs(ct^2=cos2,ct=cttemp,cg^2=(1-c2g)/2,cg=c2g/2/sg,C4[-2,-
> 2]):
```

Now that all the integrals are performed, I will re-arrange the components in a more transparent form. The matrix C[i,j,k] will contain the coefficients of C[i,j]*dj[k].

```
> C[0,0,0]:=coeff(C3[0,0],dj[0]):
> C[0,0,1]:=coeff(C3[0,0],dj[1]):
> C[0,0,2]:=coeff(C3[0,0],dj[2]):
> C[0,0,-1]:=coeff(C3[0,0],dj[-1]):
> C[0,0,-2]:=coeff(C3[0,0],dj[-2]):
> C[0,-2,0]:=coeff(C3[0,-2],dj[0]):
> C[0,-2,1]:=coeff(C3[0,-2],dj[1]):
> C[0,-2,2]:=coeff(C3[0,-2],dj[2]):
> C[0,-2,-1]:=coeff(C3[0,-2],dj[-1]):
> C[0,-2,-2]:=coeff(C3[0,-2],dj[-2]):
> C[0,2,0]:=coeff(C3[0,2],dj[0]):
> C[0,2,1]:=coeff(C3[0,2],dj[1]):
> C[0,2,2]:=coeff(C3[0,2],dj[2]):
> C[0,2,-1]:=coeff(C3[0,2],dj[-1]):
> C[0,2,-2]:=coeff(C3[0,2],dj[-2]):
> C[2,0,0]:=coeff(C3[2,0],dj[0]):
> C[2,0,1]:=coeff(C3[2,0],dj[1]):
> C[2,0,2]:=coeff(C3[2,0],dj[2]):
> C[2,0,-1]:=coeff(C3[2,0],dj[-1]):
> C[2,0,-2]:=coeff(C3[2,0],dj[-2]):
> C[2,-2,0]:=coeff(C3[2,-2],dj[0]):
> C[2,-2,1]:=coeff(C3[2,-2],dj[1]):
> C[2,-2,2]:=coeff(C3[2,-2],dj[2]):
> C[2,-2,-1]:=coeff(C3[2,-2],dj[-1]):
> C[2,-2,-2]:=coeff(C3[2,-2],dj[-2]):
> C[2,2,0]:=coeff(C3[2,2],dj[0]):
> C[2,2,1]:=coeff(C3[2,2],dj[1]):
> C[2,2,2]:=coeff(C3[2,2],dj[2]):
> C[2,2,-1]:=coeff(C3[2,2],dj[-1]):
> C[2,2,-2]:=coeff(C3[2,2],dj[-2]):
```

```
> C[-2,0,0]:=coeff(C3[-2,0],dj[0]):
> C[-2,0,1]:=coeff(C3[-2,0],dj[1]):
> C[-2,0,2]:=coeff(C3[-2,0],dj[2]):
> C[-2,0,-1]:=coeff(C3[-2,0],dj[-1]):
> C[-2,0,-2]:=coeff(C3[-2,0],dj[-2]):
> C[-2,-2,0]:=coeff(C3[-2,-2],dj[0]):
> C[-2,-2,1]:=coeff(C3[-2,-2],dj[1]):
> C[-2,-2,2]:=coeff(C3[-2,-2],dj[2]):
> C[-2,-2,-1]:=coeff(C3[-2,-2],dj[-1]):
> C[-2,-2,-2]:=coeff(C3[-2,-2],dj[-2]):
> C[-2,2,0]:=coeff(C3[-2,2],dj[0]):
> C[-2,2,1]:=coeff(C3[-2,2],dj[1]):
> C[-2,2,2]:=coeff(C3[-2,2],dj[2]):
> C[-2,2,-1]:=coeff(C3[-2,2],dj[-1]):
> C[-2,2,-2]:=coeff(C3[-2,2],dj[-2]):
```

Here C[k1,k2,k3]=<J+k3,m+k1,m'+k2|V|J,m,m'>, and c2g in these represents cos(2gamma(t)) which is the orientation of Hyperion's center of mass from the space fixed x-axis.

Bibliography

[1] P.W. Anderson. *Phys. Rev.*, **109**:1492, 1958.

[2] J. R. Anglin, J. P. Paz, and W. H. Zurek. *Phys. Rev. A*, **55**:4041, 1997.

[3] L. E. Ballentine. Fundamental problems in quantum mechanics. Kluwer Academic Publishers, 1995.

[4] L. E. Ballentine. *Quantum Mechanics, A Modern Development.* World Scientific, Singapore, 1998.

[5] L. E. Ballentine. Fractal probability distributions and the classical limit. *Physics Letters A*, **261**:145, 1999.

[6] L. E. Ballentine. Dynamics of quantum-classical differences for chaotic systems. *Phys. Rev. A*, **65**:062110, 2002.

[7] L. E. Ballentine. Quantum-to-classical limit in a hamiltonian system. *Phys. Rev. A*, **70**:032111, 2004.

[8] L. E. Ballentine and S. M. McRae. Moment equations for probability distributions in classical and quantum mechanics. *Phys. Rev. A*, 58:1799–1809, 1998.

[9] L. E. Ballentine, Y. Yang, and J. P. Zibin. *Phys. Rev. A*, **50**:2854, 1994.

[10] L. C. Biedenharn and J. D. Louck. *Angular Momentum in Quantum Physics Theory and Application.* Addison-Wesley, Reading, Mass., 1981.

[11] Bradley W. Caroll and Dale A. Ostlie. *An Introduction to Modern Astrophysics.* Addison Wesley, New York, 1996.

[12] G. Casati and B.V. Cherikov. *Phys. Rev. Letters*, **75**:350, 1995.

[13] G. L. Cassidy and G. R. Fowles. *Analytical Mechanics, 5th ed.* Saunders College Publishing, New York, 1993.

[14] W. T. Coffey, Yuri P. Kalmykov, and John T. Waldron. *The Langevin Equation: with Applications to Stochastic Problems in Physics, Chemistry and Electrical Engineering.* World Scientific Publishing Co Inc, New Jersey, 2004.

[15] V. K. Khersonskii D. A. Varshalovich, A. N. Moskalev. *Quantum Theory of Angular Momentum.* World Scientific, Teaneck, New Jersey, 1988.

[16] P. Ehrenfest. *Z. Phys.*, **45**:455, 1927.

[17] J. Emerson. *Chaos and Quantum-Classical Correspondence For Two Coupled Spins.* PhD thesis, 2001.

[18] J. Emerson and L. E. Ballentine. Characteristics of quantum-classical correspondence for two interacting spins. *Phys. Rev. A*, **63**:052103, 2000.

[19] J. Emerson and L. E. Ballentine. *Phys. Rev. E*, **64**:026217, 2001.

[20] Mario Feingold. Distribution of matrix elements in chaotic systems. *Phys Rev. A.*, **34**(1), 1986.

[21] S. Fishman, D. R. Grempel, and R. E. Prange. *Phys. Rev. Letters*, **49**(8), 1982.

[22] Herbert Goldstein. *Classical Mechanics.* Addison-Wesley, Reading, Mass, 1980.

[23] D. A. Gurnett, A. M. Persoon, W. S. Kurth, and L. J. Granroth. Direct detection of dust particles in the outer solar system by voyagers 1 and 2. presented at Cospar 2002, D1.2, Oct. 2002.

[24] Fritz Haake. *The Quantum Signitures of Chaos.* Springer, New York, 2001.

[25] S. Habib, K. Jacobs, H. Mabuchi, R. Ryne, K. Shizume, and B. Sundaram. *Phys. Rev. Let.*, **88**:040402, 2002.

[26] Salman Habib, Kosuke Shizume, and Wojciech Hubert Zurek. Decoherence, chaos, and the correspondence principle. *Phys. Rev. Letters*, (**80**):4361, 1998.

[27] R. L. Hudson. When is the wigner quasi-probability density non-negative? *Rep. Math. Phys*, (**6**):249–252, 1974.

[28] Jorge V. Jose and Eugene J. Saletan. *Classical Dynamics: A Contemporary Approach.* Cambridge University Press, Cambridge, 1998.

[29] A. R. Kolovsky. *Phys. Rev. Letters*, (**76**):340, 1996.

[30] Karol Zyczkowski Marcin Pozniak and Marek Kus. Composed ensembles of random unitary matrices. *J. Phys*, (**A31**):1059–1071, 1998.

[31] M. L. Mehta. *Random Matrices.* Academic, New York, 1991.

[32] Harold S. Morton. Hamiltonian and lagrangian formulation of rigid-body rotational dynamics based on the euler parameters. *The Journal of the Astronautical Sciences*, 41(4):569–591, 1993.

[33] Edward Ott. *Chaos in Dynamical Systems.* Cambridge University Press, New York, 2002.

[34] Arjendu K. Pattanayak. Lyapunov exponents, entropy production, and decoherence. *Phys. Rev. Letters*, **83**(22):4526–4529, 1999.

[35] Arjendu K. Pattanayak. Characterizing the metastable balance between chaos and diffusion. *Physica D.*, **148**(1), 2001.

[36] Arjendu K. Pattanayak, Bala Sundaram, and Benjamin D. Greenbaum. Parameter scaling in the decoherent quantum-classical transition for chaotic systems. *Phys. Rev. Letters*, **90**:014103, 2003.

[37] R. D. Present. *The Kinetic Theory of Gas.* McGraw Hill, New York, 1958.

[38] D. J. Rowe, H. de Guise, and B. C. Sanders. Asymptotic limits of su(2) and su(3) wigner functions. *J. Math. Phys.*, **42**(5), May 2001.

[39] R. Sankaranarayanan, A. Lakshminaryan, and V.B. Sheorey. Quantum chaos of a particle in a square well: Competing length scales and dynamical localization. *Phys. Rev. E.*, **64**:046210, 2001.

[40] W. T. Strunz, F. Haake, and D. Braun. Universality of decoherence for macroscopic quantum superpositions. *Phys. Rev. A*, **67**, 2003.

[41] K. Takahashi. *Prog. Theor. Phys. Supp.*, (**98**), 1989.

[42] P. Thomas, J. Veverka, D. Morrison, M. Davies, and T. V. Johnson. Saturn's small satellites: Voyager imaging results. *Journal of Geographical Research*, 88:8743, 1983.

[43] W. G. Unruh and W. H. Zurek. Quantum decoherence and brownian motion of a harmonic oscillator. *Phys. Rev. D*, **40**:1071, 1989.

[44] F. Haake W. T. Strunz. Universality of decoherence for macroscopic quantum superpositions. *Phys. Rev. A*, **67**:022102, 2003.

[45] J. Wisdom. Chaotic behavior in the solar system. *Astron J.*, **94**:1350, 1987.

[46] W. H. Zurek. *Physica Scripta*, **T76**:186, 1998.

[47] W. H. Zurek and J. P. Paz. Why we don't need quantum planetary dynamics: decoherence and the correspondence principle for chaotic systems., 1996. arXiv:quant-ph/9612037.